

UNIVERSITY OF TOULOUSE

---

# Un joli titre

---

Flaurent HEULLY-ALAR

October 10, 2025



# Contents

<b>1</b>	<b>Introduction</b>	<b>8</b>
<b>2</b>	<b>Theory and Methodology</b>	<b>9</b>
2.1	Model Hamiltonian . . . . .	9
2.1.1	Isotropic Hamiltonian . . . . .	9
2.1.2	Magnetic anisotropy in mononuclear complexes . . . . .	11
2.1.3	Magnetic anisotropy in polynuclear complexes . . . . .	14
2.2	Methodology . . . . .	16
2.2.1	Hartree-Fock Method . . . . .	17
2.2.2	Configuration Interaction . . . . .	18
2.2.3	Complete Active Space Self Consistent Field . . . . .	20
2.2.4	Perturbation Theory . . . . .	21
2.2.5	Difference dedicated configurational interaction . . . . .	22
2.2.6	Density functional theory . . . . .	23
2.2.7	Inclusion of Spin-Orbit effects . . . . .	25
2.2.8	Embedded Cluster Method . . . . .	26
2.2.9	Effective Hamiltonian Theory . . . . .	27
<b>3</b>	<b>Study of the magnetic anisotropy in mononuclear complexes</b>	<b>30</b>
3.1	First-Order Spin-Orbit Coupling . . . . .	31
3.2	Impact of the Electric field on the ZFS parameters . . . . .	47
3.2.1	Computational Informations . . . . .	50
3.2.2	Application of the electric field along the Z axis . . . . .	51
3.2.3	Application of the electric field along the Y axis . . . . .	57
3.2.4	Conclusion . . . . .	61
<b>4</b>	<b>Electric field on Exchange anisotropy</b>	<b>64</b>
4.1	Computational Informations . . . . .	66

4.2	Theoretical model . . . . .	67
4.3	Impact of First-Order Spin-Orbit Coupling in the absence of electric field . . . . .	72
4.4	Impact of the electric field on the symmetric anisotropic exchange parameter . . . . .	74
4.5	Conclusion . . . . .	78
<b>5</b>	<b>Herbertsmithite</b>	<b>80</b>
5.1	Density-Functional Theory study . . . . .	80
5.1.1	In-plane couplings . . . . .	81
5.1.2	Out-of-plane coupling . . . . .	84
5.2	Wave-Function Theory study . . . . .	88
5.2.1	Isotropic Coupling . . . . .	88
5.2.2	Anisotropic interactions . . . . .	92
5.3	Conclusion . . . . .	97

# List of Figures

2.1	Schematic representation of the three lowest SO-state undergoing ZFS in the case of triplet ground state. . . . .	13
2.2	Difference between the orbitals space in Hartree-Fock and CASSCF Theory . . . . .	20
2.3	Classes of excitations and associated DDCI method . . . . .	23
2.4	Schematic representation of the three region composing the embedding. red: cluster, orange: TIPS, blue: point charges . . . . .	26
2.5	Schematic representation of the three spaces involved in effective Hamiltonian theory . . . . .	28
3.1	Schematic representation of the Fe(II) complex . . . . .	32
3.2	Representation of the complex Ni(Me <sub>6</sub> trenCl)(ClO <sub>4</sub> ) . . . . .	47
3.3	Energy diagrams of the d-orbitals in $C_3$ symmetre and affected by Jahn-Teller distortion . . . . .	48
3.4	Energies of the ground state in the three cases (a),(b) and (c) for $\vec{F} \parallel Z$ . . . . .	52
3.5	Evolution of the axial D parameter as a function of the field applied in cases (a), (b) and (c) for $\vec{F} \parallel Z$ . . . . .	53
3.6	Evolution of the rhombic E parameter as a function of the field applied in cases (a), (b) and (c) for $\vec{F} \parallel Z$ . . . . .	54
3.7	Energies of the ground state in the three cases (a),(b) and (c) for $\vec{F} \parallel Y$ . . . . .	58
3.8	Evolution of the axial D parameter as a function of the field applied in cases (a), (b) and (c) for $\vec{F} \parallel Y$ . . . . .	59
3.9	Evolution of the rhombic E parameter as a function of the field applied in cases (a), (b) and (c) for $\vec{F} \parallel Y$ . . . . .	60

4.1	(a) $Cu_2Cl_5$ model molecule of $D_{2h}$ symmetry, (b) displacement $\delta$ of the atoms generated by the application of an electric field along the $y$ direction. . . . .	65
4.2	$D_{AB}$ as a function of the outside angle $\phi$ for different levels of calculations . . . . .	73
4.3	$D_{AB}$ (in $cm^{-1}$ ) as a function of the electric field applied in the X, Y and Z directions for CAS(6,4)SCF/SCF-SO calculations .	75
4.4	$D_{AB}$ (in $cm^{-1}$ ) as a function of the electric field applied in the Y direction, obtained at three levels of calculation. . . . .	76
5.1	The three computed fragments using DFT calculations for in-plane couplings. . . . .	82
5.2	Schematic representation of the fragments and the couplings introduced	83
5.3	Embedded cluster used to compute the out of plane coupling before geometry optimisation . . . . .	84
5.4	Close environment of intersite $Cu^{2+}$ in both structure obtained via DFT with the B3LYP functional . . . . .	86
5.6	Trinuclear and dinuclear embedded clusters used for Wave-funciton computation . . . . .	88
5.7	CAS(4,3)SCF, bridging orbital and magnetic orbitals calculated on the dinuclear fragment . . . . .	90
5.8	Active space orbitals from CAS(9,6) calculation. . . . .	91
5.9	Representation matrix of the Multi-Spin Hamiltonian in the basis of the four components of the quartet and the doubly-degenerate doublet states . . . . .	96
5.10	Schematic representation of the DMI vector components in two adjacent $Cu^{2+}$ triangles of the lattice. . . . .	98

# List of Tables

3.1	Dipole moment components in Debye at $F=0$ V.m $^{-1}$ . . . . .	51
3.2	Slopes of the straight lines in cases (a), (b) and (c) for the D and E parameter for $\vec{F} \parallel Z$ , Fig. 3.5 and 3.6 . . . . .	53
3.3	Contributions to the axial parameter D of the most contributing excited states, variations of SOC and energy difference $\Delta E$ for $\vec{F} \parallel Z$ . . . . .	55
3.4	Variation of the distances in Angstrom between the Ni(II) ion and the closest atoms of the ligand between $-F$ and $+F$ with $\vec{F} \parallel Z$ . . . . .	55
3.5	Variation between $-F$ and $+F$ applied in the Z direction of the orbital energy difference $\Delta(\Delta\epsilon(d_{x^2-y^2} - d_{xy}))$ in cm $^{-1}$ . . . . .	56
3.6	Weight $w(d_{xz})$ and $w(d_{yz})$ of the determinants with single occupation in the respective orbitals, their difference $\Delta w(X - Y)$ and their overall variation $\Delta(\Delta w(X - Y))$ in all three case of calculation for $\vec{F} \parallel Z$ . . . . .	56
3.7	Slopes of the straight lines in cases (a), (b) and (c) for the D and E parameter for $\vec{F} \parallel Y$ . . . . .	57
3.8	Contributions to the axial parameter D of the most contributing excited states, variations of SOC and energy difference $\Delta E$ for $\vec{F} \parallel Y$ . . . . .	61
3.9	Variation of the distances in Angstrom between the Ni(II) ion and the closest atoms of the ligand between $-F$ and $+F$ with $\vec{F} \parallel Y$ . . . . .	61
3.10	Weight $w(d_{xz})$ and $w(d_{yz})$ of the determinants with single occupation in the respective orbitals, their difference $\Delta w(X - Y)$ and their overall variation $\Delta(\Delta w(X - Y))$ in all three case of calculation for $\vec{F} \parallel Y$ . . . . .	62

4.1	Representation matrix of $\hat{H}^{SO}$ and electronic couplings in the uncoupled basis. . . . .	70
4.2	Numerical matrix of $\hat{H}^{SO}$ and electronic couplings in the uncoupled basis from a CAS(6,4)DDCI/DDCI-SO calculation with no electric field and $\phi = 130^\circ$ . . . . .	74
4.3	Variational contribution in $\text{cm}^{-1}$ of the excited states to $D_{AB}$ and its value in $\text{cm}^{-1}$ extracted from effective Hamiltonian at CAS(6,4)DDCI/DDCI-SO level . . . . .	74
4.4	Numerical matrix of $\hat{H}^{SO}$ and electronic couplings in the uncoupled basis from a CAS(6,4)DDCI/DDCI-SO calculation in the presence of an electric field of 0.01 a.u ( $5.1724 \times 10^4 \text{ kV.cm}^{-1}$ ) and $\phi = 130^\circ$ . . . . .	76
4.5	Variational contribution in $\text{cm}^{-1}$ of the excited states to $D_{AB}$ and $ d_{ab} $ given in value in $\text{cm}^{-1}$ extracted from effective Hamiltonian at CAS(6,4)DDCI/DDCI-SO level . . . . .	77
5.1	Matrix representation of the Ising Hamiltonian in the basis of determinants $M_S=1/2$ and $M_S=3/2$ . . . . .	82
5.2	Values of the $J_i$ couplings in Kelvin in the three fragments and the distance associated to each couplings. . . . .	83
5.3	Distance between the oxygens and the copper ions, defect or in plane, in the $C_3$ structure and the relative displacement in both optimisation scheme given in Å. . . . .	85
5.4	Values of the $J_i$ interactions given in Kelvin in presence of a $Cu^{2+}$ defect in the intersite for the $C_3$ and both optimised structure. .	87
5.5	Values of $J_1$ in $\text{cm}^{-1}$ extracted on both fragment. Dynamical correlation calculation are performed on the miniaml active space.	90
5.6	Values in Kelvin of the $ d $ DM magnitude and its components, axial (D) and rhomic (E) anisotropic exchange parameters, obtained for both fragments. . . . .	97

# Chapter 1

## Introduction

The present work aims to determine the mechanisms at play to obtain large values of molecular magnetic anisotropy and in one case extend the established procedure to real crystalline system. This thesis is organised around four chapters. The first is dedicated to the review of the theoretical models applied to molecular magnetic anisotropy by both experimentalist and theoricians. The model Hamiltonians and interactions will be presented and some insight on their origins will be given. The second part of this chapter is dedicated to the computational methodology that will be applied throughout this work. It introduces some informations on ways to obtain the wave-functions and energies that are crucial to make the connection to model Hamiltonians. Chapter 2 concerns the study of first-order spin-orbit coupling and its implication on the models. Two types of mononuclear complexes were examined (Chapter 3), the first originates from a collaboration with experimentalists whose objective is the synthesis of complexes with large anisotropy induced by first-order SOC. Our work was complementary to the experimental characterisation of the complexes and to the evaluation of the validity of the usual models. Following a previous study, the second complex has already been identified to exhibit large anisotropy values. Our interest lies in the evolution of its properties under the effect of an external electric field. The chapter 3 is the continuation of a study which had for purpose to determine the source of the parameters of anisotropic exchange in a binuclear toy model. One way to induce anisotropy in this system is to apply an electric field, Finally, a real system application

# Chapter 2

## Theory and Methodology

### 2.1 Model Hamiltonian

#### 2.1.1 Isotropic Hamiltonian

##### Heisenberg Hamiltonian

The Heisenberg-Dirac-van Vleck (HDvV) Hamiltonian is the most well-known and the most widely used Hamiltonian to model the behavior of system of interacting localized magnetic centers. It writes:

$$\hat{H}_{HDVV} = - \sum_{i,j} J_{ij} \hat{\mathbf{S}}_i \cdot \hat{\mathbf{S}}_j \quad (2.1.1)$$

where  $J_{i,j}$  is the coupling constant,  $\hat{\mathbf{S}}_i$  and  $\hat{\mathbf{S}}_j$  are the spin operators working on site  $i$  and  $j$ . Other conventions exist with a positive sign and/or a factor of 2 in front). With the convention of eq. 2.1.1, a positive  $J_{i,j}$  value indicates a ferromagnetic coupling between sites  $i$  and  $j$  (the coupling between these sites stabilizes the state with the largest total  $\hat{\mathbf{S}}_{tot} = \hat{\mathbf{S}}_i + \hat{\mathbf{S}}_j$ ) while a negative value indicates an antiferromagnetic coupling (the state with the lowest  $S_{tot}$  value is stabilized). This Hamiltonian is regarded as a spin Hamiltonian since it acts only on the spin degree of freedom of the system (*i.e.* the spatial part of all determinants is supposed to be the same).

$J$  is an effective parameter, that means that it considers, in the ideal case, all the mechanisms that couple  $\hat{\mathbf{S}}_i$  and  $\hat{\mathbf{S}}_j$ . The most important ones are:

- 1- The direct exchange originating from the exchange integral  $K$  that has a ferromagnetic contribution.

- 2- The Anderson mechanism going through ionic determinants that has an antiferromagnetic contribution.
- 3- Super-exchange and spin polarization involving excitations of a diamagnetic bridging ligand.

In the case of two electrons in two orbitals  $a$  and  $b$ , the Anderson mechanism and its contribution to the effective integral value can be understood from the Hubbard Hamiltonian that considers both the neutral forms  $|ab|$ ,  $|\bar{a}b|$ ,  $|\bar{a}\bar{b}|$ ,  $|a\bar{b}|$  (*i.e.* those considered in the HDvV Hamiltonian) and the ionic forms  $|\bar{a}\bar{a}|$  and  $|\bar{b}\bar{b}|$ . In the basis of  $M_S=0$  determinants, the Hamiltonian is written:

$$\hat{H} = \begin{pmatrix} |a\bar{b}| & |\bar{a}b| & |a\bar{a}| & |b\bar{b}| \\ \hline 0 & K & t & t \\ K & 0 & t & t \\ \hline t & t & U & K \\ t & t & K & U \end{pmatrix}$$

$t = t_{ab}$  is the hopping integral between sites  $a$  and  $b$  and  $U$  is the energy of the ionic forms compared to the energy of the neutral ones. As long as  $U = U_{aa} = U_{bb}$  is large compared to  $t$ , neutral forms dominate the wave function of the low energy singlet state (the triplet state is fully neutral in the Hubbard space) and it is possible to derive  $J = J_{ab}$  from  $K$ ,  $t$  and  $U$ . At the second-order perturbation theory, one obtains the following expression for the effective integral  $J$ :

$$J = 2K - \frac{4t^2}{U} \quad (2.1.2)$$

This expression shows the competition between a ferromagnetic component (direct exchange  $K>0$ ) and an antiferromagnetic one (Anderson mechanism).

Super-exchange contributions (excitations on diamagnetic ligands) appear at higher order of perturbation and can be seen as correction to the value of the above parameters and can be expressed as:

$$J = 2K_{eff} - \frac{4t_{eff}^2}{U_{eff}} \quad (2.1.3)$$

where the parameters are now effective parameters taking into account the effect of mechanisms involving the bridging ligand electrons and orbitals. For  $t_{eff}$  some mechanisms are illustrated in Figure XXX une belle figure montrant un

mécanisme passant par le pont. The hopping integral between a metal and the ligands of its coordination sphere being much larger than the metal to metal one, the  $t_{eff}$  may be much larger than the  $t_{ab}$  previously defined.

## Ising Hamiltonian

The eigenfunctions of the Heisenberg Hamiltonian are eigenfunctions of the  $\hat{\mathbf{S}}^2$  and  $\hat{S}^z$  operators, making them intrinsically multi-determinantal functions (except for the maximum  $|M_S|$  components), that requires Wave Function Theory (WFT) based calculation methods to be evaluated. Ising is a simpler model restricted to the components of  $\vec{S}$  along the  $z$  axis (reducing it to a classical-like spin problem) whose states are eigenfunctions of  $S^z$  only:

$$H_{Ising} = - \sum_{i,j} J_{ij} \hat{\mathbf{S}}_{z,i} \hat{\mathbf{S}}_{z,j} \quad (2.1.4)$$

The magnetic moment of each magnetic site are now considered to align with the  $z$  axis at all time, taking a  $\pm S$  value. The main advantage of this approximation is that the eigenfunctions of this Hamiltonian are those of broken-symmetry DFT methods. It is then possible to fit  $J_{ij}$  values to DFT results. DFT avoiding the diagonalization of large matrices, it is much faster and applicable on larger systems than WFT methods.

### 2.1.2 Magnetic anisotropy in mononuclear complexes

Effects such as Spin-Orbit-Coupling (SOC) tend to create magnetic anisotropy that cannot be described by eq (2.1.1). More specifically on mononuclear systems (only one magnetic centre) with a ground state of spin larger or equal to one and correct symmetry conditions, a lift of degeneracy between the different  $M_S$  component of a same  $S$  state can be observed even in the absence of magnetic field, this phenomenon is called Zero-Field-Splitting.

The associated spin Hamiltonian is written:

$$\hat{H}_{ZFS} = \hat{\mathbf{S}} \cdot \overline{\overline{D}} \cdot \hat{\mathbf{S}} \quad (2.1.5)$$

where  $\hat{\mathbf{S}}$  is the spin vector of the ground state and  $\overline{\overline{D}}$  is a two rank symmetric tensor. In an arbitrary axis frame, it is composed of six different parameters.

$$\overline{\overline{D}} = \begin{pmatrix} D_{xx} & D_{xy} & D_{xz} \\ D_{xy} & D_{yy} & D_{yz} \\ D_{xz} & D_{yz} & D_{zz} \end{pmatrix} \quad (2.1.6)$$

This tensor can be reduced to three parameters by diagonalization, *i.e.* expressing them in the tensor principal axes that define the magnetic anisotropy axes. Going further as to work with traceless tensors allow us to use only two parameters, by convention the z-axis is taken as the main magnetic axis with D the axial parameter:

$$D = D_{zz} - \frac{1}{2}(D_{xx} + D_{yy}) = \frac{3}{2}D_{zz} \quad (2.1.7)$$

and the rhombic term:

$$E = \frac{1}{2}(D_{xx} - D_{yy}) \quad (2.1.8)$$

With  $|D| \geq 3E \geq 0$ . The ZFS Hamiltonian can then be written:

$$\hat{H}_{ZFS} = D(\hat{S}_z^2 - \frac{1}{3}\hat{S}^2) + E(\hat{S}_x^2 - \hat{S}_y^2) \quad (2.1.9)$$

A positive value of D indicates that the ground state is mainly composed of the  $M_S=0$  component meaning that the projection of the spin moment along the z-axis is close to zero resulting in an easy-plane anisotropy. On the contrary if  $D < 0$ , the ground state is formed from the  $M_S=\pm M_{Smax}$  components with a maximum projection of spin moment along the z-axis resulting in an easy-axis anisotropy.

In the case of a triplet S=1 ground state such as for a Ni (II) complex, in an arbitrary axes frame ( $x, y, z$ ), the matrix representation of hamiltonian (2.1.5) writes:

$H_{ZFS}$	$ 1, -1\rangle$	$ 1, 0\rangle$	$ 1, 1\rangle$
$\langle 1, -1  $	$\frac{1}{2}(D_{xx} - D_{yy}) + D_{zz}$	$-\frac{\sqrt{2}}{2}(D_{xz} + iD_{yz})$	$\frac{1}{2}(D_{xx} - D_{yy} + 2iD_{xy})$
$\langle 1, 0  $	$-\frac{\sqrt{2}}{2}(D_{xz} - iD_{yz})$	$D_{xx} + D_{yy}$	$\frac{\sqrt{2}}{2}(D_{xz} - iD_{yz})$
$\langle 1, 1  $	$\frac{1}{2}(D_{xx} - D_{yy} - 2iD_{xy})$	$\frac{\sqrt{2}}{2}(D_{xz} - iD_{yz})$	$\frac{1}{2}(D_{xx} + D_{yy}) + D_{zz}$

In the magnetic axes frame (X, Y, Z), this matrix becomes:

$H_{ZFS}$	$ 1, -1\rangle$	$ 1, 0\rangle$	$ 1, 1\rangle$
$\langle 1, -1  $	$\frac{1}{2}(D_{XX} + D_{YY}) + D_{ZZ}$	0	$\frac{1}{2}(D_{XX} - D_{YY})$
$\langle 1, 0  $	0	$D_{XX} + D_{YY}$	0
$\langle 1, 1  $	$\frac{1}{2}(D_{XX} - D_{YY})$	0	$\frac{1}{2}(D_{XX} + D_{YY}) + D_{ZZ}$

Removing the trace from the tensor and applying the convention from eq(2.1.7) and eq(2.1.8) we get:

$H_{ZFS}$	$ 1, -1\rangle$	$ 1, 0\rangle$	$ 1, 1\rangle$
$\langle 1, -1 $	$\frac{1}{3}D$	0	E
$\langle 1, 0 $	0	$\frac{2}{3}D$	0
$\langle 1, 1 $	E	0	$\frac{1}{3}D$

Note that in the case of an even number of unpaired electrons, the D and E parameters can be estimated directly from the energy spectrum. Note that in

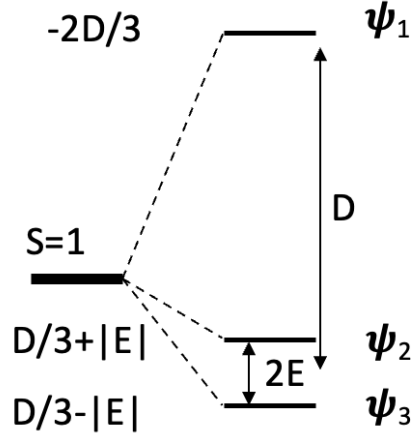


Figure 2.1: Schematic representation of the three lowest SO-state undergoing ZFS in the case of triplet ground state.

this case ( $S=1$ ) the D and E parameters can be estimated directly from the energy spectrum represented in Figure 2.1. Indeed, diagonalizing the model Hamiltonian matrix gives the three eigenvalues: In the case of a triplet ground state, diagonalizing the model Hamiltonian matrix gives the three eigenvalues:

$$E_1 = -\frac{2}{3}D \quad (2.1.10)$$

$$E_2 = \frac{1}{3}D + E \quad (2.1.11)$$

$$E_3 = \frac{1}{3}D - E \quad (2.1.12)$$

with the eigenvectors:

$$\psi_1 = |1, 0\rangle \quad (2.1.13)$$

$$\psi_2 = \frac{1}{\sqrt{2}}(|1, -1\rangle + |1, 1\rangle) \quad (2.1.14)$$

$$\psi_3 = \frac{1}{\sqrt{2}}(|1, -1\rangle - |1, 1\rangle) \quad (2.1.15)$$

leading to the extraction of the D and E terms directly from the calculated or measured energy differences:

$$D = \frac{1}{2}(E_2 + E_3) - E_1 \quad (2.1.16)$$

and

$$E = \frac{1}{2}(E_2 - E_3) \quad (2.1.17)$$

For the study of system with a ground state of  $S < 2$  these two parameters are enough to reproduce exactly the energy spectrum. In case of larger  $S \geq 2$ , one needs to introduce the Stevens operators which are linked to the crystal field and can be expressed from angular momenta operators  $\hat{J}$ . These operators were first derived to describe the lift of degeneracy induced by the crystal field potential studied in spectroscopy. Note that this formalism is not restricted to transition metals and is often used for lanthanides and actinides complexes. The ZFS is now described by a more complete model Hamiltonian:

$$\hat{H}_{Stevens} = \sum_{k=0}^{2S} \sum_{n=0}^k B_k^n \hat{O}_k^n \quad (2.1.18)$$

where  $B_k^n$  are the Stevens parameter specific to each systems and  $\hat{O}_k^n$  the Stevens Operators are spherical tensors of rank  $k$ . In case of mononuclear complexes, only the even rank  $k$  tensors contribute for symmetry reasons. The ZFS parameters are related to the second rank Stevens parameters:

$$D = 3B_2^0 \quad E = B_2^2 \quad (2.1.19)$$

### 2.1.3 Magnetic anisotropy in polynuclear complexes

Opening the study to multiple magnetic centers introduces couplings that can be anisotropic between the magnetic moments of each centre. This coupling between two sites A and B with at least one magnetic electron each, is called anisotropic exchange interaction and is described by the following Giant Spin Hamiltonian.

$$\hat{H}_{AB} = \hat{\mathbf{S}}_A \cdot \overline{\overline{D}} \cdot \hat{\mathbf{S}}_B \quad (2.1.20)$$

The interaction tensor  $\overline{\overline{D}}$  describes Zero-Field-Splitting the same way as before but now between two sites  $A$  and  $B$ , two parameters  $D$  and  $E$  can be defined

similarly. This Hamiltonian is suitable for system with a ground state of spin larger or equal to one well separated in energy from other SO-states. This tensor can be split in three components, an isotropic term that relates to the HDvV Hamiltonian and two anisotropic terms. It is then possible to study all the states of the configuration using the multi-spin Hamiltonian:

$$\hat{H}_{AB} = J(\hat{\mathbf{S}}_A \cdot \hat{\mathbf{S}}_B) + \hat{\mathbf{S}}_A \cdot \overline{\overline{D}}_{AB} \cdot \hat{\mathbf{S}}_B + \mathbf{d}_{AB} \cdot (\hat{\mathbf{S}}_A \times \hat{\mathbf{S}}_B) \quad (2.1.21)$$

where  $J$  is the isotropic coupling constant found in the HDvV Hamiltonian 2.1.1. The two following terms describe the anisotropic exchange with the symmetric tensor of exchange  $\overline{\overline{D}}_{AB}$  and the antisymmetric exchange  $\mathbf{d}_{AB}$  also called Dzyaloshinskii-Moriya pseudo-vector interaction. For couplings involving more than one unpaired electron per site, local tensor must be introduced:

$$\hat{H}_{AB} = J(\hat{\mathbf{S}}_A \cdot \hat{\mathbf{S}}_B) + \hat{\mathbf{S}}_A \cdot \overline{\overline{D}}_{AB} \cdot \hat{\mathbf{S}}_B + \mathbf{d}_{AB} \cdot (\hat{\mathbf{S}}_A \times \hat{\mathbf{S}}_B) + \hat{\mathbf{S}}_A \cdot \overline{\overline{D}}_A \cdot \hat{\mathbf{S}}_A + \hat{\mathbf{S}}_B \cdot \overline{\overline{D}}_B \cdot \hat{\mathbf{S}}_B \quad (2.1.22)$$

The matrix representation for two interacting spin 1/2 systems is the following:

$H_{MS}$	$ 1, -1\rangle$	$ 1, 0\rangle$	$ 1, 1\rangle$	$ 0, 0\rangle$
$\langle 1, -1  $	$\frac{J}{4} + \frac{D_{zz}}{4}$	$\frac{D_{xz}-iD_{yz}}{2\sqrt{2}}$	$\frac{(D_{xx}-D_{zz}-2iD_{xy})}{4}$	$\frac{d_y+id_x}{2\sqrt{2}}$
$\langle 1, 0  $	$\frac{D_{xz}+iD_{yz}}{2\sqrt{2}}$	$\frac{J}{4} - \frac{D_{zz}}{4} + \frac{(D_{xx}+D_{yy})}{4}$	$-\frac{D_{xz}-iD_{yz}}{2\sqrt{2}}$	$-\frac{id_z}{2}$
$\langle 1, 1  $	$\frac{(D_{xx}-D_{zz}+2iD_{xy})}{4}$	$-\frac{D_{xz}+iD_{yz}}{2\sqrt{2}}$	$\frac{J}{4} + \frac{D_{zz}}{4}$	$\frac{d_y-id_x}{2\sqrt{2}}$
$\langle 0, 0  $	$\frac{d_y-id_x}{2\sqrt{2}}$	$\frac{id_z}{2}$	$\frac{d_y+id_x}{2\sqrt{2}}$	$-\frac{3J}{4} - \frac{D_{zz}}{4} - \frac{(D_{xx}+D_{yy})}{4}$

From this matrix, we notice that the Dzyaloshinskii-Moriya interaction creates a coupling between the singlet with the three  $M_S$  components of the triplet state. As for the symmetric tensor of anisotropic exchange, it only couples the three component of the triplet which undergo an energy splitting. At the isotropic level, the difference between the triplet and singlet states is given by  $\Delta E = J$ , but with the inclusion of the anisotropic terms this becomes much more complex. As opposed to the Zero-Field Splitting mechanism, it is impossible to obtain values for these interactions from the energy spectrum only, as such they will be extraced from the effective Hamiltonian theory. Note that this Hamiltonian 2.1.22 is not restricted to a ground state with  $S \geq 1$ .

## 2.2 Methodology

All types of calculations discussed here after have for purpose to solve, in some way, the Schrodinger Equation:

$$\hat{H}\Psi_i = E_i\Psi_i \quad (2.2.1)$$

where  $\hat{H}$  is an Hamiltonian used to describe the system,  $E_i$  is the energy associated to the wave-function  $\Psi_i$ . The solutions  $E_i$  of this problem are obtained pretty straightforwardly by diagonalizing the Hamiltonian matrix, except that in most cases, the  $\Psi_i$  vector are not known beforehand. The Hamiltonian treated during the calculations is called exact electronic Hamiltonian as it considers all electronic and nuclear interactions of the system, it is written as follow, in atomic units:

$$\hat{H} = -\frac{1}{2} \sum_{i=1}^N \nabla_i^2 - \sum_{A=1}^M \frac{1}{2M_A} \nabla_A^2 - \sum_{i=1}^N \sum_{A=1}^M \frac{Z_A}{|r_i - R_A|} + \sum_{i=1}^N \sum_{j < i}^N \frac{1}{r_{ij}} + \sum_{A=1}^M \sum_{B > A}^M \frac{Z_A Z_B}{|R_A - R_B|} \quad (2.2.2)$$

where  $r_i$  is the position vector of the  $i$ th electron,  $R_A$  the position vector of the  $A$ th nucleus with atomic number  $Z_A$  and mass  $M_A$ . This Hamiltonian can be simplified in the context of the Born-Oppenheimer approximation, in which the electrons are considered to adapt instantly to the movement of the nuclei. This allows to decouple the movement of the electrons from that of the nuclei, whose position can be fixed at the equilibrium (or any other geometry). Note that once the electronic energies and wave-function have been obtained for different geometries, it is also possible to study the nuclei motion within this approximation. This approximation is justified with the fact that the electrons are much lighter than the nuclei.

$$\hat{H}_{elec} = -\frac{1}{2} \sum_{i=1}^N \nabla_i^2 - \sum_{i=1}^N \sum_{A=1}^M \frac{Z_A}{|r_i - R_A|} + \sum_{i=1}^N \sum_{j < i}^N \frac{1}{|r_i - r_j|} \quad (2.2.3)$$

This Hamiltonian describes the electronic problem while the nuclei contribution, last term from eq 2.2.2 is a constant, having for only effect a shift in the overall energy spectrum. While this greatly simplifies the equations, it is still not solvable analytically and several approximations were developed to tackle this

problem. All the methods used in this work rely on the construction of molecular orbitals (**MO**) as expansions of atomic orbitals (**AO**).

$$\psi_k = \sum_i c_i \phi_i \quad (2.2.4)$$

Where  $\psi_k$  is the  $k$ th MO built from the AOs  $\phi_i$  with coefficient  $c_i$ . This expansion relies on a infinite number of AO but in real case application this is not achievable and will thus be restricted to a finite number of basis functions. As the electronic Hamiltonian does not include any information about spin, it will be included within a so called spin orbital with the introduction of two orthonormal functions  $\alpha(\omega)$  and  $\beta(\omega)$ , *i.e.* spin up or down function, with  $\omega$  a dummy variable. From each spatial molecular orbital, two spin orbitals can be created such that:

$$\chi_i = \begin{cases} \psi_i(r)\alpha(\omega) \\ \text{or} \\ \psi_i(r)\beta(\omega) \end{cases} \quad (2.2.5)$$

This definition for the spin orbital is well adapted for close-shell systems where all molecular orbitals are doubly occupied, the spatial part for any spin orbital is the same for both spin function defining the restricted formalism. A commonly used notation in this formalism is to refer to a spin orbital by its spatial component and indicate the spin function with an overline, *i.e.*  $\chi_i = \psi_i(r)\alpha(\omega) = \overline{\psi}_i(r)$  or  $\chi_i = \psi_i(r)\beta(\omega) = \overline{\psi}_i(r)$ . Such definition changes when working with open shell system, *i.e.* some orbitals are singly occupied necessitating the application of unrestricted formalism.

### 2.2.1 Hartree-Fock Method

The cornerstone of *ab initio* calculation in quantum chemistry is the Hartree-Fock method which is usually the initial step for computing a first approximation of the wave-function in molecules. It is a variational approach that aims to treat the N-electron problems as a problem of N non interacting electrons in the presence of an average potential replicating interactions between them, it is in this sense a mean-field theory. This wave-function is constructed on the

optimisation of a single Slater determinant  $\Psi$ :

$$|\Psi(x_1, x_2, \dots, x_N)| = \frac{1}{\sqrt{N!}} \begin{vmatrix} \chi_i(x_1) & \chi_j(x_1) & \cdots & \chi_k(x_1) \\ \chi_i(x_2) & \chi_j(x_2) & \cdots & \chi_k(x_2) \\ \vdots & \vdots & & \vdots \\ \chi_i(x_N) & \chi_j(x_N) & \cdots & \chi_k(x_N) \end{vmatrix} \quad (2.2.6)$$

where  $\chi_i$  are spin orbitals and the variable  $x_i = \{r_i, \omega_i\}$ , it involves all combination of all  $N$  electrons in all  $k$  spin orbitals. We introduce the shorthand notation for such determinant  $|\Psi(x_1, x_2, \dots, x_N)| = |\chi_1(x_1)\chi_2(x_2)\dots\chi_N(x_N)|$  showing only the diagonal elements of the determinant.

The way to obtain the best adapted Hartree-Fock wave-function, *i.e.* the molecular orbitals, comes through the resolution of the Roothan's equation:

$$FC = SC\epsilon \quad (2.2.7)$$

$S$  is the overlap matrix of the basis function,  $\epsilon$  the matrix of orbital energies and  $C$  is the matrix of the trial vector. The Fock operator  $F$  is defined as:

$$\hat{F}(i) = \hat{h}(i) + \sum_j^{N/2} [2\hat{J}_j(i) - \hat{K}_j(i)] \quad (2.2.8)$$

where  $\hat{h}(i)$  is a mono-electronic operator that contains the kinetic energy operator of the  $i$ th and the coulomb repulsion with the fixed nuclei. The two operators  $\hat{J}_j(i)$  and  $\hat{K}_j(i)$  describe the coulomb repulsion and exchange mechanism between the  $i$ th electron and the rest. These operator carry a direct dependance on the trial vectors from eq 2.2.7 as such, the Roothan's equation are non-linear and will be solved iteratively following a *Self Consistent Field* (SCF) procedure.

## 2.2.2 Configuration Interaction

A single Hartree-Cok determinant provides a good starting point for the wave-function but fails to describe properties associated with open-shell systems. For most of magnetic systems, a single reference wave-function is not enough as the system is usually not closed shell and has one or more unpaired electrons. Hence, its ground state is described by a wave-function composed of several determinants. The most straightforward way to compute such a wave-function

is to perform a full Configuration Interaction calculation. This method relies on the diagonalisation the N-electron Hamiltonian in a basis of N-electron functions (Slater Determinants). In other word, each configurations of N-electrons in the  $k$ -spin orbitals is considered and added to the wave-function. With a complete basis, the energy obtained would be exact in the Born-Oppenheimer approximation and solve the N-electron problem. However, this is not applicable due to the finite nature of our calculation as we cannot handle infinite basis set. Still, full CI calculations are possible on some systems and provide a good upper bound to the exact energy.

The determinant  $|\psi_0\rangle$  is a Slater determinant describing the case where electrons occupy the lowest orbitals obtained by a Hartree-Fock calculation. The determinant  $|\psi_a^r\rangle$  describes the configuration where an electron from orbital  $a$  is excited to orbital  $r$ . In the same way, all the excitations are taken into account and the generated determinants are used as the basis for the many-electron wave function  $|\Psi_0\rangle$

$$|\Psi_0\rangle = c_0|\psi_0\rangle + \sum_{ar} c_a^r |\psi_a^r\rangle + \sum_{\substack{a < b \\ r < s}} c_{ab}^{rs} |\psi_{ab}^{rs}\rangle + \dots \quad (2.2.9)$$

As the number of determinants grows factorially with the number of electrons and the basis set (*i.e.* the number of orbitals), this is very costly calculation wise. This method is thus only applicable on small systems where the number of electrons and the basis sets used are small. This is not the case for the systems studied in this work, so the need to decrease the computational time is of importance. One can see from the wave function computed, that a significant number of determinants do not play a big role in the physics of the wave function. The ones with high excitations should appear with little weight unless high excited states are computed, therefore they can be left out of the wave-function without removing too much of physical relevance. Most of the studies in this work concern systems based on 3d-transition metals. The main focus is on the characterisation of the ground state, which is mainly carried by the metal's 3d orbitals, as well as the excited states at the bottom of the spectrum resulting from excitations within these orbitals. It becomes clear that in these systems, most of the determinants taken into account in eq 2.2.9 do not play an important role in the physics of the system.

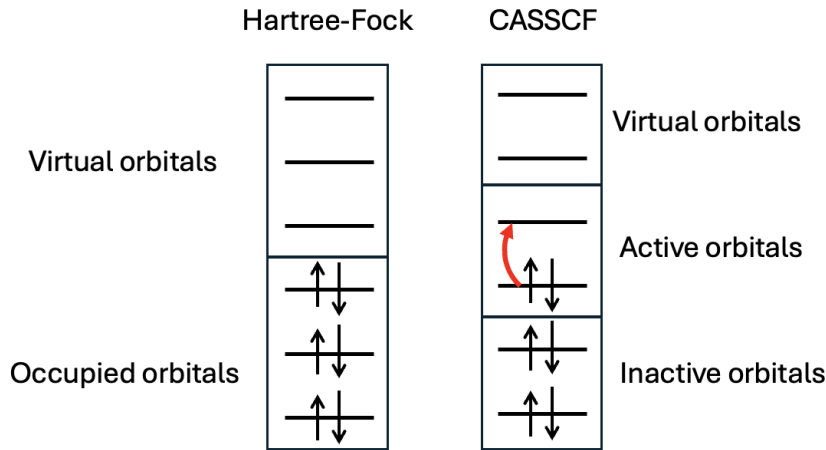


Figure 2.2: Difference between the orbitals space in Hartree-Fock and CASSCF Theory

### 2.2.3 Complete Active Space Self Consistent Field

One of the most used method to introduce multiple references in the wave-function is called *Complete Active Space Self Consistent Field* (*CASSCF*). Compared to the Hartree-Fock theory where two types of orbitals (occupied and unoccupied) are considered, in CASSCF theory orbitals are separated in three sub-spaces. The inactive orbitals are doubly occupied throughout the calculation, virtual orbitals will stay empty while the active orbitals have a variable occupancy ranging from zero to two electrons. These active orbitals (and the active electrons they bear) define the active space into which a configuration interaction will be realised considering all the possible determinants within this sub-space. As the number of determinants grows significantly with the number of active electrons and orbitals, this method is still costly and its size becomes a limiting factor for the calculations. The new wave-function is now written as an expansion of Slater determinants which is obtained via a SCF procedure where both the expansion coefficients and the orbitals are optimised as to minimize the ground state energy or of several states in an "average" way. This dual optimisation scheme can render the convergence troublesome, as such the definition of the active space and the choice of the starting orbitals become crucial. One usually starts from a set of orbitals previously obtained via an Hartree-Fock calculation. For computation of magnetic properties in transition metal systems, the minimum active space should consists of the

magnetic orbitals, *i.e.* the singly occupied d-orbitals of the metallic centers, this can later be extended to all of the 3-d orbitals of the metal as well as some orbitals of the ligands. As a result of the CASSCF method we obtain the energies of all states included in the calculation and a new set of orbitals into which they are expressed. Note that depending on the computational code used, the sets of orbitals may be *specific* to a single state or *averaged* to lower the average energy of all of the states computed. This calculation takes into account the correlation between the electrons inside the active space in the mean field created by the other electrons. While this method provides the non-dynamical correlation, it fails to capture the correlation with the inactive electron and their response to excitations, called dynamical correlation which plays a crucial work in the physics of magnetic systems.

#### 2.2.4 Perturbation Theory

Perturbative treatment can be applied to extract the dynamical correlation brought by the mono and diexcitations that is left out from simple CASSCF calculation. For such calculation, one can use the CASPT (Complete Active Space Perturbation theory) or the NEVPT (N-electron valence state perturbation theory). Both of these methods rely on the assumption that the Hamiltonian can be partitioned into a zeroth-order term and a perturbation with the parameter  $\lambda$ :

$$\hat{H} = \hat{H}^{(0)} + \lambda \hat{H}^{(1)} + \lambda^2 \hat{H}^{(2)} + \dots \quad (2.2.10)$$

The wave-function and energy are expanded in a similar way and the zeroth order term  $\Psi_{(0)}^0$  is chosen to be the CASSCF wave-function. The effect of the configurations outside of the active space on the energy and the wave-function is estimated though perturbation theory and the expansions of the equations allows one to obtain the corrected energies, usually at second-order of perturbation with CASPT2 or NEVPT2. These two methods mainly differ from the choice of the zeroth-order Hamiltonian, CASPT2 rely on a monoelectronic Hamiltonian built from a one electron Fock operator that falls back to the Moller-Plesset Hamiltonian in single reference case. This treatment may lead to what is called "intruder states" coming from divergence in the denominator of the corrections term where a difference of orbital energy is taken. Several approach have been adapted such as the introduction of *level shifts*, real or

imaginary, as to fix this divergence. In case of NEVPT2, the zeroth-order Hamiltonian is a bi-electronic (Dyall) Hamiltonian which in itself include a shift in energy between state from inside or outside the active space preventing the appearance of intruder states. One should add that the corrections are considered to be contracted (NEVPT2 proposes both fully and partially contracted scheme) as these methods do not act upon the coefficients inside the wave-functions but only on the energies.

### 2.2.5 Difference dedicated configurational interaction

Another way to retrieve the dynamical correlation that is lost in CASSCF calculation is apply a Configuration Interaction restricted to the mono and diexcitations considered in perturbation theory. This method allows the introduction of new determinants in the wave-function that do not belong to the CASSCF space, this way not only the energies but the wave-functions are revised. While very promising, the size of the system remains a limiting factor because of the number of determinants to include in the CI expansion, the cost of calculation becoming too high, one has to truncate the CI space even more. Restricting the CI to all the simple and double excitations is still computationally demanding as the double excitation are too numerous, but some of them can be left out of the calculations. These excitations are classified into eight categories depending on the number of hole/particle created, they are represented on Figure 2.3. A hole is an excitation from an inactive orbital to an active or virtual orbital, while a particle is an excitation from an active or inactive orbital to a virtual one.

The most troublesome excitations are the one generating two holes and two particles (2h-2p) as they are the most numerous, but it can be shown at second-order of perturbation that, as long as a common set of MO is used, they do not contribute to the energy difference between states but only act as a shift of the diagonal energies. As such they can be neglected giving rise to a variant of MRCI called Difference-Dedicated-Configurational-Interaction (DDCI). Three sub-variant of DDCI exists taking into account different classes of excitations as pictured on fig 2.3 It has been established that the extraction of magnetic coupling involving bridging ligand requires the use of the DDCI3 method to provide good estimates.

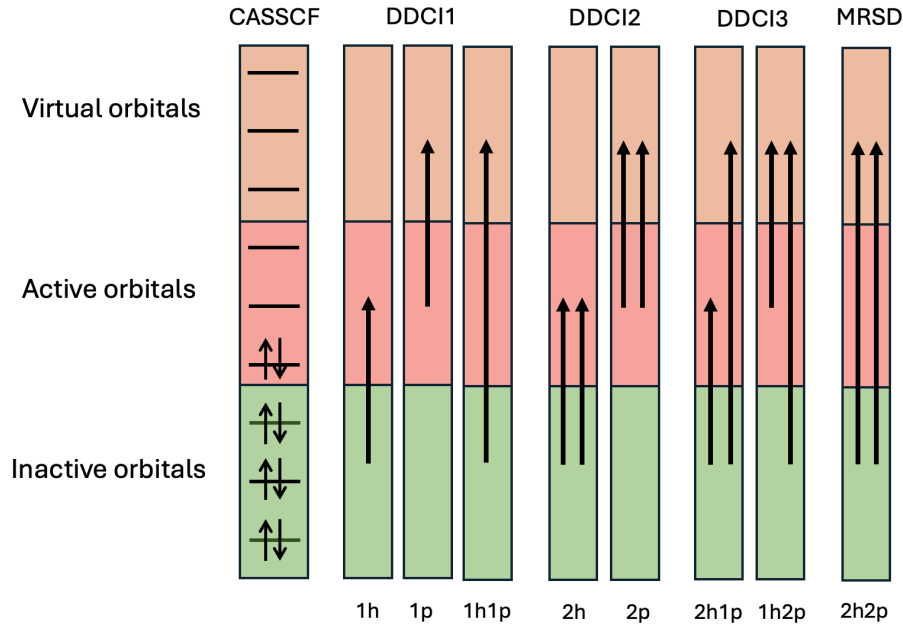


Figure 2.3: Classes of excitations and associated DDCI method

### 2.2.6 Density functional theory

Another way to get a description of the electronic structure is through density functional theory (DFT). The main interest of such a method is the description of the ground state properties through the determination of the ground state energy  $E_0$  following the variational theorem:

$$E_0 = \min \langle \Psi | \hat{H} | \Psi \rangle \quad (2.2.11)$$

Here, the electronic wave-function of the molecule  $\Psi$  is approximated to a single Slater determinant obtained from the determination of the electronic density  $\rho(\mathbf{r})$ :

$$\rho(\mathbf{r}) = N \int |\Psi(\mathbf{x}_1 \dots \mathbf{x}_N)|^2 ds_1 dx_2 \dots dx_N \quad (2.2.12)$$

The Hamiltonian 2.2.2 can be written:

$$\hat{H} = \hat{T} + \hat{V}_{ee} + \hat{V}_{ne} \quad (2.2.13)$$

with  $\hat{T}$  the kinetic energy operator,  $\hat{V}_{ee}$  the electron-electron interaction operator and  $\hat{V}_{ne}$  the nuclei-electron interaction operator. By replacing  $v_{ne}(\mathbf{r})$  with a known external potential  $v(\mathbf{r})$ , one can obtain the ground state wave-function  $\Psi$  by solving the Schrödinger equation and the electron density follows. The

first Hohenberg-Kohn theorem states that this external potential is a unique functional of the electron density. As such, knowing the electron density allows to determine the properties of the ground states. The second Hohenberg-Kohn gives, in case of non degenerate ground state, that the wave-function  $\Psi$  is itself a functional of  $\rho(\mathbf{r})$  which allows to define the total energy:

$$E[\rho] = F[\rho] + \int \rho(\mathbf{r})v(\mathbf{r})d\mathbf{r} \quad (2.2.14)$$

with  $F[\rho]$  a universal density functional which contains the kinetic and potential contributions. The ground state energy  $E_0$  is the minimum of eq 2.2.14 which is reached when the electron density  $\rho_0(\mathbf{r})$  is that of the ground state. In theory the knowledge of the electron density allows to determine  $E_0$ , however the density dependence expression of  $F[\rho]$  is not known.

$$F[\rho] = T[\rho] + V_{ee}[\rho] \quad (2.2.15)$$

Kohn and Sham introduced new definition of this functional by replacing the interacting system with a fictitious system of  $N$  non interacting electrons. The functional becomes:

$$F[\rho] = T_s[\rho] + J[\rho] + E_{xc}[\rho] \quad (2.2.16)$$

where  $T_s[\rho]$  is the non-interacting kinetic energy functional of density  $\rho$  expressed in the basis of  $\phi_i(\mathbf{r})$  that are built to reproduce the ground state density  $\rho_0(\mathbf{r})$ .

$$\rho_0(\mathbf{r}) = \sum_i^N |\phi_i(\mathbf{r})|^2 \quad (2.2.17)$$

$$T_s[\rho] = \sum_i^n \langle \phi_i | -\frac{1}{2} \nabla^2 | \phi_i \rangle \quad (2.2.18)$$

The Hartree-potential  $J[\rho]$  gives the coulomb repulsion between electrons pair:

$$J[\rho] = \frac{1}{2} \int \int \frac{\rho(\mathbf{r}_1)\rho(\mathbf{r}_2)}{|\mathbf{r}_2 - \mathbf{r}_1|} d\mathbf{r}_1 d\mathbf{r}_2 \quad (2.2.19)$$

The energy expression eq 2.2.14 finally becomes:

$$E[\rho] = \int v(\mathbf{r})\rho(\mathbf{r})d\mathbf{r} + T_s[\rho] + J[\rho] + E_{xc}[\rho] \quad (2.2.20)$$

This definition gives the exact energy given that the expression of the Exchange-Correlation  $E_{xc}$  is known, unfortunately this is not the case. Over the years

multiple attempts have been made to find a universal expression of  $E_{xc}$  in terms of  $\rho$  and its derivative. In the most basic approach, called Local Density Approximation (LDA), the system is taken to behave as a uniform electron gas where  $E_{xc}$  depends only in the density  $\rho$ . This model was later adapted to study different spin configuration with the Local Spin Density Approximation (LSDA). Other attempts tried to improve the functional by incorporating a dependance in the derivative of  $\rho$  with the Generalized Gradient Approximation (GGA) or a small portion of the Hartree-Fock exact exchange in what is called hybrid functionals.

### 2.2.7 Inclusion of Spin-Orbit effects

As the goal of this thesis is the characterisation of the magnetic anisotropy, which is a direct consequence of relativistic mechanisms, it is crucial to include the most important ones in our calculation, namely spin-orbit coupling. Following the already established procedure, a two-step approach is chosen for this work. It relies on the computation of the spin-orbit free states, that are independant from spin-orbit, using CASSCF or post-CASSCF method as the first step. The spin-orbit is then included *a posteriori* following the State-Interaction method. This method computes the interaction matrix, based on the application of the Breit-Pauli coupling operator on the different  $M_S$  component of all the states included in the calculation. This matrix is then diagonalised to obtain the "spin-orbit" states and their corresponding energies. The Breit-Pauli spin-orbit coupling operator is the sum of a mono- and bielectronic term. This operator is usually treated in a mean field approximation, where the operator is written as an effective one-electron operator:

$$\hat{H}^{SO} = \sum_i \xi_i(\mathbf{r}_i) \hat{l}_i \cdot \hat{s}_i \quad (2.2.21)$$

where  $\xi_i$  is the effective spin-orbit constant,  $\hat{l}_i$  is the angular momenta operator and  $\hat{s}_i$  the spin momenta operator. The application of this Hamiltonian rely on the computation of the Atomic Mean Field Integral (AMFI). The effective spin-orbit constant  $\xi$  should yield different value depending on which electron is treated. For the rationalisation, a unique tabulated value of  $\xi$  will be used for all electrons.

### 2.2.8 Embedded Cluster Method

In the case of molecules, the study of magnetic anisotropy is well described by single molecule calculations as these interactions are localised between the metallic centers and ligands. The restricted size of the molecule generally allows for an explicit treatment of all the atoms involved. The same cannot be said about crystalline systems which are infinite and cannot be treated that way by the methods chosen in this work, as such we have to work on smaller part called "cluster" or "fragment". In theory one would want the fragment to be as large as possible to reduce the error created by cutting off the fragment from its environment, unfortunately to reduce computational cost we have to limit ourselves with small sized fragments. It then becomes crucial to chose correctly the fragment based on our knowledge of the physics we want to reproduce. The properties of the cluster alone differ from the one inside its natural environment. To reproduce it accurately it is immersed inside an embedding. This embedding is composed of point charges that aim to replicate the electrostatic field of the crystal, called Madelung Field, inside the cluster region. To keep the symmetries of the crystal, the point charges are positionned at the lattice site in a sphere of radius  $R_c$ . Another problem in selecting fragments in ionic crystal

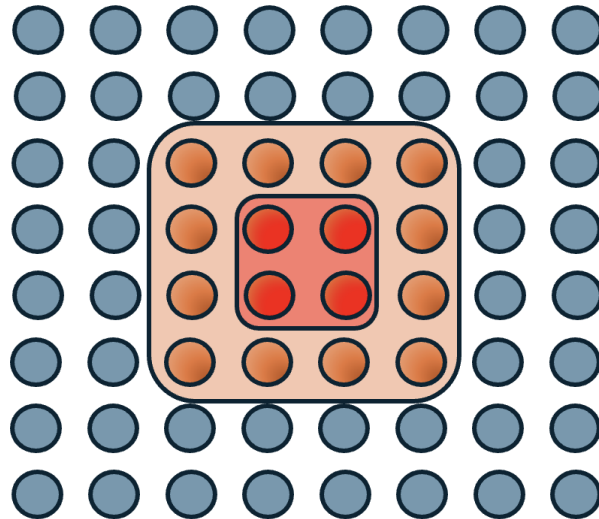


Figure 2.4: Schematic representation of the three region composing the embedding. red: cluster, orange: TIPS, blue: point charges

is the overall charge of the fragment. The centre of the study is the metallic ions, charged positively, forming ionic bonds with negatively charged ligands. A correct description of these magnetic centres requires to include all closest

neighbors which often makes the overall fragment negatively charged. The ions outside the border of the fragment, replaced by point charges, are then positive. This induces a polarization of the electron density of the anions bordering the cluster. To avoid the electrons escaping the fragment, pseudo-potentials are placed at the lattice sites near the fragment to act as walls which prevent electrons from approaching these positive charges as if they were real atoms. These potentials are called Total-Ion-Potentials (TIPS) and can be either *ab initio* model potential (AIMP) or Effective Core Potential (ECP) depending on which Quantum Chemistry software is used.

Two procedures were explored to create such embedding:

- (1) Formal charges were used in a sphere with very large  $R_c$  (around 50 Å).
- (2) Optimised point charges were obtained using Ewal Summation from formal charges, this allows to reduce the  $R_c$  to a few angstrom around the fragment.

All of this is done to ensure that the properties extracted from the fragment calculations, *i.e.* for a finite system, are a good representation of the crystal properties, *i.e.* for an infinite system.

### 2.2.9 Effective Hamiltonian Theory

Having ways to compute the *ab initio* multi-reference wave-functions usually leads to lengthy expressions where the wave-function is spanned along a large number of Slater determinants making its analysis complicated. On the other hand, the model Hamiltonian works in a much smaller space where a small number of electrons is used to introduce effective interactions. A way to connect the two Hamiltonians is to apply a theory developed by Bloch called Effective Hamiltonian theory. Its purpose is to build an effective Hamiltonian whose eigenvalues and eigenvectors reproduce the energy spectrum and wave-functions of the *ab initio* Hamiltonian but using a much smaller number of eigenfunctions.

Starting from the Schrodinger equation with the Born-Oppenheimer Hamiltonian  $\hat{H}$ :

$$\hat{H} |\Psi_m\rangle = E_m |\Psi_m\rangle \quad (2.2.22)$$

where  $\Psi_m$  are the eigenvectors with the associated eigenvalue  $E_m$  forming the space  $S$  of size  $N$ . We define a smaller space  $S_0$  called model space with  $N_0$  states  $|\phi_i\rangle$ , this space is usually composed of the low lying states where the

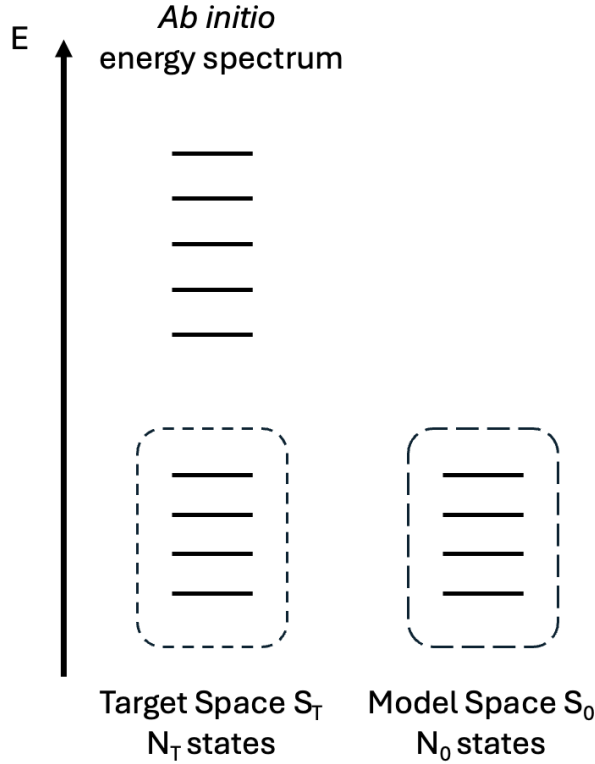


Figure 2.5: Schematic representation of the three spaces involved in effective Hamiltonian theory

model Hamiltonian will be developed. An effective Hamiltonian  $H_{eff}$  is built to reproduce the energy spectrum of the exact Hamiltonian in the target space  $S_T$  using a small number of low-lying states  $\tilde{\Psi}_m$  such that:

$$\hat{H}_{eff} |\tilde{\Psi}_m\rangle = E_m |\tilde{\Psi}_m\rangle \quad (2.2.23)$$

This target space  $S_T$  is chosen to be of the same size as the model space  $S_0$  allowing for direct comparison.

The first step is to project the eigenfunctions  $\Psi_m$  onto the model space using the projector:

$$\hat{P}_0 = \sum_m^{N_0} |\tilde{\phi}_m\rangle \langle \tilde{\phi}_m| \quad (2.2.24)$$

$$|\tilde{\Psi}_m\rangle = \hat{P}_0 |\Psi_m\rangle \quad (2.2.25)$$

These eigenvectors are not necessarily orthogonal leading to a non-Hermitian Hamiltonian, this is problematic when comparing to the model Hamiltonians

which are Hermitians. In this work, we apply the formalism proposed by Des Cloizeaux where the vectors are symmetrically orthogonalized from the overlap matrix  $S$ :

$$|\tilde{\Psi}_m^\perp\rangle = S^{-1/2} |\tilde{\Psi}_m\rangle \quad (2.2.26)$$

At this point, it is possible to check the quality of the model space by calculating the norm of the projected vectors present in the  $S$  matrix. If too small, the interactions of the system are not captured correctly by the model space making it inadequate.

When these projections are close to one, we can consider the model space adequate, the effective Hamiltonian is then built:

$$H_{eff} = \sum_m^N |\tilde{\Psi}_m^\perp\rangle E_m \langle \tilde{\Psi}_m^\perp | \quad (2.2.27)$$

Once this is done, this numerical matrix  $H_{eff}$  constructed from the *ab initio* exact Hamiltonian are compared to the model Hamiltonian representation matrix. This allows for the extraction of values for the model Hamiltonian parameters as well as a test of validity. If there is too much deviation between the two matrices, it is possible that there is some missing interaction in the model. In such a case, analytical derivation allows one to derive a new Hamiltonian from a more sophisticated Hamiltonian.

# Chapter 3

## Study of the magnetic anisotropy in mononuclear complexes

The field of mononuclear complexes is a perfect area for the study of magnetic anisotropy. The finite size of such complexes as well as the localised character of the magnetic entities allow for the explicit treatment of all atoms at play with reasonable computational cost. This combined with the large amount of experimental data available enable for the validation of models and computational methodology. Numerous studies have been dedicated to the ability of the ZFS Hamiltonian to model the behaviour of mononuclear complexes based on fourth period transition metals. It has established that the value of the ZFS parameters are highly dependant on the metallic ion nature and charge, its d-shell configuration, and its environment which impact the energy difference of the d-orbitals. The ligands around the metallic centre becomes a crucial choice that dictates some of the complex properties as we will see in this chapter.

State of the art methodology for such studies is to generate a wave-function starting from a CASSCF calculation. This should include all electronic states generated by an active space composed of all the d-orbitals of the metallic ion and the electrons occupying them. The energies of these states are then computed using the NEVPT2 method to include the dynamical correlation. Spin orbit coupling between  $M_S$  components of all states are accounted for using Spin-Orbit-State-Interaction (SO-SI) method with NEVPT2 correlated energies as the diagonal elements of the SO matrix. Finally, the ZFS parameters are extracted using the Effective Hamiltonian Theory in a procedure implemented in the ORCA package. To go beyond the simple extraction of the parameters, a more thorough study requires the analysis of the wave-functions, energy differences and contributions to ZFS parameters.

### 3.1 First-Order Spin-Orbit Coupling

The search for large magnetic anisotropy in molecular systems remains a central objective in the design of next-generation single-molecule magnets (SMMs). In 3d transition-metal complexes, the challenge arises from the fact that usually SOC is weak compared to the ligand field, the orbital angular momentum is then almost quenched. SOC can be considered as a perturbation of spin-orbit free states (situation called second-order spin-orbit coupling) and magnetic anisotropy properties are correctly described by the zero-field splitting (ZFS) Hamiltonian, in which the axial  $D$  and rhombic  $E$  parameters quantify the splitting of the  $M_S$  components in the ground state. While this formalism has proved successful in identifying SMMs candidates, it fundamentally limits the achievable anisotropy, since second-order processes rely on large orbital energy gaps. One way to increase the anisotropy is to try and retrieve a contribution from first-order SOC, where near-degenerate orbitals allow the spin and orbital angular momenta to couple directly. This situation is well known for lanthanide ions, where unquenched orbital moments naturally give rise to extreme anisotropy, but it is rarely accessible for 3d ions, except in very low coordination numbers or highly symmetric geometries. The theoretical appeal of such systems is clear: when orbital quasi-degeneracy is preserved, the ZFS model breaks down, and anisotropy must instead be understood in terms of the mixing of spin-orbit states at the *ab initio* level. With this in mind, a series of five Iron(II) complexes were synthesized with the purpose of retrieving a first-order SOC. Through a joint study by experimentalists and theoricians, this work aims to determine the properties of the complexes and identify the contribution of first-order SOC. The use of a pentadentate ligand in the equatorial plane enforces a pentagonal bipyramidal geometry around the metallic center. Combined with a halides or  $\text{H}_2\text{O}$  ligands in the apical positions, this allows the conditions of quasidegeneracy of the  $d_{xz}$  and  $d_{yz}$  orbitals to be met.

The electronic structure of the complexe were computed using CAS(6,5)SCF calculations, which allow for the evaluation of the energy splitting of the d-orbitals. First-oder SOC involves the two lowest quintuplets  $Q_1$  and  $Q_2$ , which are essentially monoconfigurational with one electron occupying either the  $d_{xz}$  or  $d_{yz}$  orbital. The incorporation of the SOC was performed using the SO-SI method generating the full manifold of SO-states for the extraction of anisotropic

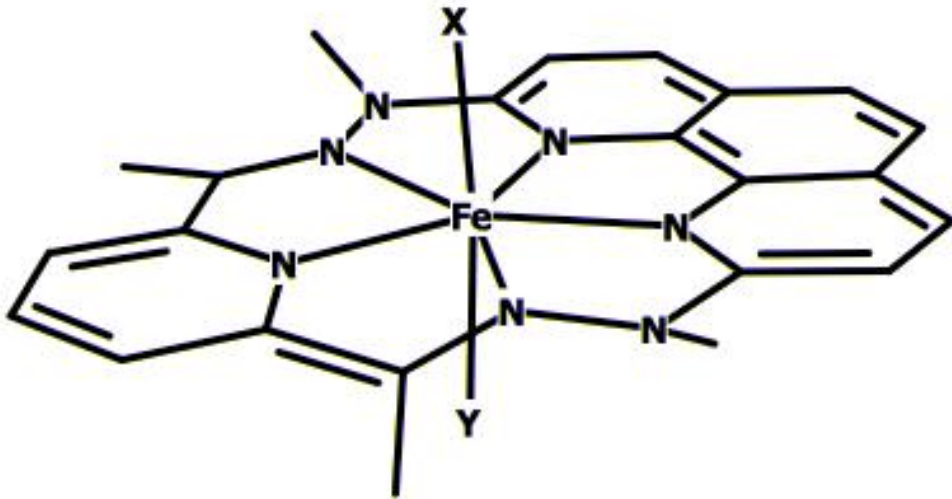


Figure 3.1: Schematic representation of the Fe(II) complex with H atoms attached to carbon hidden

parameter of the ZFS Hamiltonian. In parallel, a first-order SOC model was adopted, previously developed for low-symmetry iron and nickel complexes. In this picture, the ligand field Hamiltonian is represented in a basis of the nearly degenerate orbitals  $d_{xz}$  and  $d_{yz}$ . This lift of degeneracy is induced by distortion of the fully symmetric geometry and is described by two parameters:

- $\delta_1$  the splitting between the two orbitals, reflecting the extent to which degeneracy is broken.
- $\delta_2$  the off-diagonal mixing between the orbitals, which couples them in the ligand field Hamiltonian.

The ligand field Hamiltonian is then written:

$$\hat{H}_{LF} = \begin{pmatrix} -\delta_1 & \delta_2 \\ \delta_2 & \delta_1 \end{pmatrix}$$

An expression of the SO-states energy spectrum can be derived and directly compared to the *ab initio* one to obtain values for the  $\delta_i$  terms. It also provides a way to estimate the  $D$  and  $E$  parameter from the ZFS formalism if applicable.

The study indicates that the ZFS formalism is only applicable in the case of the  $H_2O$  ligand with a lift of orbital degeneracy of  $412\text{ cm}^{-1}$  between the  $d_{xz}$  and  $d_{yz}$ . The results indicates a significant axial anisotropy and rhombicity that is slightly underestimated compared to experimental determination with a  $S=2$

model. The two models, ZFS and first-order SOC, provide values that are in very good agreement.

In the case of other complexes, results indicates that they behave like SMMs with large anisotropy. However, the energy splitting between the  $d_{xz}$  and  $d_{yz}$  orbitals is very small, which leads to a strong mixing of the two lowest quintuplet states in the SO-ground state. Only a few  $\text{cm}^{-1}$  separate the five lowest SO-states from the other, rendering the ZFS hamiltonian inappropriate.

Overall, this study highlight that first-order SOC, traditionally associated with low-coordinate 3d complexes, can also be engineered in higher coordination environments by careful ligand design. This not only advances the understanding of magnetic anisotropy in transition metals, but also provides new opportunities for designing molecular materials with enhanced anisotropic interactions.

## RESEARCH ARTICLE

[View Article Online](#)  
[View Journal](#) | [View Issue](#)


Cite this: *Inorg. Chem. Front.*, 2025, **12**, 3456

## Engineering first-order spin–orbit coupling in a pentagonal bipyramidal Fe(II) complex and subsequent SMM behavior†

Kateryna Bretosh, <sup>a</sup> Virginie Béreau, <sup>a,b</sup> Flaurent Heully-Alary, <sup>c</sup> Nicolas Suaud, <sup>\*c</sup> Carine Duhayon, <sup>a</sup> Elen Duverger-Nédellec, <sup>d,e</sup> Nathalie Guihéry <sup>\*c</sup> and Jean-Pascal Sutter <sup>\*a</sup>

Pentagonal bipyramidal (PBP) complexes with a first-order spin–orbit coupling contribution can be readily obtained, mainly through chemical design optimization ensuring minimum structural distortion and a more symmetrical ligand field. This conclusion follows from the investigation of a series of five Fe(II) complexes:  $[FeL^{N5}(H_2O)Cl]Cl\cdot 4.5H_2O$ , **1**;  $[FeL^{N5}Cl_2]\cdot 3H_2O$ , **2**;  $[FeL^{N5}Br_2]$ , **3**;  $[FeL^{N5}I_2]$ , **4**; and  $[Fe_{0.12}Zn_{0.88}L^{N5}]_2$ , **5** ( $L^{N5}$  stands for the pentadentate macrocyclic ligand formed by the condensation of 2,6-diacetylpyridine and 2,9-di( $\alpha$ -methylhydrazino)-1,10-phenanthroline). Theoretical calculations revealed quasi-degeneracy of the  $d_{xz}$  and  $d_{yz}$  orbitals for the complexes with halide ligands at the apical positions ( $\Delta E = 91, 134$ , and  $142\text{ cm}^{-1}$ , respectively, for **2–4**). This small energy gap leads to SO states with very strong mixing of the ground and first excited quintet states. Therefore, the ZFS Hamiltonian is not suitable for modelling the magnetic properties of complexes **2–5**. This does not apply for **1** with  $\Delta E = 412\text{ cm}^{-1}$ . The recorded magnetic behaviors indicated strong magnetic anisotropy; for **1**  $D = -24\text{ cm}^{-1}$  was obtained. The Br and I derivatives were found to behave as SMMs (with a  $U/k_B$  of about 90 K), the latter even in the absence of a static field.

Received 18th December 2024,  
Accepted 1st March 2025

DOI: 10.1039/d4qi03255a  
[rsc.li/frontiers-inorganic](http://rsc.li/frontiers-inorganic)



### 10th anniversary statement

*Inorganic Chemistry Frontiers* is undoubtedly the benchmark journal for inorganic chemistry. From the beginning, it has been the policy of the journal that quality should prevail over quantity, and this policy has enabled it to quickly make a difference. I know that I am going to find in the journal the latest remarkable developments in my field. This is important to me, not only as a reader, but also as an author.

## Introduction

The paradigm of single-molecule and single-chain magnets (*i.e.* SMM and SCM)<sup>1,2</sup> has triggered efforts to achieve large magnetic anisotropy in molecular compounds.<sup>3–8</sup> One way of achieving this is to be close to the first-order spin–orbit regime. However, while the orbital angular momentum,  $L$ , plays a dominant role in lanthanide ions, it is generally quenched by the ligand field in transition metal ions.<sup>9,10</sup> In 3d ion complexes, the coordination sphere leads to an energy distribution of the d orbitals with differences of a few hundreds to a few thousands  $\text{cm}^{-1}$  between them. The magnetic anisotropy exhibited by the metal center stems from the interaction between the fundamental and excited levels resulting from the promotion of an electron to a higher-energy orbital, a process known as second-order spin–orbit coupling (SOC). This magnetic anisotropy is described by the zero-field splitting (ZFS) model,<sup>11</sup> and quantified by the axial parameter,  $D$ ,

<sup>a</sup>Laboratoire de Chimie de Coordination du CNRS (LCC-CNRS), Université de Toulouse, CNRS, 205 route de Narbonne, F-31077 Toulouse, France. E-mail: jean-pascal.sutter@lcc-toulouse.fr

<sup>b</sup>Université de Toulouse, Institut Universitaire de Technologie-Département de Chimie, Av. Georges Pompidou, F-81104 Castres, France

<sup>c</sup>Laboratoire de Chimie et Physique Quantiques (LCPQ), Université de Toulouse, CNRS, F-31062 Toulouse, France. E-mail: suaud@irsamc.ups-tlse.fr, nathalie.guihery@irsamc.ups-tlse.fr

<sup>d</sup>Department of Condensed Matter Physics, Faculty of Mathematics and Physics, Charles University, Ke Karlovu 5, 121 16 Praha 2, Czech Republic

<sup>e</sup>Univ. Bordeaux, CNRS, Bordeaux INP, ICMCB, UMR 5026, F-33600 Pessac, France

† Electronic supplementary information (ESI) available: Additional experimental information; crystal structure solution for **2**, crystallographic information, related plots, and bond lengths and angles for all the compounds, PXRD, Mössbauer spectra, EDX analysis of **5**, additional magnetic behaviors, and data from theoretical calculations. CCDC 2352840–2352845. For ESI and crystallographic data in CIF or other electronic format see DOI: <https://doi.org/10.1039/d4qi03255a>

and the rhombic term,  $E$ . The sign of  $D$ , which is positive for in-plane anisotropy and negative for axial anisotropy, is regulated by the coordination polyhedron and the electronic configuration of the metal center,<sup>12</sup> and its strength is inversely proportional to the energy difference of the ground and excited states. However, under certain conditions, the splitting of the orbital levels can lead to quasi-degenerate orbitals giving rise to a certain amount of first-order spin-orbit contribution. This results in much larger anisotropy and, in the case of an axial-symmetry ligand field, axial (*i.e.* Ising-type) anisotropy is observed. The use of low coordination number complexes is an effective approach to generate first-order SOC. This has been illustrated for Fe derivatives with two-coordinate linear<sup>13–16</sup> or trigonal-pyramidal<sup>17,18</sup> coordination spheres, most exhibiting slow relaxation of magnetization (*i.e.* SMM behavior). Similar results have been reported for Co(II)<sup>19,20</sup> and Ni(II)<sup>21–23</sup> derivatives. However, the slightest deformation of the coordination sphere or the symmetry of the ligand field leads to an increase in the energy difference between the d orbitals of the metal ion and lifts the quasi-degeneracy of the spin-orbit free states, resulting in the suppression of first-order SOC.<sup>15,24–26</sup>

While the contribution of the first-order SOC is clearly essential for enhancing the magnetic anisotropy in 3d ions, achieving this objective by chemical design remains highly challenging. And this becomes even more difficult if such complexes are to form the building blocks of polynuclear systems such as SCMs; a crucial requirement will be that the suitable geometry of the coordination polyhedron is structurally robust.

Energy diagrams with degenerate orbitals are also observed for geometries with higher coordination numbers.<sup>12</sup> This is the case for heptacoordinated species with pentagonal bipyramidal (PBP) arrangements for which two sets of two orbitals with the same energy levels are expected in the ideal geometry (Scheme 1). In real compounds, structural distortions and low symmetry of the ligand field lead to the lifting of degeneracies of the energy levels of these orbitals (from a few hundreds to thousands cm<sup>-1</sup>). However, a significant ZFS effect has been demonstrated for such complexes, with  $D$  parameters of the order of 30 cm<sup>-1</sup> for Co(II) to -30 cm<sup>-1</sup> for Fe(II) and Ni(II).<sup>27</sup> For a given metal ion, the value of  $D$  depends on the actual energy difference between these orbitals.<sup>28</sup> For instance, in Fe(II) derivatives, the main contribution to the negative  $D$  value

arises from the transfer of an electron between  $d_{xz}$  and  $d_{yz}$  orbitals; therefore their energy separation significantly affects the overall value of  $D$ . Theoretical calculations have revealed that  $D$  will not exceed -10 cm<sup>-1</sup> for an energy difference above 400 cm<sup>-1</sup>, but that  $D$  value may reach -20 to -30 cm<sup>-1</sup> when the energy difference is reduced to about 200 cm<sup>-1</sup>.<sup>29–32</sup> The same applies to Ni(II) in PBP coordination, but for the d<sup>8</sup> configuration it is the  $d_{xy}$  and  $d_{x^2-y^2}$  orbitals that are relevant.<sup>28</sup> Thus, to achieve large magnetic anisotropy, it is essential to minimize the energy gap between d orbitals. The optimum situation would be to achieve quasi-degeneracy, which would *de facto* induce a substantial contribution from first-order SOC.

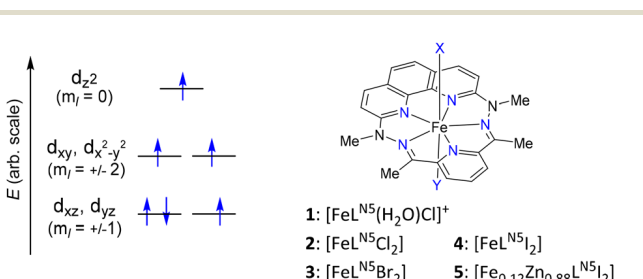
We show here that PBP complexes with a first-order SOC contribution can be readily obtained, mainly through chemical design optimization ensuring minimum structural distortion and a more symmetrical ligand field.

The PBP coordination polyhedron is typically induced by a pentadentate ligand, which occupies the equatorial positions of the complex and confers remarkable structural robustness. The phenanthroline-based macrocyclic ligand L<sup>N5</sup> (Scheme 1) gained our preference because it is planar, obviously stiff, and symmetrical with five coordinating sp<sup>2</sup>-N atoms. A suitable metal ion is Fe(II). Its high-spin d<sup>6</sup> electronic configuration in the PBP geometry leads to three electrons occupying the two  $d_{xz}$  and  $d_{yz}$  orbitals. As these orbitals are ideally degenerate and are linear combinations of  $m_l = \pm 1$  spherical harmonics, 1<sup>st</sup> order SOC can take place. However, to maintain the (quasi-)degeneracy of these orbitals, the apical ligands of the complex must have the same interaction with each of these orbitals, and any dissymmetry would induce an energy difference between them.<sup>29</sup> Halides (Cl<sup>-</sup>, Br<sup>-</sup>, and I<sup>-</sup>) seemed best suited for this purpose. The corresponding complexes are reported here. Theoretical calculations revealed quasi-degeneracy of the  $d_{xz}$  and  $d_{yz}$  orbitals ( $\Delta E < 200$  cm<sup>-1</sup>) for all those with halide ligands in the apical positions. Their magnetic behavior indicated strong magnetic anisotropy, and the bromide and iodide derivatives were found to behave as SMMs, the latter even in the absence of a static field.

## Results and discussion

### Syntheses

The PBP complexes [FeL<sup>N5</sup>(H<sub>2</sub>O)Cl]Cl·4.5H<sub>2</sub>O, 1; [FeL<sup>N5</sup>Cl<sub>2</sub>]·3H<sub>2</sub>O, 2; [FeL<sup>N5</sup>Br<sub>2</sub>], 3; [FeL<sup>N5</sup>I<sub>2</sub>], 4; and [Fe<sub>0.12</sub>Zn<sub>0.88</sub>L<sup>N5</sup>I<sub>2</sub>], 5, were obtained by adapting a reported procedure.<sup>33</sup> The Fe(II) complex [FeL<sup>N5</sup>(H<sub>2</sub>O)Cl]Cl·4.5H<sub>2</sub>O, 1, was prepared by reacting FeCl<sub>2</sub>·4H<sub>2</sub>O, 2,6-di(acetyl)pyridine, and 2,9-di( $\alpha$ -methylhydrazino)-1,10-phenanthroline in H<sub>2</sub>O in the presence of HCl. When excess NaCl was added to the reaction mixture, co-crystallization of 1 and [FeL<sup>N5</sup>Cl<sub>2</sub>]·5H<sub>2</sub>O, 2 occurred. However, the complexes [FeL<sup>N5</sup>Br<sub>2</sub>], 3 and [FeL<sup>N5</sup>I<sub>2</sub>], 4 were isolated as single products by the same procedure (*i.e.* in the presence of an excess amount of either NaBr or NaI, and the corresponding HX acid). The reactions were performed under strictly oxygen-free conditions, although the addition of



**Scheme 1** Relative energy diagram of the d orbitals in an ideal pentagonal bipyramidal geometry ( $D_{5h}$ ), the electron filling is for high-spin Fe(II), and sketch of the molecular complexes 1–5.



ascorbic acid was required to avoid traces of oxidation. This was systematically confirmed by Mössbauer spectroscopy (see below). All the complexes were isolated as crystallized solids and the same batch was used for the characterization studies.

In order to investigate these Fe complexes diluted in a diamagnetic matrix, the corresponding Zn(II) complexes were synthesized to verify structural concordance. Only the iodide derivative  $[ZnL^{N5}I_2]$  proved isostructural to the Fe homologue. With  $Br^-$ , a pentagonal pyramidal complex,  $[ZnL^{N5}Br]Br \cdot 0.5H_2O$ , with a single axial ligand was obtained (Fig. S6†), and the Cl derivative could not be crystallized. Thus, only mixed-metal derivative  $[Fe_{0.12}Zn_{0.88}L^{N5}I_2]$ , 5, was prepared. Information on these Zn complexes are provided in the ESI.†

### Crystal structures

The crystal structures for all the complexes have been determined by single-crystal X-ray diffraction analyses; the crystallographic data are given in Table S1 (ESI).† The metal–ligand bond lengths and axial bond angles for the first coordination sphere of 1–4 are gathered in Table 1, and additional information can be found in the ESI (Fig. S1–S6†).

Complexes 1–4 and  $[ZnL^{N5}I_2]$  are mononuclear and have a chemical organization similar to known PBP complexes of 3d metal ions with ligand  $L^{N5}$ .<sup>33–38</sup> The crystal arrangement of 2 was found to be incommensurable and composed of two superimposed inverted configurations, more information can be found in the ESI.† For each molecular complex, the M(II) center is heptacoordinated and sits in a slightly distorted pentagonal bipyramidal environment (Fig. 1 and ESI†). The equatorial plane is formed by five N atoms from pentadentate ligand  $L^{N5}$ , while axial positions are occupied by different donor groups:  $H_2O$  and  $Cl^-$  for 1,  $Cl^-$  for 2,  $Br^-$  for 3, and  $I^-$  for 4 and  $[ZnL^{N5}I_2]$ . The Fe–N bond distances in the equatorial sites are found between 2.07 and 2.28 Å, the shortest is with the N of the pyridyl moiety and the longer with the imine groups (Table 1). These bond distances are very similar to those reported for  $[FeL^{N5}(H_2O)_2]^{2+}$ .<sup>33</sup> The bonds between the metal center and the halogen atoms in the apical sites are longer, extending from 2.25 to 2.92 Å for  $Cl^-$  to  $I^-$ , in line with the increasing van der Waals radii of these atoms. The equatorial coordination arrangement is perfectly planar, the five nitrogen atoms and the iron atom (as well as Zn in  $[ZnL^{N5}I_2]$ ) lie in the same plane (defined by the 5 N, see Fig. S1–S5†), and only for 1 the Fe atom is very marginally outside the plane by 0.022 Å.

The apical arrangement very slightly deviates from normal to the equatorial plane, and the X–Fe–X links form an angle of around 170° (Table 1) in all the complexes. Thus, the coordination polyhedron of all these complexes is best described by a pentagonal bipyramidal geometry.

To evaluate the degree of deviation from the ideal PBP geometry, continuous shape measures analysis of the coordination polyhedron was performed with SHAPE software.<sup>39,40</sup> The CShM parameter values related to the deviation of the actual shape from ideal PBP for 1–4 are 0.499, 1.060, 1.326, and 2.214, respectively. The divergence, which increases from 1 to 4, can be ascribed to the increasing size of the halogen atoms. Indeed, the distortion of the equatorial plane from the pentagonal geometry is quite small and similar for all complexes (Table S2†). The increasing deviation from the ideal PBP geometry is therefore mainly due to the lengthening of the Fe–X<sub>axial</sub> bonds from 1 to 4 (Table 1) due to the larger size of the halogen atoms which results in an elongated pentagonal bipyramidal environment.

For  $[ZnL^{N5}Br]Br$ , the molecular complex exhibits a pentagonal pyramidal coordination sphere with the five N atoms of  $L^{N5}$  bonded to Zn forming the pentagonal base and a coordinated Br located on the apex of the pyramid (Fig. S6†). Zn(II) is located approximately 0.441 Å above the basal plane with N–Zn bond distances ranging from 2.134 Å to 2.350 Å (Fig. S6†), which are slightly longer than those in  $[ZnL^{N5}I_2]$ . The charge of this cationic complex is compensated by a bromide anion. Although unusual, the formation of a pentagonal pyramidal complex between  $L^{N5}$  and a 3d metal ion is not unprecedented, and it was reported for an Mn(II) derivative with Cl as the apical ligand.<sup>41</sup>

For all the compounds the crystal packing shows that the complexes are stacked in parallel (Fig. S1–S4†). For 1 and 2 the complexes are organized in layers, with uncoordinated Cl and/or  $H_2O$  solvates in between (Fig. S1 and S2†), whereas the packing is more compact for the solvent-free 3 and 4. The closest distances between the Fe centers are similar, with values of 8.352(1) to 8.7229(3) Å from 1 to 4. For the Br- and I-derivatives, some rather close separations between the halogen atoms and the hydrogen of adjacent complexes, especially with phenanthroline and pyridyl moieties, become evident when the van der Waals radii of the halogens are considered (about 1.85 and 2.0 Å, respectively). These weak hydrogen bonds (H…X: 2.8062(4)–2.9585(4) Å in 3 and 3.0592(2)–

**Table 1** Metal–ligand bond lengths (Å) and axial bond angles (°) for the first coordination sphere for 1–4

1	2		3		4	
Fe1–N1 2.1112(2)	Fe1–N3 2.13(1)	Fe2–N6 2.07(1)	Fe1–N1 2.128(5)	Fe1–N1 (2.1053)		
Fe1–N2 2.273(2)	Fe1–N4 2.248(7)	Fe2–N5 2.252(9)	Fe1–N2 2.304(3)	Fe1–N2 2.280(2)		
Fe1–N7 2.270(2)	Fe1–N7 2.117(9)	Fe2–N2 2.124(9)	Fe1–N4 2.114(3)	Fe1–N4 2.123(2)		
Fe1–N4 2.137(2)	Fe1–Cl1 2.575(6)	Fe2–Cl1 2.544(2)	Fe1–Br1 2.7106(5)	Fe1–I1 2.9231(2)		
Fe1–N5 2.134(2)	Fe1–Cl2 2.555(6)	Fe2–Cl2 2.591(6)	Br–Fe–Br 171.08(4)	I–Fe–I 170.556(4)		
Fe1–Cl 2.2549(7)	Cl–Fe1–Cl 171.5(1)	Cl–Fe2–Cl 170.0(1)				
Fe1–O1 2.193(2)						
Cl–Fe–O 174.26(5)						



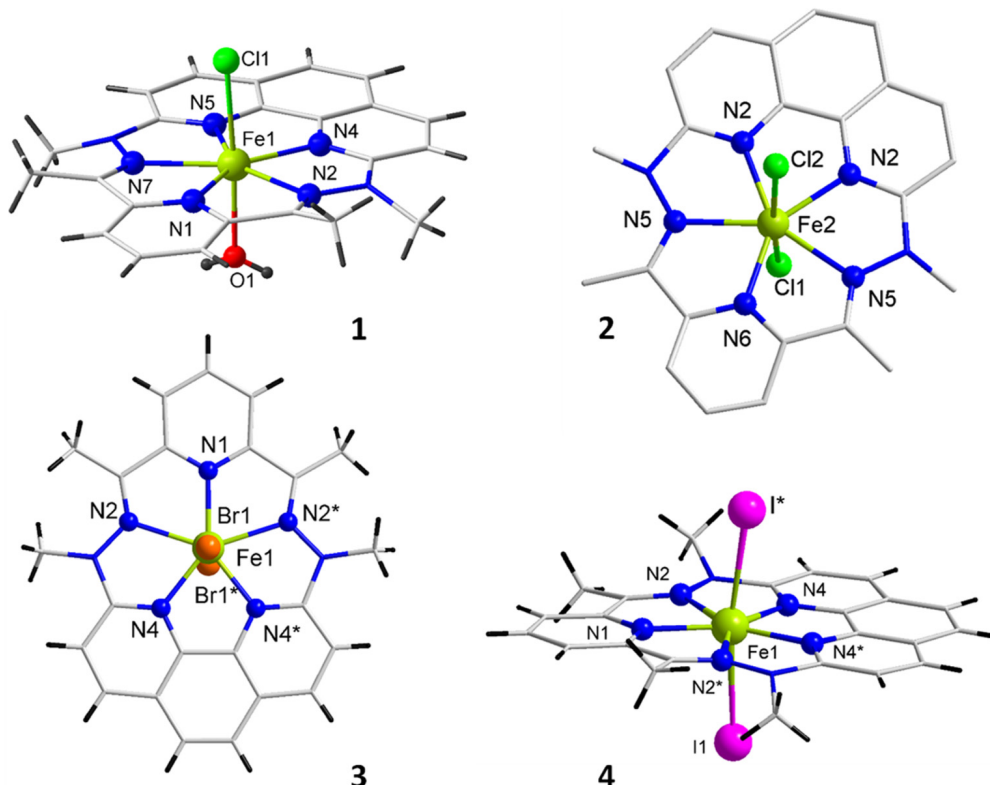


**Fig. 1** Molecular structures of the Fe complexes **1–4**. One of the two independent complexes of **2** is shown; counter ion and lattice solvent molecules are not depicted; \* refers to the  $1 - x, y, 1,5 - z$  symmetry operation.

3.1730(2) in **4**) are likely to inter-connect all the molecules in the solid (Fig. S4†) and propagate magnetic interactions (*vide infra*).

With the exception of compound **2**, the phase concordance of the bulk samples with the crystal structures was confirmed by powder X-ray diffraction (Fig. S7†).

### Mössbauer spectroscopy

$^{57}\text{Fe}$  Mössbauer spectroscopy was carried out to confirm the oxidation state of the Fe centers and the purity of samples **1**, **3**, and **4** for magnetic studies. The spectra recorded at 80 K show a unique doublet (Fig. S8†) with a chemical shift near  $\delta = 1.1 \text{ mm s}^{-1}$  and a quadrupole splitting of about  $\Delta = 2.1 \text{ mm s}^{-1}$  (Table 2). These characteristics are comparable to those reported (*i.e.* 1.1 and 2.74  $\text{mm s}^{-1}$ , respectively) for a homologous high-spin Fe(II) complex with  $\text{H}_2\text{O}$  as ligands in the apical positions.<sup>33</sup> Moreover, Mössbauer data have been reported for several other Fe(II) complexes in the PBP surrounding featuring either a macrocyclic ligand<sup>42–44</sup> or an open pentadentate ligand<sup>29,45–49</sup> in their equatorial coordination sphere. In all cases the chemical shift is found between 1.0 and 1.2  $\text{mm s}^{-1}$  while their quadrupole splitting is more versatile as it varies with the ligands located in the apical positions.<sup>29</sup> Interestingly, Fe(III) in the same PBP environment exhibits a decrease in the chemical shift to about  $\delta = 0.5 \text{ mm s}^{-1}$  with smaller splitting,<sup>50,51</sup> which makes it very distinguishable and easy to

**Table 2** Experimental Mössbauer parameters and magnetic characteristics for **1, 3–5**

	<b>1</b>	<b>3</b>	<b>4</b>	<b>5</b>
<i>Mössbauer doublet (80 K)</i>				
$\delta$ ( $\text{mm s}^{-1}$ )	1.10	1.09	1.05	—
$\Delta$ ( $\text{mm s}^{-1}$ )	2.12	2.14	2.03	—
<i>Magnetic characteristics</i>				
$\chi_M T$ at 300/2 K ( $\text{cm}^3 \text{ mol}^{-1} \text{ K}$ )	3.16/2.21	3.90/2.11	3.27/0.58	—
$M$ ( $\mu_{\text{B}}$ ) for 50 kOe at 2 K	2.52	2.73	2.14	2.28
$U/k_{\text{B}}$ (K)	—	$89 \pm 5$	$99 \pm 8$	$88 \pm 9$
$\tau_0$ (s)	—	$7 \times 10^{-12}$	$3 \times 10^{-11}$	$2 \times 10^{-10}$

identify in the Mössbauer spectrum of a Fe(II) derivative. The spectra obtained for **1**, **3** and **4** are typical of high spin PBP Fe(II) complexes with no detectable traces of oxidation products.

### Theoretical calculations

Wavefunction based calculations (SO-CAS(6/5)SCF + NEVPT2) (see the Experimental section for computational information) have been performed on complexes **1** to **4** followed by the procedure of anisotropic parameter extraction proposed by Maurice *et al.*<sup>52</sup> The atom coordinates from the X-ray structures were considered except for the positions of the H atoms that were optimized using DFT calculations.

**Table 3** (left part) Energy differences ( $\text{cm}^{-1}$ ) between the ground state  $Q_1$  spin-orbit free and the 4 excited quintuplet states ( $Q_2$  is the 1st excited one, ...) in complexes **1–4** (the apical ligands is indicated in brackets), obtained at the NEVPT2 level of calculations, and (right part) AILFT 3d MO energies obtained at the NEVPT2 level of calculations

Complex	$Q_2$	$Q_3$	$Q_4$	$Q_5$	$d_{yz}$	$d_{xz}$	$d_{x^2-y^2}$	$d_{xy}$	$d_{z^2}$
<b>1</b> (Cl H <sub>2</sub> O)	450	6661	7951	9228	0	412	5275	6278	7197
<b>2</b> (Cl)	92	6804	7756	9060	0	91	5323	6122	7048
<b>3</b> (Br)	42	5734	7999	8070	134	0	4597	6415	6470
<b>4</b> (I)	37	6314	7962	8739	142	0	5020	6570	7035

The  $x$ ,  $y$ , and  $z$  axes are those presented in Fig. S15.<sup>†</sup>

The NEVPT2 energy differences between the spin-orbit free quintuplet ground state and the first excited quintuplet state resulting from d-d transitions are given in Table 3, together with the energies of the AILFT 3d MOs. It should be specified that the lowest  $Q_1$  and  $Q_2$  states essentially have a mono-configurational wavefunction with a double occupancy either in the  $d_{xz}$  or the  $d_{yz}$  orbital (depending on the complex).

Atanasov *et al.*<sup>26</sup> have studied a family of trigonal pyramidal iron(II) complexes that exhibit very similar spectra to those calculated here with almost degenerate  $d_{xz}$  and  $d_{yz}$  orbitals. They proposed a model that accounts for the first-order SOC and the lift of degeneracy arising from geometrical distortions from the ideal  $C_3$  symmetry. A related approach has also been developed to characterize a Ni(II) complex.<sup>21</sup> This model is applicable to the complexes studied here, for which the ideal symmetry would contain a  $C_5$  symmetry axis. In the case of strictly degenerate  $d_{xz}$  and  $d_{yz}$  orbitals, the ground state is degenerate and consists of a 1:1 mixture of two quintuplet states ( $Q_1$  and  $Q_2$ ) in which either the  $d_{xz}$  or the  $d_{yz}$  orbital contains a single electron. Distortions of the ideal  $C_5$  symmetry will lead to a lift of the degeneracy ( $2\delta_1$ ) of these orbitals and to their mixing ( $\delta_2$ ) so that the ligand field Hamiltonian matrix can be written as:

$$\begin{pmatrix} d_{xz} & d_{yz} \\ -\delta_1 & \delta_2 \\ \delta_2 & \delta_1 \end{pmatrix}. \quad (1)$$

In the complexes studied here, the states  $Q_1$  and  $Q_2$  are almost mono-configurational, hence the  $\delta_2$  parameter is close to zero. As the  $d_{xz}$  and  $d_{yz}$  orbitals are linear combinations of the  $M_l = \pm 1$  spherical harmonics, the two spin-orbit free quintuplet states  $Q_1$  and  $Q_2$  can only be coupled through the  $\zeta l_z s_z$  part of the spin-orbit Hamiltonian:

$$\hat{H}^{\text{SOC}} = \zeta \sum_i (l_i^z s_i^z + (l_i^+ s_i^- + l_i^- s_i^+)/2) \quad (2)$$

where  $\zeta$  is the covalently reduced effective spin-orbit constant.<sup>53</sup>

SOCs will generate 10 spin-orbit states, which are the eigenfunctions of the spin-orbit and ligand field Hamiltonian, the representative matrix of which is provided in the ESI (Table S6<sup>†</sup>). In the absence of SOC with the other excited

states, the analytical expressions of the energy of the SO states resulting from this first-order SOC would be:

$$\begin{aligned} E(\text{SO}_1, \text{SO}_2/\text{SO}_9, \text{SO}_{10}) &= \pm \frac{1}{2} \sqrt{4\delta^2 + \zeta^2} \\ E(\text{SO}_3, \text{SO}_4/\text{SO}_7, \text{SO}_8) &= \pm \frac{1}{4} \sqrt{16\delta^2 + \zeta^2} \\ E(\text{SO}_5/\text{SO}_6) &= \pm \delta \end{aligned} \quad (3)$$

where  $\delta = \sqrt{\delta_1^2 + \delta_2^2}$ .

The *ab initio* energy of these SO states is given in Table 4 as well as their wavefunction decomposition on the basis of the two spin-orbit free quintuplet states  $Q_1$  and  $Q_2$ . Of course, the SOC with other excited states is non-zero and is treated *ab initio*, indicating that the reported energies do not strictly follow these spacings.

In complex **1**, the ground state is mainly based on a configuration with a doubly occupied  $d_{yz}$  MO (and a single occupation of all other MOs), while  $Q_2$ ,  $Q_3$ ,  $Q_4$ , and  $Q_5$  exhibit double occupancy of the  $d_{xz}$ ,  $d_{x^2-y^2}$ ,  $d_{xy}$  and  $d_{z^2}$  MOs, respectively. The spectrum presents an energy gap of  $450 \text{ cm}^{-1}$  between the ground and first excited states originating from the energy gap between the  $d_{yz}$  and  $d_{xz}$  MOs. Therefore, the 5 lowest SO states  $\text{SO}_1-\text{SO}_5$  are mainly based on the  $M_s$  components of  $Q_1$  (more than 86%) and are low in energy compared to  $\text{SO}_6-\text{SO}_{10}$  that are mainly based on  $Q_2$  components. In this case, the anisotropic ZFS spin Hamiltonian applies (eqn (4)); it is extended with a fourth-order tensor operator represented by  $B_{40}$ , as recommended.<sup>26</sup>

$$\begin{aligned} \hat{H}_{\text{ZFS}} = D[\hat{S}_z^2 - S(S+1)/3] + \frac{E[\hat{S}_+^2 + \hat{S}_-^2]}{2} \\ + B_{40}[35\hat{S}_z^4 - (30S(S+1) - 25)\hat{S}_z^2 + 3S(S+1)(S(S+1)-2)] \end{aligned} \quad (4)$$

Parameters  $B_{40}$ ,  $D$  and  $E$ , reported in Table 5, have been extracted for complex **1** using the following formulas which result from the diagonalization of the Hamiltonian  $\hat{H}_{\text{ZFS}}$  matrix (given in Table S7<sup>†</sup>):

$$\begin{aligned} D &= -\frac{1}{7}[(\text{En}_{\pm 2} - \text{En}_{\pm 1}) + (\text{En}_{\pm 2} - \text{En}_0)] \\ B_{40} &= \frac{1}{140} \left[ (\text{En}_{\pm 2} - \text{En}_0) - \frac{4}{3}(\text{En}_{\pm 2} - \text{En}_{\pm 1}) \right]. \end{aligned} \quad (5)$$

In eqn (5),  $\text{En}_{\pm 2}$ ,  $\text{En}_{\pm 1}$  and  $\text{En}_0$  are the mean energy values of the SO states essentially carried by the  $M_s = \pm 2$ ,  $M_s = \pm 1$ , and



**Table 4** Energy ( $\text{cm}^{-1}$ ) and decomposition of the ground and first excited spin–orbit states on the basis of  $\text{Q}_1$  and  $\text{Q}_2$ 

Complex		$\text{SO}_1$	$\text{SO}_2$	$\text{SO}_3$	$\text{SO}_4$	$\text{SO}_5$	$\text{SO}_6$	$\text{SO}_7$	$\text{SO}_8$	$\text{SO}_9$	$\text{SO}_{10}$
<b>1</b>	Energies	0.0	1.0	34	48	58	507	521	548	601	603
	Weights	86/12	87/12	96/3	95/5	98/0	0/96	3/95	5/94	12/87	12/85
<b>2</b>	Energies	0.0	0.0	81	82	141	228	280	320	408	410
	Weights	61/39	61/39	71/28	69/31	99/0	0/99	28/71	31/69	39/60	39/60
<b>3</b>	Energies	0.0	0.0	84	86	161	207	275	315	411	411
	Weights	55/44	55/44	62/38	59/40	99/0	0/99	37/62	41/59	44/55	44/55
<b>4</b>	Energies	0.0	0.0	87	88	169	208	284	320	421	421
	Weights	54/45	54/45	60/40	58/42	99/0	0/99	40/60	42/58	45/54	45/54

Weights (in %) are given for  $\text{Q}_1/\text{Q}_2$ . SO states  $\text{SO}_1$ ,  $\text{SO}_2$ ,  $\text{SO}_9$  and  $\text{SO}_{10}$  are based on the  $M_s = \pm 2$  of  $\text{Q}_1$  and  $\text{Q}_2$  respectively,  $\text{SO}_3$ ,  $\text{SO}_4$ ,  $\text{SO}_7$  and  $\text{SO}_8$  on the  $M_s = \pm 1$  components, and  $\text{SO}_5$  and  $\text{SO}_6$  on the  $M_s = 0$  components.

**Table 5** Parameters extracted from the formulas (see text) and provided by the ORCA code<sup>59</sup>

Complex	$D$ (eqn (5))	$D$ (ORCA)	$D$ (exp)	$E$ (eqn (5))	$E$ (ORCA)	$E$ (Exp)	$B_{40}$	$\delta$	$\zeta$ (ORCA)
<b>1</b>	-14.00	-13.64	$-24.9 \pm 0.4$	2.33	2.24	$4.06 \pm 0.04$	0.09	225	411
<b>2</b>	—	—	—	—	—	—	—	43	409
<b>3</b>	—	—	—	—	—	—	—	23	404
<b>4</b>	—	—	—	—	—	—	—	20	396

Axes are those of the  $\mathbf{D}$  tensor for complex **1** (Fig. S15†).  $z$  is almost aligned with the bond between the metal and the apical ligands and  $x$  and  $y$  are in the plane of the pentadentate ligand.  $x$  is almost along the Fe–N(pyridine) direction in **1** (N1).

$M_s = 0$  spin components, respectively.  $E$  is 1/6 of the splitting between the two SO states essentially carried by the  $M_s = \pm 1$  spin components. The values of the ZFS parameters  $D$  and  $E$ , and of the spin–orbit constant calculated in ORCA are also reported (Table 5). The decrease of the spin–orbit constant in complexes (in comparison with the free metal ion) is due to the covalent interaction between the metal ion and the ligand and is called the relativistic nephelauxetic effect. As expected, the obtained values follow the spectrochemical series, and therefore, they decrease as the nephelauxetic effect increases, *i.e.*  $\text{H}_2\text{O} \ll \text{Cl}^- < \text{Br}^- < \text{I}^-$ . This effect is well documented in the literature.<sup>54–58</sup> As expected from the nature of the excitation from  $\text{Q}_1$  to  $\text{Q}_2$ – $\text{Q}_5$ , the contribution of  $\text{Q}_2$  to  $D$  is negative ( $-18.9 \text{ cm}^{-1}$ ) while those of  $\text{Q}_3$  and  $\text{Q}_4$  are positive and of much smaller amplitude ( $+1.97$  and  $0.72 \text{ cm}^{-1}$ , respectively) since these states are much higher in energy, and the contribution of  $\text{Q}_5$  is almost zero.

The case of complexes **2**, **3** and **4** is more complex since the energy gap between  $\text{Q}_1$  and  $\text{Q}_2$  is much smaller than in **1**, as  $d_{yz}$  and  $d_{xz}$  are almost degenerate. This small energy gap leads to SO states with a very strong mixing of  $\text{Q}_1$  and  $\text{Q}_2$  spin–orbit free states (except for  $M_s = 0$  components that do not interact through SOC) and no clear gap is observed between the 5 lowest and 5 highest energy states. Therefore, the ZFS Hamiltonian is not suited to model magnetic properties of complexes **2**–**4**,<sup>60</sup> and only their  $\delta$  and  $\zeta$  parameters have been reported in Table 5. Note that parameters  $D$  and  $E$  are provided by the ORCA code and can be calculated using the formulas given above, but the magnetic moment, which now contains a non-negligible contribution from the angular momentum, can no longer be equated with spin momentum alone. For this

reason, an evaluation of the  $D$  and  $E$  parameters from the magnetic data using spin  $S = 2$  is irrelevant for these complexes.

The calculated  $g$ -factors show the anticipated trend with  $g_x \approx g_y \ll g_z$ , values are tabulated in Table S8.† In addition, the magnetization *versus* field has been calculated at various temperatures and will be compared below to the measured magnetizations.

Compared with previous works on PBP Fe(II) complexes,<sup>29,48</sup> the first order SOC contribution in complexes **2** to **4** is much more important. Indeed, it should be noted that the energy differences between the ground state  $\text{Q}_1$  spin–orbit free quintuplet and the first excited state ( $\text{Q}_2$ ) are particularly small here. For instance, in the earlier reports these values vary between 170 and 410  $\text{cm}^{-1}$ , compared to the 37–92  $\text{cm}^{-1}$  found for **2**–**4** (Table 3). Complex **1**, with  $\text{H}_2\text{O}$  in the apical position, has an energy difference of 450  $\text{cm}^{-1}$  between  $\text{Q}_1$  and  $\text{Q}_2$ , and can therefore be described using a ZFS model. In **1**, this energy difference is governed by the energy difference between the  $d_{yz}$  and  $d_{xz}$  orbitals, which in turn is governed by the difference of interactions in the  $x$  and  $y$  axes. In this respect, the orientation of the  $\pi$ -doublets in the apical positions plays a crucial role in these complexes.<sup>48</sup> In **1**, the  $\pi$  doublet of  $\text{H}_2\text{O}$  is oriented along the  $x$  axis (Fig. S15†) and therefore introduces a dissymmetry between  $x$  and  $y$  axes, which is responsible for the lift of degeneracy between the two orbitals. On the other hand, for halogen atoms as in **2**–**4**, 2  $\pi$  doublets are involved with identical interactions with  $d_{yz}$  and  $d_{xz}$ , leading to quasi-degeneracy of the orbitals.

### Magnetic properties

The temperature dependence of the molar magnetic susceptibility,  $\chi_M$ , in the 2 to 300 K range, and the field dependence of



the magnetization at different temperatures between 2 and 8 K were recorded for complexes **1**, **3**, and **4** (Fig. 2 and S10†).

All the derivatives exhibit a paramagnetic behavior characterized by a constant  $\chi_M T$  value between 300 and 100 K, followed by an increasingly steep decline as  $T$  approaches 2 K. The characteristic values found at 300 and 2 K are listed in Table 2. As can be seen in Fig. 2, the decline is clearly more pronounced for **4**. For this compound the  $M$  versus  $H$  at 2 K also exhibits an S-shape behavior (Fig. 2b). These behaviors indicate antiferromagnetic interactions between the complexes in the solid state.<sup>61</sup> This was anticipated from the crystal lattice arrangement of **4**, which shows short contacts existing between the Fe complexes by means of I atoms and phenanthroline moieties (*vide supra*). The  $M$  versus  $H$  behavior for **5** confirms this hypothesis (Fig. 2b), as such intermolecular magnetic interactions no longer occur for the diluted derivative.

The field dependences of the magnetizations for **1**, **3**, and **4** between 2 and 8 K are depicted in Fig. S10.† For all complexes,

the magnetization achieved for a field of 50 kOe at 2 K is around  $2.5\mu_B$  (Table 2), a value lower than the expected contribution of spin alone for a center with  $S = 2$ , confirming the existence of substantial magnetic anisotropy. The theoretical calculations revealed that only derivative **1** shows no mixing between ground and excited states, and so its magnetic behaviors were likely to be analyzed with a ZFS-based model. Indeed, a good adjustment of the experimental  $M$  versus  $H$  behaviors was obtained with a model for an  $S = 2$  with magnetic anisotropy accounted by ZFS, yielding  $D = -24.9 \pm 0.4 \text{ cm}^{-1}$  and  $E = 4.06 \pm 0.04 \text{ cm}^{-1}$  for  $g = 2.34$  (Fig. S10a†). The negative value for  $D$  is in agreement with the anticipated axial magnetic anisotropy for a high-spin  $d^6$  ion in PBP geometry,<sup>27</sup> and with the calculated value. A similar analysis proved impossible for **3** (let alone **4**), which is in line with the conclusion of the theoretical studies. However, for these complexes the experimental  $M$  versus  $H$  behaviors are well reproduced by the calculated behaviors as described above (Fig. S10†).

The existence of a slow magnetization relaxation phenomenon was examined by AC-mode magnetic susceptibility measurements in zero field and in the presence of an applied magnetic field. For **1**, just the onset of an out-of-phase component of the susceptibility,  $\chi_M''$ , is observed in the applied field (Fig. S11†), a behavior indicative of fast relaxation above 2 K. For **3**, a slow relaxation is revealed when a small field is applied to cancel the QTM (quantum tunneling of the magnetization), while the  $\chi_M''$  versus  $T$  for **4** in zero field shows a frequency dependent peak (Fig. S12a and S13a,† respectively).

For **3**, the optimum applied DC field, *i.e.* for which the peak signal of  $\chi_M''$  is the largest and at the lowest frequency, turned out to be 5 kOe (Fig. S12b†). Detailed AC studies were carried out with this applied field to reveal frequency and temperature dependencies of the  $\chi_M''$  characteristic for an SMM (Fig. 3 and S12†). The relaxation times,  $\tau$ , between 2 and 5.6 K were obtained from the analyses of  $\chi_M''$  versus  $\nu$  behaviors using a generalized Debye model.<sup>62</sup> The temperature dependency of  $\tau$  is well modeled by an expression combining an Orbach process (Arrhenius law) and a direct mechanism to account for the lower temperature behavior (eqn (6), respectively first and second term).<sup>1,5</sup> The best fit gave  $U/k_B = 89 \pm 5 \text{ K}$ ,  $\tau_0 = 7 \times 10^{-12} \text{ s}$ ,  $DH^n = 14.6 \pm 1.0 \text{ K}^{-1} \text{ s}^{-1}$ .

$$\tau^{-1} = \tau_0^{-1} \exp(-U/k_B T) + DH^2 T + \text{QTM}^{-1} \quad (6)$$

For **4**, the temperature dependency of  $\chi_M''$  in the absence of a static applied magnetic field exhibits a well-defined peak shape with the maximum shifts from about 6 K to lower  $T$  with decreasing AC frequencies from 1500 to 1 Hz (Fig. S13b†). However,  $\chi_M''$  does not tend to return to zero after reaching the peak when the temperature is lowered. The behavior at lower temperatures (<3 K) is characteristic of QTM, but a second, smaller peak is also observed at around 3.5 K. This second component could be the signature of magnetic ordering, which is also suggested by the meta-magnetic behavior shown by **4** (Fig. 2b). Indeed, the second ( $T$ -independent) signal is no longer found for **5** (*vide infra*). Moreover, the signal at 3.5 K is

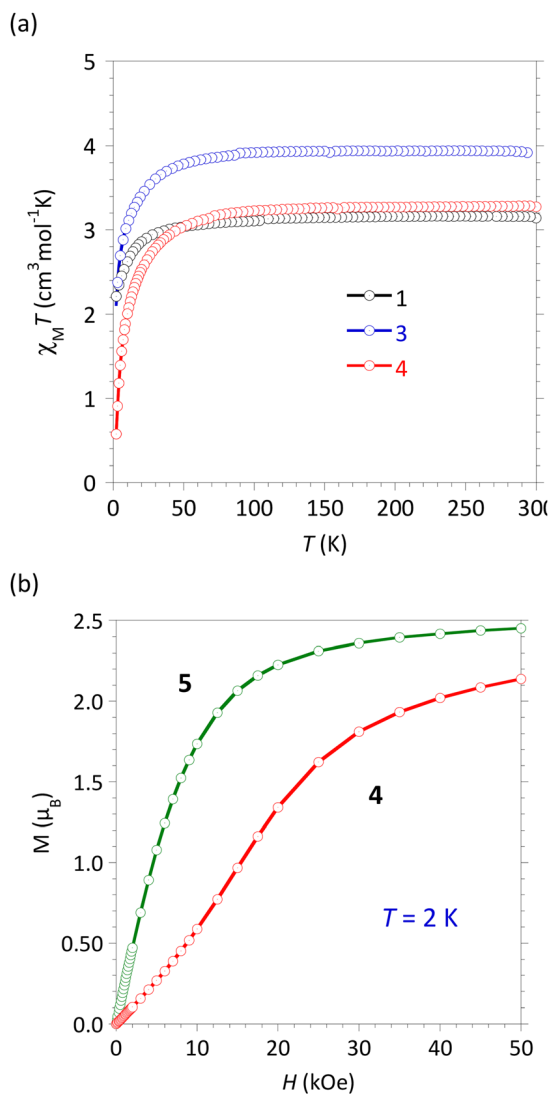
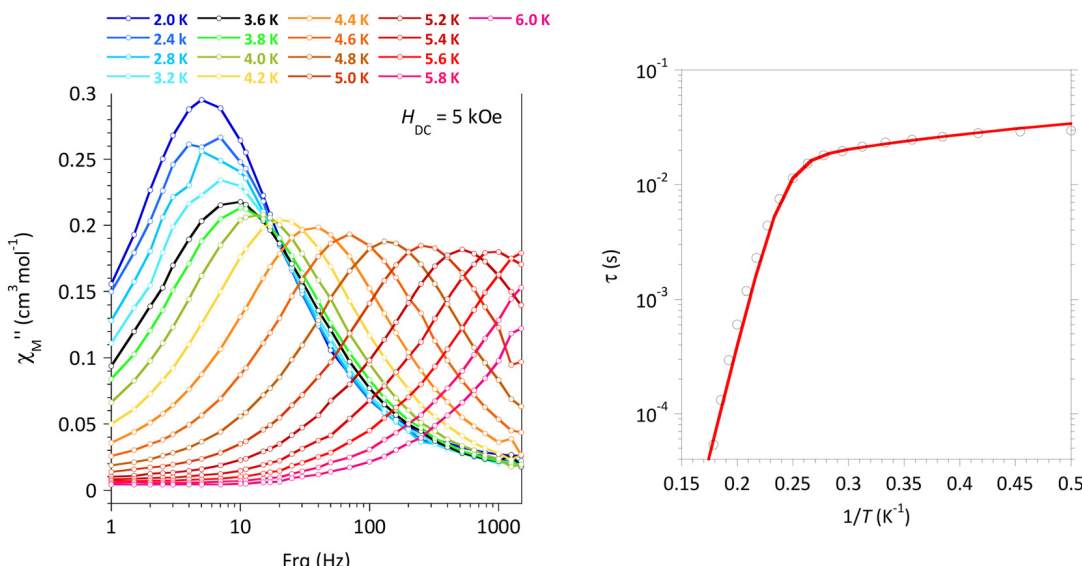


Fig. 2 (a)  $\chi_M T$  versus  $T$  for **1**, **3**, and **4** and (b)  $M$  versus  $H$  at 2 K for **4** and **5**.





**Fig. 3**  $[\text{FeL}^{N_5}\text{Br}_2]$ , 3: (left panel)  $\chi''_M$  versus  $\nu$ , in the 2–6 K temperature range with  $H_{\text{DC}} = 5$  kOe; (right panel) experimental (O) and calculated (—) relaxation time,  $\tau$ , versus  $1/T$  with best-fit associated with eqn (6) (see the main text).

dampened by the application of a DC field (Fig. S13e and f†). In the field, the maximum of  $\chi''_M$  at 2 K steadily shifts to a lower frequency until about 5 kOe, suggesting QTM cancellation, but it also continuously increases in intensity with DC fields up to 10 kOe (Fig. S13e†). The latter trend can be attributed to a gradual decoupling of intermolecular interactions by the applied field.

The relaxation times,  $\tau$ , for **4** in the absence of an applied field could be obtained between 2 and 6.4 K from the analyses of  $\chi''_M$  versus  $\nu$  behaviors by a generalized Debye model (Fig. S13c and Table S4†). The plot of  $\tau$  versus  $1/T$  (Fig. S13d†) shows three domains characteristic of temperature activated relaxation (6.4–5.8 K),  $T$ -independent relaxation (5.6 to about 3.5 K), and for lower  $T$  a steady increase of the relation time

likely due to the intermolecular interactions taking place at these temperatures. The temperature dependence of  $\tau$  between 6.4 and 3.0 K is well modeled by an expression combining an Orbach process and QTM (first and third terms in eqn (6)). Best fit gave  $U/k_B = 76 \pm 6$  K,  $\tau_0 = 8 \times 10^{-10}$  s, and QTM =  $3.41 \times 10^{-4}$  s (Fig. S13d†), confirming the SMM behavior in zero-field for **4**.

In order to avoid the contribution of the QTM, an investigation of the SMM characteristics was performed with an applied field of 5 kOe (Fig. S13g–l†). Under these conditions, the temperature dependence of the relaxation of the relaxation time follows an Orbach behavior in the higher T-domain and a Direct process below 5 K, characterized by  $U/k_B = 99 \pm 8$  K,  $\tau_0 = 3 \times 10^{-11}$  s, and  $DH^n = 11.47 \pm 0.09 \text{ K}^{-1} \text{ s}^{-1}$ . It can be noticed

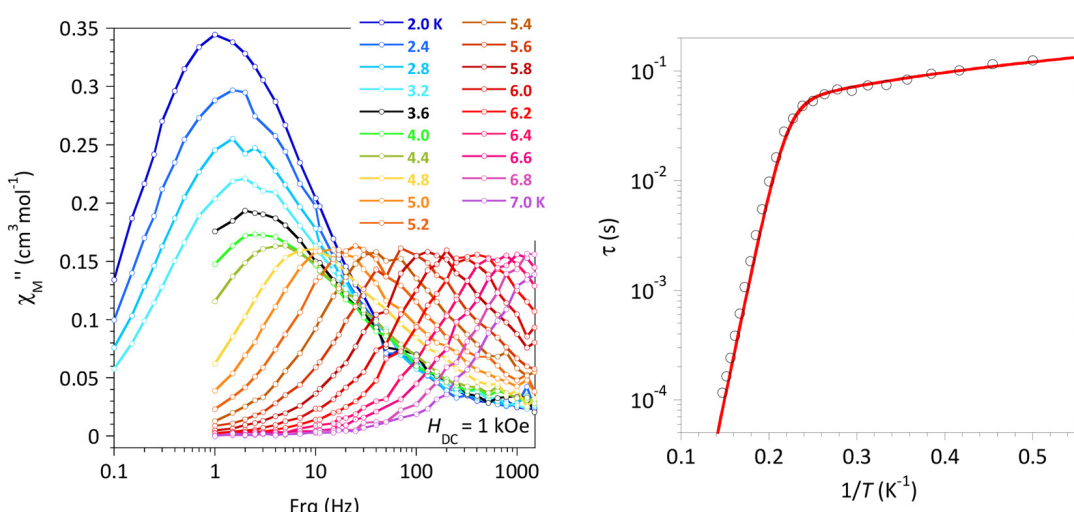


**Fig. 4**  $[\text{Fe}_{0.12}\text{Zn}_{0.88}\text{L}^{N_5}\text{I}_2]$ , 5: (left panel)  $\chi''_M$  versus  $\nu$  with  $H_{\text{DC}} = 1$  kOe, in the 2–7 K temperature range; (right panel) experimental (O) and calculated (—) relaxation time  $\tau$  versus  $1/T$  with best-fit associated with eqn (6) (see the main text).



that these parameters are very similar to those of the Br-derivative, 3.

For the solid solution of  $[\text{FeL}^{\text{N}5}\text{I}_2]$  in  $[\text{ZnL}^{\text{N}5}\text{I}_2]$ , 5, AC magnetic susceptibility recorded in the absence of an applied static magnetic field confirms the emergence of a  $\chi''_M$  signal below 9 K for a test frequency of 997 Hz (Fig. S14a†). However, the profile of the behavior, with a poorly resolved peak and a continuously increasing contribution with decreasing temperature, is a characteristic of rapid relaxation processes such as QTM. The latter is quenched when a static field is applied; for 5, 1 kOe was found to be optimal (Fig. S14b†) and was applied for detailed AC studies. The  $\chi''_M$  versus  $\nu$  behavior at different temperatures between 2 and 7 K and the related temperature dependence of  $\tau$  are depicted in Fig. 4 (additional plots are shown in Fig. S14†). And here again,  $\tau$  versus  $1/T$  of  $[\text{FeL}^{\text{N}5}\text{I}_2]$  in 5 is perfectly modeled using an Orbach and a Direct process (eqn (6)) with  $U/k_B = 88 \pm 9$  K,  $\tau_0 = 2 \times 10^{-10}$  s, and  $DH'' = 4.13 \pm 0.04$  K $^{-1}$  s $^{-1}$ . The energy barrier for magnetization reversal is very similar to that obtained for the bulk  $[\text{FeL}^{\text{N}5}\text{I}_2]$ , confirming the molecular origin of the low  $T$  magnetization freezing. No evidence for magnetic hysteresis was found in the  $M$  versus  $H$  behaviors recorded at 2 and 5 K (Fig. S10†).

An SMM-type behavior with a magnetization reversal regulated mainly by a thermal activation is clearly evidenced for 2–5. For the I-derivative, slow magnetization relaxation is even observed in zero-field, a behavior hardly found in mononuclear 3d ion SMMs. For all, the effective energy barriers,  $U/k_B$ , are much larger than those usually reported for PBP complexes of Fe(II),<sup>27</sup> and reach that described for linear two-coordinated Fe(II) with first-order SOC.<sup>15</sup>

## Concluding remarks

Unlike lanthanide ions, 1<sup>st</sup>-order spin-orbit coupling is cancelled by the ligand field for transition metal ions, and achieving high magnetic anisotropy is generally considered the Holy Grail for these ions. The results gathered herein show that the contribution from first-order SOC is not confined to low coordination number complexes but can be implemented in a pentagonal bipyramidal Fe(II) complex by appropriate chemical design.

The rigid pentadentate ligand, L<sup>N5</sup>, imposes an effective equatorial coordination sphere close to a pentagonal and symmetrical ligand field, and apical ligands (halogens in the present case), which exhibit a very similar overlap with the d<sub>xz</sub> and d<sub>yz</sub> orbitals, lead to a quasi-degenerate state for these orbitals sharing 3 electrons. The mixing of the M<sub>s</sub> levels, revealed by the theoretical calculations, confirms the existence of the 1<sup>st</sup>-order SOC and rules out the possibility of describing the magnetic behavior within the ZFS formalism.

Further evidence is provided by the experimental behavior, which is consistent with the existence of large magnetic anisotropy, the most salient feature being the SMM behavior with large energy barriers for magnetization reversal. The

observation of such a behavior without an applied static magnetic field is quite unique for a mononuclear 3d complex.

Finally, such complexes with quasi-degenerated magnetic orbitals are also desirable building units for the design of exchange-coupled polynuclear compounds. Some recent studies have shown that close to a first-order SOC regime, anisotropic interactions such as the Dzyaloshinskii–Moriya<sup>63,64</sup> or the symmetric exchange tensor of anisotropy may also reach high values.<sup>65,66</sup>

## Experimental section

### Materials and methods

All the chemicals used were commercially available and were employed without further purification. 2,9-Di( $\alpha$ -methylhydrazino)-1,10-phenanthroline·2HCl, denoted as Phen<sup>MeNH<sub>2</sub></sup>·2HCl, was synthesized from methylhydrazine and 2,9-dichloro-1,10-phenanthroline<sup>67</sup> according to a literature procedure.<sup>68</sup> All the syntheses of Fe<sup>II</sup> complexes were carried out under N<sub>2</sub> using Schlenk techniques and degassed solvents (diethyl ether was purified using an Innovative Technology Solvent Purification® system while the alcohol and water solvents were distilled under N<sub>2</sub> prior to use). The solid samples for the characterization of the Fe<sup>II</sup> complexes were prepared in a glovebox. Technical information can be found in the ESI.†

### Synthetic procedures

**[FeL<sup>N5</sup>(H<sub>2</sub>O)Cl]Cl·4.5H<sub>2</sub>O** **1.** FeCl<sub>2</sub>·4H<sub>2</sub>O (100.0 mg; 0.54 mmol) was solubilized in 70 mL of water, followed by the addition of ascorbic acid (100.0 mg; 0.57 mmol). Phen<sup>MeNH<sub>2</sub></sup>·2HCl (170.0 mg; 0.54 mmol) was then added to the solution that turned yellow. The addition of 2,6-diacyetylpyridine (81.0 mg; 0.54 mmol) followed by 3 drops of 37% aqueous HCl solution turned the solution color to olive green. The reaction mixture was heated to reflux for 1 h and then concentrated to 10 mL before being stored overnight at 5 °C. Dark green-brown crystals suitable for X-ray diffraction were collected by filtration and washed with cold methanol, shortly dried under vacuum and stored under a nitrogen atmosphere (164.0 mg, 49%). Elemental analysis: calcd for C<sub>23</sub>H<sub>29</sub>N<sub>7</sub>Cl<sub>2</sub>FeO<sub>4.5</sub> (with the loss of 1 H<sub>2</sub>O molecule of the solvent) C, 45.79; H, 5.01; N, 16.25. Found C, 45.96; H, 4.93; N, 16.22. IR ( $\nu_{\text{max}}$ /cm<sup>-1</sup>): 3317br, 3170br, 2989w, 1589vs, 1575vs, 1553s, 1486vsbr, 1419s, 1363s, 1300s, 1186s, 1148vs, 1090vs, 1045vs, 858vs, 736w, 686w, 664w, 624vw.

**[FeL<sup>N5</sup>Br<sub>2</sub>] 3 and [FeL<sup>N5</sup>I<sub>2</sub>] 4.** 3 and 4 were synthesized following the same procedure as that for 1. 48% HBr and 47% HI aqueous solutions were used instead of HCl to acidify the reaction mixture after the addition of 2,6-diacyetylpyridine. The addition of NaBr (500.0 mg; 4.85 mmol) or NaI (800.0 mg; 5.33 mmol) at the end of the reflux time formed dark green crystals of 3 (121 mg, 41%) or 4 (176 mg, 50%), respectively, and these were isolated after cooling the solution to 5 °C for several days. For 3, elemental analysis: calcd for C<sub>23</sub>H<sub>21</sub>N<sub>7</sub>Br<sub>2</sub>Fe C, 45.20; H, 3.46; N, 16.04. Found C, 45.35; H,



3.47; N, 16.20. IR ( $\nu_{\text{max}}/\text{cm}^{-1}$ ): 3039w, 2951w, 1590vs, 1575vs, 1545s, 1495vs, 1473s, 1427s, 1409s, 1359s, 1302s, 1256s, 1187s, 1150vs, 1094vs, 1027vs, 1009s, 953s, 873vs, 812s, 795s, 742s, 658w. For **4**, elemental analysis: calcd for  $\text{C}_{23}\text{H}_{21}\text{N}_7\text{FeI}_2$  C, 39.18; H, 3.00; N, 13.90. Found C, 39.08; H, 2.74; N, 13.66. IR ( $\nu_{\text{max}}/\text{cm}^{-1}$ ): 3037w, 3000w, 1589vs, 1573vs, 1542s, 1494vs, 1471s, 1451s, 1423s, 1405s, 1354s, 1302s, 1255s, 1180s, 1148vs, 1091vs, 1026vs, 867vs, 798s, 740s, 695w, 658w.

[ $\text{Fe}_{0.12}\text{Zn}_{0.88}\text{L}^{\text{N}^5}\text{I}_2$ ] **5**.  $\text{FeCl}_2 \cdot 4\text{H}_2\text{O}$  (8.0 mg; 0.040 mmol) and  $\text{Zn}(\text{NO}_3)_2 \cdot 6\text{H}_2\text{O}$  (118.0 mg; 0.40 mmol) were solubilized in 40 mL of  $\text{H}_2\text{O}$ . Ascorbic acid was added (20.0 mg; 0.11 mmol) followed by  $\text{Phen}^{\text{MeNH}_2} \cdot 2\text{HCl}$  (113.0 mg; 0.36 mmol), 2,6-diacetylpyridine (69.0 mg; 0.42 mmol), and then 3 drops of 47% HI aqueous solution. The solution turned yellowish green and it was heated to reflux for 1 h. A brown-yellow precipitate started to appear during the heating time. NaI (380.0 mg; 2.53 mmol) was added before allowing the suspension to cool down to room temperature. The solid was then isolated by filtration through a cannula and filter paper. It was washed with acetone and dried under vacuum (120.0 mg, 47%). Elemental analysis: calcd for  $\text{C}_{23}\text{H}_{21}\text{N}_7\text{Fe}_{0.12}\text{I}_2\text{Zn}_{0.88}$  C, 38.72; H, 2.97; N, 13.74. Found C, 38.70; H, 2.95; N, 13.75. EDX analysis (Fig. S9†) was performed on several crystals that confirmed the presence of both Fe (12 mol%) and Zn (88 mol%). IR ( $\nu_{\text{max}}/\text{cm}^{-1}$ ): 3035w, 3010w, 1592vs, 1571vs, 1542s, 1494vs, 1470s, 1450s, 1427s, 1408s, 1355s, 1302s, 1255s, 1179s, 1148vs, 1091vs, 1030vs, 866vs, 798s, 739s, 693w, 658w.

### Single-crystal X-ray diffraction

Intensity data were collected at low temperature on an Apex2 Bruker diffractometer equipped with a 30 W air-cooled micro-focus source ( $\lambda = 0.71073 \text{ \AA}$ ). Structures for **1**, **3**, **4**, [ $\text{ZnL}^{\text{N}^5}\text{Br}$ ] $\cdot\text{Br}$  and  $\text{ZnL}^{\text{N}^5}\text{I}_2$  were solved using SUPERFLIP<sup>69</sup> or ShelxT<sup>70</sup> and refined by means of least squares procedures using the PC version of the CRYSTALS program.<sup>71</sup> Atomic scattering factors were taken from the international tables for X-ray crystallography.<sup>72</sup> All non-hydrogen atoms were refined anisotropically. Structure for **2** was found to be modulated with a modulation vector of  $0.6754a + 0.1052c$ . The structure was solved by charge flipping methods using the SUPERFLIP program<sup>69</sup> using the super-space group  $C2/m(a0g)0s$  and refined using Jana2006.<sup>73</sup> The structure is composed of two superimposed inversed configurations of the complex. The incommensurately modulated structure of this complex was successfully solved and refined in (3 + 1) dimensions, evidencing an ordered-disorder along the fourth dimension as well as a significant atomic displacement from the average positions. Additional information can be found in the ESI.†

### Computational information

CASSCF and NEVPT2 calculations were performed with Orca5.0 package<sup>59</sup> considering 6 active electrons and 5 active MOs, *i.e.* those with a major Fe 3d character. Extended DKH-def2 atomic basis sets were used for all atoms except I: QZVPP for Fe atoms (14s10p5d4f2 g), TZVP for C (6s3p2d1f), N (6s3p2d1f), O (6s3p2d1f), Cl (8s4p2d1f), Br (10s8p4d1f), SVP

for H atoms (2s1p) and a 15s11p5d1f basis set for I atoms. Optimization of the positions of the H atoms was performed by DFT calculations using def2-SVP atomic basis sets and the PBE functional.

## Data availability

Crystallographic data have been deposited at the CCDC under 2352840 (**1**), 2352845 (**2**), 2352841 (**3**), 2352842 (**4**), 2352843 ([ $\text{ZnL}^{\text{N}^5}\text{Br}$ ] $\cdot\text{Br}$ ), and 2352844 ( $\text{ZnL}^{\text{N}^5}\text{I}_2$ ) and can be obtained from <https://www.ccdc.cam.ac.uk/structures/>.

## Conflicts of interest

There are no conflicts to declare.

## Acknowledgements

The authors are grateful to M. J.-F. Meunier (LCC) and M. V. Collière (LCC) for technical assistance in magnetic, Mössbauer, and EDX data collection.

## References

- D. Gatteschi, R. Sessoli and J. Villain, *Molecular Nanomagnets*, Oxford University Press, Oxford, 2006.
- C. Coulon, H. Miyasaka and R. Clérac, in *Single-Molecule Magnets and Related Phenomena*, ed. R. Winpenny, Springer, Berlin, 2006, vol. 122, pp. 163–206.
- J. D. Rinehart and J. R. Long, Exploiting single-ion anisotropy in the design of f-element single-molecule magnets, *Chem. Sci.*, 2011, **2**, 2078.
- S. Gomez-Coca, E. Cremades, N. Aliaga-Alcalde and E. Ruiz, Mononuclear Single-Molecule Magnets: Tailoring the Magnetic Anisotropy of First-Row Transition-Metal Complexes, *J. Am. Chem. Soc.*, 2013, **135**, 7010–7018.
- S. T. Liddle and J. van Slageren, Improving f-element single molecule magnets, *Chem. Soc. Rev.*, 2015, **44**, 6655–6669.
- J. M. Frost, K. L. M. Harriman and M. Murugesu, The rise of 3-d single-ion magnets in molecular magnetism: towards materials from molecules?, *Chem. Sci.*, 2016, **7**, 2470–2491.
- J.-L. Liu, Y.-C. Chen and M.-L. Tong, Symmetry strategies for high performance lanthanide-based single-molecule magnets, *Chem. Soc. Rev.*, 2018, **47**, 2431–2453.
- P. Kumar Sahu, R. Kharel, S. Shome, S. Goswami and S. Konar, Understanding the unceasing evolution of Co(II) based single-ion magnets, *Coord. Chem. Rev.*, 2023, **475**, 214871.
- E. A. Boudreaux and L. N. Mulay, *Theory and applications of molecular paramagnetism*, Wiley-Interscience Publication, 1976.



- Open Access Article. Published on 18 March 2025. Downloaded on 9/30/2025 12:58:09 PM.  
This article is licensed under a Creative Commons Attribution-NonCommercial 3.0 Unported Licence.
- 
- 10 L. Sorace, C. Benelli and D. Gatteschi, Lanthanides in molecular magnetism: old tools in a new field, *Chem. Soc. Rev.*, 2011, **40**, 3092.
  - 11 R. Boca, Zero-field splitting in metal complexes, *Coord. Chem. Rev.*, 2004, **248**, 757–815.
  - 12 A. K. Bar, C. Pichon and J.-P. Sutter, Magnetic anisotropy in two- to eight-coordinated transition-metal complexes: Recent developments in molecular magnetism, *Coord. Chem. Rev.*, 2016, **308**, 346–380.
  - 13 W. M. Reiff, A. M. LaPointe and E. H. Witten, Virtual Free Ion Magnetism and the Absence of Jahn-Teller Distortion in a Linear Two-Coordinate Complex of High-Spin Iron(II), *J. Am. Chem. Soc.*, 2004, **126**, 10206–10207.
  - 14 W. M. Reiff, C. E. Schulz, M.-H. Whangbo, J. I. Seo, Y. S. Lee, G. R. Potratz, C. W. Spicer and G. S. Girolami, Consequences of a Linear Two-Coordinate Geometry for the Orbital Magnetism and Jahn-Teller Distortion Behavior of the High Spin Iron(II) Complex  $\text{Fe}[\text{N}(\text{t-Bu})_2]_2$ , *J. Am. Chem. Soc.*, 2009, **131**, 404–405.
  - 15 J. M. Zadrozny, M. Atanasov, A. M. Bryan, C.-Y. Lin, B. D. Rekken, P. P. Power, F. Neese and J. R. Long, Slow magnetization dynamics in a series of two-coordinate iron (II) complexes, *Chem. Sci.*, 2013, **4**, 125–138.
  - 16 J. M. Zadrozny, D. J. Xiao, M. Atanasov, G. J. Long, F. Grandjean, F. Neese and J. R. Long, Magnetic blocking in a linear iron(I) complex, *Nat. Chem.*, 2013, **5**, 577–581.
  - 17 W. H. Harman, T. D. Harris, D. E. Freedman, H. Fong, A. Chang, J. D. Rinehart, A. Ozarowski, M. T. Sougrati, F. Grandjean, G. J. Long, J. R. Long and C. J. Chang, Slow Magnetic Relaxation in a Family of Trigonal Pyramidal Iron (II) Pyrrolide Complexes, *J. Am. Chem. Soc.*, 2010, **132**, 18115.
  - 18 A. V. Palii, J. M. Clemente-Juan, E. Coronado, S. I. Klokishner, S. M. Ostrovsky and O. S. Reu, Role of Orbital Degeneracy in the Single Molecule Magnet Behavior of a Mononuclear High-Spin Fe(II) Complex, *Inorg. Chem.*, 2010, **49**, 8073–8077.
  - 19 P. C. Bunting, M. Atanasov, E. Damgaard-Møller, M. Perfetti, I. Crassee, M. Orlita, J. Overgaard, J. van Slageren, F. Neese and J. R. Long, A linear cobalt(II) complex with maximal orbital angular momentum from a non-Aufbau ground state, *Science*, 2018, **362**, 7319.
  - 20 X.-N. Yao, J.-Z. Du, Y.-Q. Zhang, X.-B. Leng, M.-W. Yang, S.-D. Jiang, Z.-X. Wang, Z.-W. Ouyang, L. Deng, B.-W. Wang and S. Gao, Two-Coordinate Co(II) Imido Complexes as Outstanding Single-Molecule Magnets, *J. Am. Chem. Soc.*, 2017, **139**, 373–380.
  - 21 R. Ruamps, R. Maurice, L. Batchelor, M. Boggio-Pasqua, R. Guillot, A. L. Barra, J. Liu, E.-E. Bendeif, S. Pillet, S. Hill, T. Mallah and N. Guihéry, Giant Ising-Type Magnetic Anisotropy in Trigonal Bipyramidal Ni(II) Complexes: Experiment and Theory, *J. Am. Chem. Soc.*, 2013, **135**, 3017–3026.
  - 22 S. Gómez-Coca, E. Cremades, N. Aliaga-Alcalde and E. Ruiz, Huge Magnetic Anisotropy in a Trigonal-Pyramidal Nickel (II) Complex, *Inorg. Chem.*, 2013, **53**, 676–678.
  - 23 R. C. Poulsen, M. J. Page, A. G. Algarra, J. J. Le Roy, I. López, E. Carter, A. Llobet, S. A. Macgregor, M. F. Mahon, D. M. Murphy, M. Murugesu and M. K. Whittlesey, Synthesis, Electronic Structure, and Magnetism of  $[\text{Ni}(6\text{-Mes})_2]^+$ : A Two-Coordinate Nickel(I) Complex Stabilized by Bulky N-Heterocyclic Carbenes, *J. Am. Chem. Soc.*, 2013, **135**, 13640–13643.
  - 24 W. A. Merrill, T. A. Stich, M. Brynda, G. J. Yeagle, J. C. Fettinger, R. De Hont, W. M. Reiff, C. E. Schulz, R. D. Britt and P. P. Power, Direct Spectroscopic Observation of Large Quenching of First-Order Orbital Angular Momentum with Bending in Monomeric, Two-Coordinate Fe(II) Primary Amido Complexes and the Profound Magnetic Effects of the Absence of Jahn– and Renner–Teller Distortions in Rigorously Linear Coordination, *J. Am. Chem. Soc.*, 2009, **131**, 12693–12702.
  - 25 M. Atanasov, J. M. Zadrozny, J. R. Long and F. Neese, A theoretical analysis of chemical bonding, vibronic coupling, and magnetic anisotropy in linear iron(II) complexes with single-molecule magnet behavior, *Chem. Sci.*, 2013, **4**, 139–156.
  - 26 M. Atanasov, D. Ganyushin, D. A. Pantazis, K. Sivalingam and F. Neese, Detailed Ab Initio First-Principles Study of the Magnetic Anisotropy in a Family of Trigonal Pyramidal Iron(II) Pyrrolide Complexes, *Inorg. Chem.*, 2011, **50**, 7460–7477.
  - 27 J.-P. Sutter, V. Béreau, V. Jubault, K. Bretosh, C. Pichon and C. Duhayon, Magnetic anisotropy of transition metal and lanthanide ions in pentagonal bipyramidal geometry, *Chem. Soc. Rev.*, 2022, **51**, 3280–3313.
  - 28 R. Ruamps, L. J. J. Batchelor, R. Maurice, N. Gogoi, P. Jiménez-Lozano, N. Guihéry, C. de Graaf, A.-L. Barra, J.-P. Sutter and T. Mallah, Origin of the Magnetic Anisotropy in Ni(II) and Co(II) Heptacoordinate Complexes, *Chem. – Eur. J.*, 2013, **19**, 950–957.
  - 29 A. K. Bar, N. Gogoi, C. Pichon, V. M. L. D. P. Goli, M. Thlijeni, C. Duhayon, N. Suaud, N. Guihéry, A.-L. Barra, S. Ramasesha and J.-P. Sutter, Pentagonal Bipyramid FeII Complexes: Robust Ising-Spin Units towards Heteropolynuclear Nanomagnets, *Chem. – Eur. J.*, 2017, **23**, 4380–4396.
  - 30 P. Antal, B. Drahoš, R. Herchel and Z. Trávníček, Structure and Magnetism of Seven-Coordinate FeIII, FeII, CoII and NiII Complexes Containing a Heptadentate 15-Membered Pyridine-Based Macroyclic Ligand, *Eur. J. Inorg. Chem.*, 2018, 4286–4297.
  - 31 A. Mondal, S.-Q. Wu, O. Sato and S. Konar, Effect of Axial Ligands on Easy-Axis Anisotropy and Field-Induced Slow Magnetic Relaxation in Heptacoordinated FeII Complexes, *Chem. – Eur. J.*, 2020, **26**, 4780–4789.
  - 32 V. Jubault, B. Pradines, C. Pichon, N. Suaud, C. Duhayon, N. Guihéry and J.-P. Sutter, Homochiral SCM Built of Tetrahedral and Pentagonal Bipyramidal Fe(II) Units Bridged by Chlorine, *Cryst. Growth Des.*, 2023, **23**, 1229–1237.
  - 33 M. M. Bishop, J. Lewis, T. D. O'Donoghue, P. R. Raithby and J. N. Ramsden, Chemistry of polydentate ligands. Part

8. Preparation and properties of iron(II) complexes with quinquedentate macrocyclic ligands. Crystal and molecular structure of a compound where high-spin Fe sits in the ligand cavity. Electrochemistry of a series of complexes with the macrocycles, *Dalton Trans.*, 1980, 1390–1396.
- 34 M. M. Bishop, J. Lewis, T. D. O'Donoghue, P. R. Raithby and J. N. Ramsden, X-Ray crystal structure of a planar, high-spin iron(II) complex of a pentadentate unsaturated macrocycle formed by reaction of 2,9-di(1-methylhydrazino)1,10-phenanthroline monohydrochloride with 2,6-diacetylpyridine, *J. Chem. Soc., Chem. Commun.*, 1978, 828–829.
- 35 L. R. Hanton and P. R. Raithby, Diaqua[7,15-dihydro-7,9,13,15-tetramethylpyrido[2',1',6':12,13,14][1,2,4,7,9,10,13]heptaazacyclopentadeca[3,4,5,6,7,8-aklmn][1,10]phenanthroline]cobalt(II) bis(tetrafluoroborate) [Co(H<sub>2</sub>O)<sub>2</sub>(tdmmb)][BF<sub>4</sub>]<sub>2</sub>, *Acta Crystallogr., Sect. B*, 1980, **36**, 1489–1491.
- 36 C. W. G. Ansell, J. Lewis, P. R. Raithby, J. N. Ramsden and M. Schroder, X-Ray crystal structure of the pentagonal bipyramidal nickel(II) complex [Ni(L)(H<sub>2</sub>O)<sub>2</sub>](BF<sub>4</sub>)<sub>2</sub> and the selective stabilisation of the nickel(II) oxidation state by a quinquedentate macrocyclic ligand, *J. Chem. Soc., Chem. Commun.*, 1982, 546–547.
- 37 D. Shao, S.-L. Zhang, L. Shi, Y.-Q. Zhang and X.-Y. Wang, Probing the Effect of Axial Ligands on Easy-Plane Anisotropy of Pentagonal-Bipyramidal Cobalt(II) Single-Ion Magnets, *Inorg. Chem.*, 2016, **55**, 10859–10869.
- 38 K. Bretosh, V. Béreau, C. Duhayon, C. Pichon and J.-P. Sutter, A ferromagnetic Ni(II)-Cr(III) single-chain magnet based on pentagonal bipyramidal building units, *Inorg. Chem. Front.*, 2020, **7**, 1503–1511.
- 39 D. Casanova, P. Alemany, J. M. Bofill and S. Alvarez, Shape and symmetry of heptacoordinated transition-metal complexes: structural trends, *Chem. – Eur. J.*, 2003, **9**, 1281–1295.
- 40 M. Llunell, D. Casanova, J. Cirera, P. Alemany and S. Alvarez, *SHAPE: Program for the stereochemical analysis of molecular fragments by means of continuous shape measures and associated tools*, University of Barcelona, Barcelona, 2013.
- 41 J. Lewis, T. D. O'Donoghue and P. R. Raithby, Chemistry of polydentate ligands. Part 7. Synthesis, characterisation, and properties of some manganese(II) complexes of quinquedentate macrocyclic ligands based on 1,10-phenanthroline. Crystal and molecular structure of a complex with pentagonal-pyramidal coordination geometry about the Mn, *Dalton Trans.*, 1980, 1383–1389.
- 42 M. G. Drew, A. Hamid Bin Othman, W. Hill, P. McIlroy and S. M. Nelson, Seven-coordinate complexes of iron(II) with pentadentate macrocyclic ligands, *Inorg. Chim. Acta*, 1975, **12**, L25–L26.
- 43 T. S. Venkatakrishnan, S. Sahoo, N. Bréfuel, C. Duhayon, C. Paulsen, A.-L. Barra, S. Ramasesha and J.-P. Sutter, Enhanced Ion Anisotropy by Nonconventional Coordination Geometry: Single-Chain Magnet Behavior for a [{FeIIL}<sub>2</sub>{NbIV(CN)<sub>8</sub>}]-Helical Chain Compound Designed with Heptacoordinate FeII, *J. Am. Chem. Soc.*, 2010, **132**, 6047–6056.
- 44 B. Drahoš, R. Herchel and Z. Trávníček, Single-Chain Magnet Based on 1D Polymeric Azido-Bridged Seven-Coordinate Fe(II) Complex with a Pyridine-Based Macroyclic Ligand, *Inorg. Chem.*, 2018, **57**, 12718–12726.
- 45 A. S. M. Al-Shihri, J. R. Dilworth, S. D. Howe, J. Silver, R. M. Thompson, J. Davies and D. C. Povey, Synthesis and characterization of some novel pentagonal bipyramidal 2,6-diacetylpyridine bis(benzoylhydrazone) (DAPBH<sub>2</sub>) complexes of Rhenium(III) and molybdenum crystal and molecular structure of [ReCl(DAPB)(PPh<sub>3</sub>)]. An investigation of the Mössbauer spectroscopy of [FeIICl<sub>2</sub>(DAPBH<sub>2</sub>)].H<sub>2</sub>O and [FeIIICl(DAP-Me-B)(H<sub>2</sub>O)], *Polyhedron*, 1993, **12**, 2297–2305.
- 46 H. S. Soo, M. T. Sougrati, F. Grandjean, G. J. Long and C. J. Chang, A seven-coordinate iron platform and its oxo and nitrene reactivity, *Inorg. Chim. Acta*, 2011, **369**, 82–91.
- 47 A. K. Bar, C. Pichon, N. Gogoi, C. Duhayon, S. Ramasesha and J.-P. Sutter, Single-ion magnet behaviour of heptacoordinated Fe(II) complexes: on the importance of supramolecular organization, *Chem. Commun.*, 2015, **51**, 3616–3619.
- 48 C. Pichon, N. Suaud, V. Jubault, C. Duhayon, N. Guihéry and J.-P. Sutter, Trinuclear Cyanido-Bridged [Cr<sub>2</sub>Fe] Complexes: To Be or not to Be a Single-Molecule Magnet, a Matter of Straightness, *Chem. – Eur. J.*, 2021, **27**, 15484–15495.
- 49 Y. P. Tupolova, D. V. Korchagin, A. S. Andreeva, V. V. Tkachev, G. V. Shilov, V. A. Lazarenko, L. D. Popov, K. A. Babeshkin, N. N. Efimov, R. B. Morgunov, A. V. Palii, S. P. Kubrin, I. N. Shcherbakov and S. M. Aldoshin, Mononuclear Heptacoordinated 3d-Metal Helicates as a New Family of Single Ion Magnets, *Magnetochemistry*, 2022, **8**, 153.
- 50 F. A. Deeney and S. M. Nelson, Relaxation effects in the mössbauer spectra of some seven-coordinate iron(III) complexes, *J. Phys. Chem. Solids*, 1973, **34**, 277–282.
- 51 D. Darmanović, I. N. Shcherbakov, C. Duboc, V. Spasojević, D. Hanžel, K. Andelković, D. Radanović, I. Turel, M. Milenković, M. Gruden, B. Čobeljić and M. Zlatar, Combined Experimental and Theoretical Investigation of the Origin of Magnetic Anisotropy in Pentagonal Bipyramidal Isothiocyanato Co(II), Ni(II), and Fe(III) Complexes with Quaternary-Ammonium-Functionalized 2,6-Diacetylpyridine Bisacylhydrazone, *J. Phys. Chem. C*, 2019, **123**, 31142–31155.
- 52 R. Maurice, R. Bastardis, C. D. Graaf, N. Suaud, T. Mallah and N. Guihéry, Universal Theoretical Approach to Extract Anisotropic Spin Hamiltonians, *J. Chem. Theory Comput.*, 2009, **5**, 2977–2984.
- 53 R. S. Fishman and F. A. Reboreda, Magnetic anisotropy in the Fe(II)Fe(III) bimetallic oxalates, *Phys. Rev. B: Condens. Matter Mater. Phys.*, 2008, **77**, 144421.
- 54 C. K. Jorgensen, *Orbitals in atoms and molecules*, Academic Press, London, 1962.
- 55 C. K. Jørgensen, in *Advances in Chemical Physics*, ed. I. Prigogine, 1963, vol. 5, pp. 33–146.



- 56 C. K. Jørgensen, in *Structure and Bonding*, ed. C. K. Jørgensen, J. B. Neilands, R. S. Nyholm, D. Reinen and R. J. P. Williams, Springer Berlin Heidelberg, Berlin, Heidelberg, 1969, pp. 94–115.
- 57 A. Bencini, C. Benelli and D. Gatteschi, The angular overlap model for the description of the paramagnetic properties of transition metal complexes, *Coord. Chem. Rev.*, 1984, **60**, 131–169.
- 58 F. Neese and E. I. Solomon, Calculation of Zero-Field Splittings, g-Values, and the Relativistic Nephelauxetic Effect in Transition Metal Complexes. Application to High-Spin Ferric Complexes, *Inorg. Chem.*, 1998, **37**, 6568–6582.
- 59 F. Neese, F. Wennmohs, U. Becker and C. Ripplinger, The ORCA quantum chemistry program package, *J. Chem. Phys.*, 2020, **152**, 224108.
- 60 B. R. McGarvey and J. Telser, Simple Ligand-Field Theory of d<sub>4</sub> and d<sub>6</sub> Transition Metal Complexes with a C<sub>3</sub> Symmetry Axis, *Inorg. Chem.*, 2012, **51**, 6000–6010.
- 61 Y. Hosokoshi, M. Tamura, D. Shiomi, N. Iwasawa, K. Nozawa, M. Kinoshita, H. Aruga Katori and T. Goto, Organic radical crystals,  $\alpha$ -nitronyl nitroxide family: High-field magnetization study, *Phys. B*, 1994, **201**, 497–499.
- 62 C. Dekker, A. F. M. Arts, H. W. de Wijn, A. J. van Duyneveldt and J. A. Mydosh, Activated dynamics in a two-dimensional Ising spin glass: Rb<sub>2</sub>Cu<sub>1-x</sub>Co<sub>x</sub>F<sub>4</sub>, *Phys. Rev. B: Condens. Matter Mater. Phys.*, 1989, **40**, 11243.
- 63 I. Dzyaloshinsky, A thermodynamic theory of “weak” ferromagnetism of antiferromagnetics, *J. Phys. Chem. Solids*, 1958, **4**, 241–255.
- 64 T. Moriya, Anisotropic Superexchange Interaction and Weak Ferromagnetism, *Phys. Rev.*, 1960, **120**, 91–98.
- 65 M.-A. Bouammali, N. Suaud, R. Maurice and N. Guihéry, Extraction of giant Dzyaloshinskii–Moriya interaction from ab initio calculations: First-order spin-orbit coupling model and methodological study, *J. Chem. Phys.*, 2021, **155**, 164305.
- 66 M.-A. Bouammali, N. Suaud, C. Martins, R. Maurice and N. Guihéry, How to create giant Dzyaloshinskii–Moriya interactions? Analytical derivation and ab initio calculations on model dicopper(II) complexes, *J. Chem. Phys.*, 2021, **154**, 134301.
- 67 H. C. Guo, R. H. Zheng and H. J. Jiang, Improved Synthesis of 2,9-Dichloro-1,10-phenanthroline, *Org. Prep. Proced. Int.*, 2012, **44**, 392–396.
- 68 J. Lewis and T. D. O'Donoghue, Chemistry of polydentate ligands. Part 5. Complexes of 2,9-di-hydrazino-derivatives of 1,10-phenanthroline. Dependence of co-ordination number of a ligand on the anion present, *Dalton Trans.*, 1980, 736–742.
- 69 L. Palatinus and G. Chapuis, Superflip, *J. Appl. Crystallogr.*, 2007, **40**, 786–790.
- 70 S.-P. V5.4, *Bruker Analytical X-ray Systems*, Madison, WI, 1999.
- 71 P. W. Betteridge, J. R. Carruthers, R. I. Cooper, K. Prout and D. J. Watkin, CRYSTALS, *J. Appl. Crystallogr.*, 2003, **36**, 1487–1487.
- 72 *International Tables for X-ray Crystallography*, ed. A. J. C. Wilson, Kluwer Academic, Dordrecht, 1992.
- 73 M. Dusek, V. Petricek and L. Palatinus, Introduction to JANA2006, *Acta Crystallogr., Sect. A: Found. Crystallogr.*, 2006, **62**, s46.



### 3.2 Impact of the Electric field on the ZFS parameters

This section follows on a previous study of a Ni(II) complex exhibiting strong unaxial anisotropy. This complex has a tetradentate ligand (hexamethyl-2,2',2"-triamino-triethylamine) in which three nitrogen atoms form bonds in the plane with the metal ion, while the fourth nitrogen atom forms a bond in the perpendicular plane, as shown in Figure 3.2. Opposite this fourth nitrogen atom is an apical halide ligand, either chlorine or bromine.

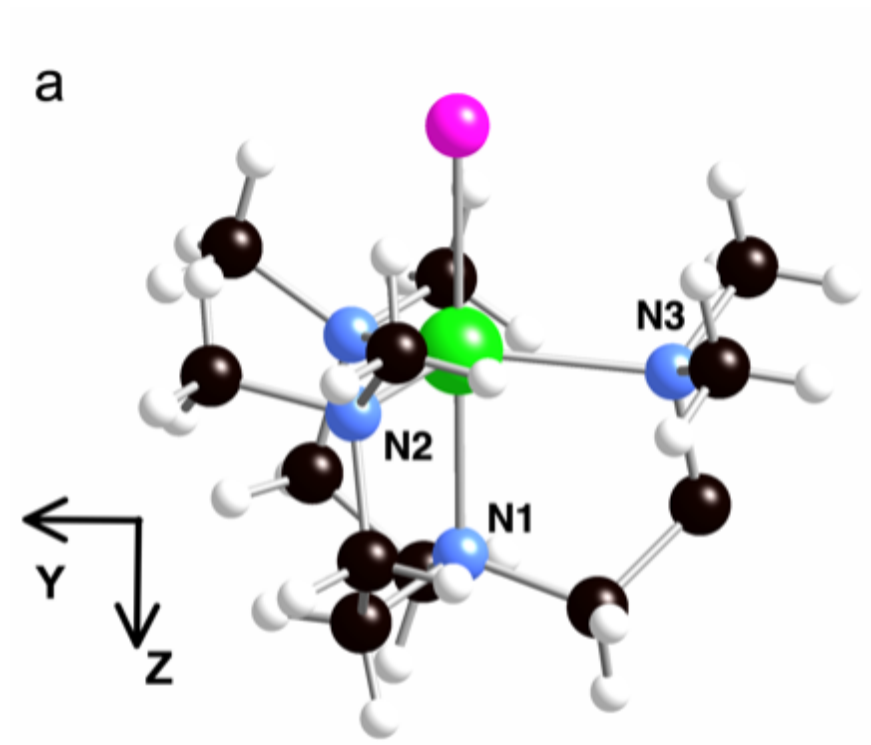


Figure 3.2: Representation of the complex  $[\text{Ni}(\text{Me}_6\text{trenCl})](\text{ClO}_4)$ , Ni in green, Cl, N in blue, C in black and H in white

Cristallographic data indicates that this complex crystallises in the trigonal space  $R_{3c}$  with a  $C_3$  axis of symmetry along the Ni-Cl axis. This coordination induces a degeneracy of the d-orbital that share the same angular component  $m_l=\pm 2(\pm 1)$ , *i.e.*  $d_{xy}(dxz)$  and  $d_{x^2-y^2}(dyz)$ . The conditions for 1<sup>st</sup> order SOC are met between two degenerate ground states carried by the two  $d^8$  configurations depicted on Figure 3.3 (left). This would result in a large splitting of the  $M_S$  components of the ground state with a large value for the D term as strong as the spin orbit coupling constant of the nickel ion ( $\xi_{Ni}=644\text{cm}^{-1}$ ). At this point, a competing effect appears, the Jahn-Teller effect, which breaks the orbital

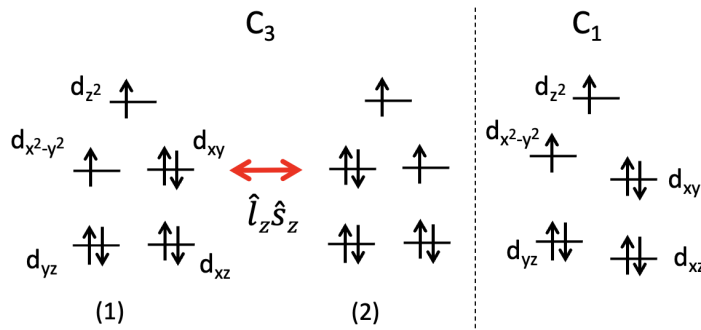


Figure 3.3: Energy diagrams of the d-orbitals in case of three-fold symmetry  $C_3$  (left) and in presence of Jahn-Teller distortion (right) with the induced lift of degeneracy of the d-orbitals.

degeneracy by distorting the complex (mainly removing the Ni atom from the barycenter of the  $N_2$ ,  $N_3$  and  $N_4$  atoms), reducing the axial anisotropy and gives rise to non-zero rhombic term ( $E \neq 0$ ). This distortion is confirmed by both electron paramagnetic resonance (EPR) studies and a theoretical study, which revokes of 1<sup>st</sup>order SOC, leaving only 2<sup>nd</sup>order SOC as the source of the anisotropy.

The ground state is now mainly carried by the configuration illustrated in Figure 3.3 (right) where  $d_{x^2-y^2}$  is simply occupied while  $d_{xy}$  remains doubly occupied. State of the art methodology was applied this complex as to extract the ZFS parameters, the concluding remark was that this complex exhibits strong axial anisotropy with  $D \approx -120\text{cm}^{-1}$  and a significant rhombic term  $E=1.6\text{cm}^{-1}$ . Although the Jahn-Teller effect has a significant impact on the value of the D parameter, it does not completely negate it, which shows that the ligand rigidity is on par with the distortion.

The focus of the present study lies in the interest of controlling the anisotropy via an external stimulus, such as an electric field. While the effect of a magnetic field on the different  $M_S$  components is well understood in terms of the Zeeman effect, it is practically impossible to focus a magnetic field at the nanoscale. This makes it hard to conceptualise any real life application relying on magnetic fields for systems of this scale. Electric fields, however, allow very accurate control at this scale and can affect the magnetic properties of a material via magneto-electric couplings. *Ab initio* calculations allow for the appreciation of the Jahn-Teller distortion as well as the determination of the anisotropic parameters  $D$  and  $E$  as functions of the applied electric field. Such a mechanism can be rationalized by analysing the spin-orbit coupled wave-function and the

contribution of the excited states to the ZFS, both of which are provided by the ORCA program. To identify, discriminate and quantify the mechanisms at the origin of the magneto-electric effect, series of calculations were performed for different orientations and intensity of the electric field. It is then possible to evaluate the effect of:

- (a) electronic structure changes, ZFS calculation under an applied field on the zero-field geometry.
- (b) geometric structure changes, ZFS calculation under no applied field on the field-optimised geometry.
- (c) electronic and geometric changes, both geometry optimisation and ZFS calculation performed under an applied electric field.

In order to explore the response to the electric field for different orientations, the field  $\mathbf{F}$  was initially applied along the Ni-Cl axis, which corresponds to the easy axis of magnetisation. This orientation includes the maximum component of the dipole moment and is referred to as  $\mathbf{F} \parallel Z$ . The electric field was then applied perpendicular to this axis ( $\mathbf{F} \parallel Y$ ) in the YZ plane containing the Ni, N1 and N3 atoms (see to Figure 3.2 for atom numbering). The YZ plane was chosen because the Ni-N3 bond length is the shortest of the three Ni-N bonds in the XY plane.

### Analysis of the contributions

The main contribution to the D term comes from the SOC with the first excited triplet state ( $T^1$ ), which is predominantly expressed in the determinant formed by exciting an electron from the  $d_{x^2-y^2}$  to the  $d_{xy}$  orbitals. The Hamiltonian used to rationalise the SOC is given by  $\hat{H}^{SO} = \sum_i \zeta (\hat{l}_x^i \hat{s}_x^i + \hat{l}_y^i \hat{s}_y^i + \hat{l}_z^i \hat{s}_z^i)$  where  $i$  runs over all the electrons in the  $d^8$  configuration. The two lowest triplets mainly present singly occupied orbitals that are combinations of  $m_l=\pm 2$ , the resulting SOC originates only from the part of the Hamiltonian involving the  $m_s=\pm 1$  of each triplet, *i.e.* from the  $\hat{l}_z^i \hat{s}_z^i$  term. This coupling stabilises the  $m_s=\pm 1$  of the  $T_0$  ground state without affecting the  $m_s=0$  component, which gives a negative contribution to the D term. This contribution can be estimated using second-order perturbation theory:

$$C(D)^{(2)} = -\frac{|\langle T_{\pm 1}^0 | \hat{H}^{SO} | T_{\pm 1}^1 \rangle|^2}{\Delta E} \quad (3.2.1)$$

with  $\Delta E = E(T^1) - E(T^0)$  the energy difference between the two states. As this energy difference is relatively small, a better treatment of the contributions can be obtained by diagonalising the  $2 \times 2$  SOC matrices in the basis of  $T_{\pm 1}^0$  and  $T_{\pm 1}^1$  using a variational approach:

$$C(D)_{VAR} = \frac{\Delta E - \sqrt{\Delta E^2 + 4|SOC|^2}}{2} \quad (3.2.2)$$

where  $|SOC|^2 = |\langle T_{\pm 1}^0 | \hat{H}^{SO} | T_{\pm 1}^1 \rangle|^2$  is the squared value of the off-diagonal term in the SO Hamiltonian between the ground and excited components. Other states may contribute positively or negatively to the overall value of D, their contributions can be obtained in the same way. The ORCA program also provides these contributions and will be used if possible. To approach the finale value of D, one needs to sum all these contributions. However, the variation of the electric field has almost no impact on the contributions of the excited states except for  $T_{\pm 1}^1$ , so they will be excluded from the rationalization. The rhombic term E will be rationalised, but as the sum of the contributions provided by the program does not match the overall variation of the E term, the analysis will be performed using wave functions.

### 3.2.1 Computational Informations

Wave-function based calculations have been performed using the ORCA package. In a first place, CASSCF calculations have been performed to account for non-dynamic correlations. The CAS(8,5) active space contains eight electrons in the five essentially 3d orbitals of the Ni(II) ion, and two sets of orbitals have been optimized using an average procedure over all triplet and all singlet states of the configuration. To account for dynamic correlations at the 2<sup>nd</sup> order of perturbation, NEVPT2 calculations have been carried out for all states. The SI-SO method was then used to account for SOCs between all Ms components of all spin states using CASSCF wave-functions and NEVPT2 correlated energies (*i.e.* as diagonal elements of the SO matrix). ZFS parameters were extracted using a procedure based on the effective Hamiltonian theory which proved to provide accurate values of the anisotropic parameters. The QZVPP extended basis sets have been used for Ni atoms (14s10p5d4f2g), TZVP for all other atoms (6s3p2d1f for N, 8s4p2d1f for Cl and 6s3p2d1f for C) and SVP for H (2s1p). As the field may change the geometrical structure, geometry optimizations were

performed for different values and orientations of the field. We used the Hay-Wadt LanL2TZ(f) basis set for Ni and its corresponding relativistic effective core, Pople triple- $\zeta$  basis set (6-311G) for N and Cl atoms, a Pople double- $\zeta$  plus polarization basis set (6-31G\*) for C atoms, and a Pople double- $\zeta$  basis set (6-31G) for H atoms and the B3LYP functional. Small variations in the geometries have proved to have a large impact on the ZFS parameters, as such the convergence thresholds were set as VERYTIGHT.

The field is applied in the two opposite directions referred as positive  $+F$  and negative  $-F$  with an amplitude of  $|F|=1.028 \cdot 10^9 \text{ V.m}^{-1}$ . The positive direction for the field in the Z direction induces an elongation of the  $\text{Ni}^{2+}\text{-Cl}^-$  bond, *i.e.*, the positive region of the electric potential is above  $\text{Cl}^-$  in Figure 1. The positive direction for the field in the Y direction induces an elongation of the  $\text{Ni}^{2+}\text{-N}_3$ , *i.e.*, the positive region of the electric potential is to the right of  $\text{N}_3$  in Figure 3.2.

### 3.2.2 Application of the electric field along the Z axis

First, we consider the  $\vec{F} \parallel Z$  situation since electric dipole moment is almost along Z, coinciding with the Ni-Cl bond while its components along X and Y are small. Table 3.1 shows the three components of the dipole moment and its magnitude in absence of electric field.

	$\mu_X$	$\mu_Y$	$\mu_Z$	$ \mu $
$F=0$	-0.0228007	-0.0772935	-8.1053645	8.1057651

Table 3.1: Dipole moment components in Debye at  $F=0 \text{ V.m}^{-1}$

Figure 3.4 shows the ground state energy as a function of the electric field for the three cases of calculation.

As expected from the Stark effect, the variation of case (a) is linear with respect to the field  $\vec{F}$ , which tends to stabilise the ground state when the applied field and dipolar moment share the same orientation. In case (b) the energy follows a parabolic curve as the electric field disrupts the equilibrium geometry found at  $F = 0 \text{ V.m}^{-1}$ . The curvature is much smaller compared to the variation in case (a) and the overall behaviour in case (c) follows the electronic effects.

Figure 3.5 shows how the  $D$  parameter evolves as a function of the applied field  $F$ . In all three cases the absolute variation ( $|dD/dF|$ ) is linear, with a small negative slope in case (a) and a large positive slope in cases (b) and (c).

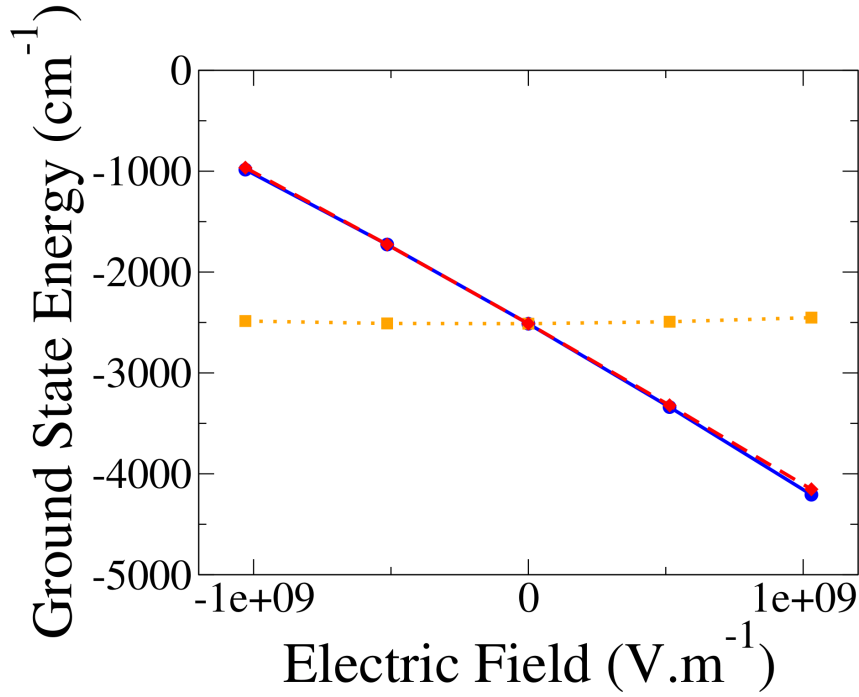


Figure 3.4: Energies in  $\text{cm}^{-1}$  (shifted by  $58.35795.107 \text{ cm}^{-1}$ ) of the ground state obtained for the cases (a) (in blue and plain line), (b) (in orange and dotted line) and (c) (in red and dashed line) as functions of the field,  $\vec{F} \parallel Z$ .

This demonstrates that the geometric effects (b) have a stronger impact on the variation of the  $D$  value than electronic effects (a) as the overall tendency of case (c) follows that of case (b). Figure 3.6 shows the evolution of the  $E$  parameter. Although some deviation is observed for the geometric case (b), mainly due to the lack of precision in calculating this specific property, the overall variation is linear with the field. However, the variation in case (b) is very small ( $< 0.05 \text{ cm}^{-1}$ ) and the behaviour of case (c) is now governed by the electronic effects with a negative absolute slope.

Table 3.2 shows the absolute slopes  $|dD/dF|$  and  $|dE/dF|$  for all three cases of calculations and their individual sums. Note that these slopes are additive with good precision for both parameters.

To rationalise these results, the most significant contributions to the D parameter  $C(D)$  were examined as detailed in Table 3.3. As mentioned previously, the main contribution comes from the first excited triplet, which is also the most affected by the field  $\vec{F}$ . While other states may have large contributions, the variation from  $-F$  to  $+F$  is minimal. Given that these contributions are

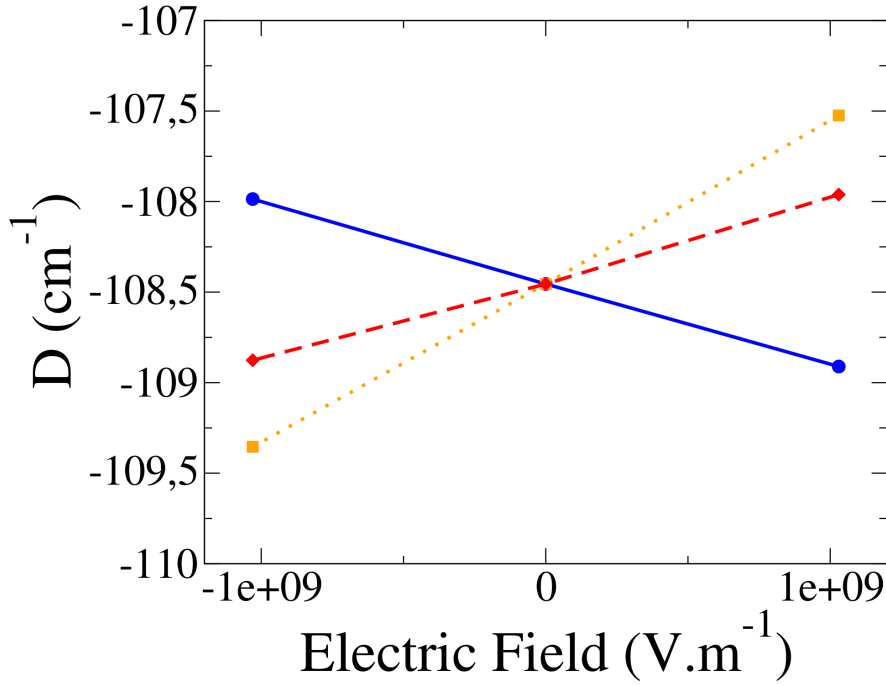


Figure 3.5: Evolution of the axial D parameter (in  $\text{cm}^{-1}$ ) as a function of the field applied in cases (a) (in blue and plain line), (b) (in orange and dotted line) and (c) (in red and dashed line),  $\vec{F} \parallel Z$

$\text{Hz}/(\text{V.m}^{-1})$	(a) Electronic structure	(b) Geometric structure	(c) Both	Sum of (a) and (b)
$dD/dF$	-13.52	+26.66	+13.15	+13.14
$dE/dF$	-2.53	-0.36	-2.88	-2.89

Table 3.2: Slopes of the straight lines in cases (a), (b) and (c) for the D and E parameter for  $\vec{F} \parallel Z$ , Fig. 3.5 and 3.6

positive (while the total D is negative) it is clear that the first excited triplet is the main source of the substantial axial D parameter and its variation in this system.

The variation of the contribution of the first excited triplet  $\Delta C(D)_{VAR}$  matches well with that provided by ORCA, indicating that the variation of the SOC, as well as the variation of the difference in energy  $\Delta(\Delta E)$ , can be used for the analysis. The perturbative estimation of this contribution yields a slightly larger value ( $-193\text{cm}^{-1}$  at  $F = 0$ ), as the two lowest states are rather close in energy ( $\approx 2166\text{cm}^{-1}$ ), which takes them outside the perturbation regime.

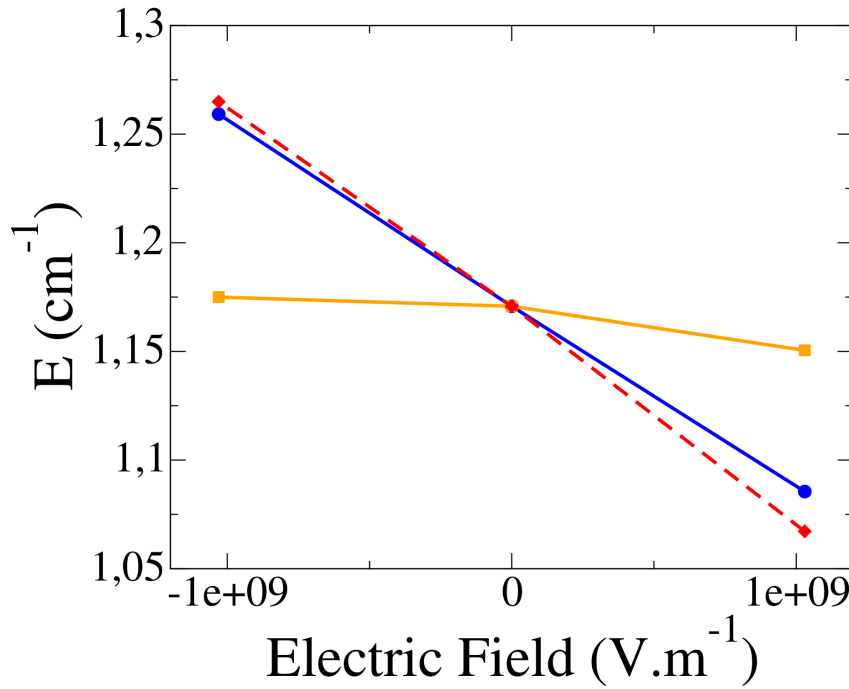


Figure 3.6: Evolution of the rhombic E parameter (in  $\text{cm}^{-1}$ ) as a function of the field applied in cases (a) (in blue and plain line), (b) (in orange and dotted line) and (c) (in red and dashed line),  $\vec{\mathbf{F}} \parallel Z$

- In case (a), the energy difference between the two lowest triplet states remains roughly the same ( $\Delta(\Delta E) = -1.6\text{cm}^{-1}$ ), so the variation of the SOC is the leading factor in the change of  $|D|$ . As the SOC increases, so does  $|D|$ .
- In case (b), the SOC decreases and the energy difference increases ( $\Delta|\text{SOC}|^2 = -210\text{cm}^{-1}$  and  $\Delta(\Delta E) = 36\text{cm}^{-1}$ ), inducing a decrease of  $|D|$  (eq. 3.2.1).
- In case (c), both the SOC and energy difference increase. Since  $D$  decreases, we can conclude that the dominant factor is the increase of the energy difference. Moreover, since case (c) and (b) have a similar trend, we can also conclude that geometrical structure effects dominate electronic ones.

This last conclusion is supported by the changes in geometry under the application of the electric field, as reported in Table 3.4, with the variation of the distances between the Ni(II) ion and its coordination sphere between  $+F$  and  $-F$ . The Ni-Cl bond length increases in a positive field  $+F$ , as this bond carries most of

	Excited state	C(D) for -F	C(D) for +F	$\Delta C(D)$ ORCA	$\Delta C(D)$ VAR.	$\Delta C(D)$ PERT.	$\Delta SOC ^2$	$\Delta(\Delta E)$
(a)	T <sub>1</sub>	-179.18	-180.06	-0.88	-0.82	-0.96	1722.78	-1.60
	T <sub>2</sub>	23.84	23.72	-0.12				
	T <sub>3</sub>	19.61	19.68	0.07				
	S <sub>3</sub>	20.48	20.57	0.09				
(b)	T <sub>1</sub>	-180.95	-178.25	2.70	2.70	3.42	-209.90	36.2
	T <sub>2</sub>	23.82	23.72	-0.10				
	T <sub>3</sub>	19.71	19.58	-0.13				
	S <sub>3</sub>	20.55	20.51	-0.04				
(c)	T <sub>1</sub>	-180.49	-178.66	1.83	1.90	2.47	1509.15	34.7
	T <sub>2</sub>	23.88	23.66	-0.22				
	T <sub>3</sub>	19.67	19.61	-0.06				
	S <sub>3</sub>	20.51	20.56	0.05				

Table 3.3: Contributions to the axial parameter D (in cm<sup>-1</sup>) of the most contributing excited states and their variations  $\Delta C(D)$  between the -F and +F in the Z direction either provided by ORCA, calculated variationally and perturbatively.  $\Delta|SOC|^2$  is the variation of the square of the module of the SOC between the ground and the first excited triplet states while  $\Delta(\Delta E)$  is the variation between the -F and +F of their energy difference (in cm<sup>-1</sup>) obtained at the NEVPT2 level.

Ligands	-F	+F	$\Delta(distance)$
Cl	2.31391	2.32709	$131.8 \cdot 10^{-4}$
N <sub>1</sub> (apical)	2.2.15016	2.14727	$-28.9 \cdot 10^{-4}$
N <sub>2</sub>	2.22739	2.22043	$-69.6 \cdot 10^{-4}$
N <sub>3</sub>	2.14628	2.14139	$-48.9 \cdot 10^{-4}$
N <sub>4</sub>	2.22688	2.22023	$-6.65 \cdot 10^{-4}$

Table 3.4: Variation of the distances in Angstrom between the Ni(II) ion and the closest atoms of the ligand between -F and +F with  $\vec{F} \parallel Z$ .

the dipole moment and is therefore expected to lengthen in order to maximise its interaction with the field. However, the others atoms tend to move closer to the Ni(II) ion, increasing the ligand field in the XY plane. This destabilises both the  $d_{x^2-y^2}$  and  $d_{xy}$  orbitals, the former, which points directly towards N<sub>3</sub> is more affected. This leads to an increase in the energy difference between these orbitals and thus between the ground and excited states. As can be seen from Tables 3.3 and 3.5, the variation of the two energy differences follows the same pattern in each case of calculation.

The rhombic term  $E$  arises from the difference between the X and Y directions. For its rationalisation, the same analysis based on the contributions provided

Variation of the orbital energy differences	(a)	(b)	(c)
$\Delta(\Delta\epsilon(d_{x^2-y^2} - d_{xy}))$	6.58	258.98	267.76

Table 3.5: Variation between  $-F$  and  $+F$  applied in the Z direction of the orbital energy difference  $\Delta(\Delta\epsilon(d_{x^2-y^2} - d_{xy}))$  in  $\text{cm}^{-1}$

by ORCA should be used. Unfortunately, these contributions cannot be used because their sum increases with the field while the  $E$  values extracted via effective Hamiltonian theory decrease as shown in Figure 3.6. Nevertheless it is possible to rationalise the  $E$  term by identifying the determinants that distinguish the X direction from the Y direction. In the case of an applied field along the Z axis, the  $d_{x^2-y^2}$ ,  $d_{xy}$  and  $d_{z^2}$  orbitals are symmetric in X and Y. As such the only determinants that treat these two directions differently are those with a single occupation in the  $d_{xz}$  or  $d_{yz}$  orbitals. There are six of these determinants with  $M_S=1$ , two of them have the largest coefficients in the wave-function of the  $T_2$  and  $T_3$  excited states, resulting from single excitation from either of these orbitals to the  $d_{x^2-y^2}$  or  $d_{z^2}$  which are singly occupied in the ground state  $T_0$ . If there is no difference between the two directions, *i.e.* no rhombicity  $E=0$ , the weights of these determinants should be the same in both states leading to two contributions that cancel each other out. To estimate the evolution of the rhombicity, one can look at the variation of these weights with respect to the field. We can define  $\Delta w(X - Y)$  which is the difference between the weight  $w(d_{xz})$  and  $w(d_{yz})$ , and its overall variation  $\Delta(\Delta w(X - Y))$  as reported in Table 3.6.

		$-F$	$-F$	$\Delta(\Delta w(X - Y))$
(a)	$w(d_{xz})$	96.200	96.741	
	$w(d_{yz})$	97.210	97.224	-0.528
	$\Delta w(X - Y)$	1.010	0.482	
(b)	$w(d_{xz})$	96.543	96.494	
	$w(d_{yz})$	97.282	97.145	0.088
	$\Delta w(X - Y)$	0.739	0.651	
(c)	$w(d_{xz})$	96.271	96.762	
	$w(d_{yz})$	97.282	97.152	-0.621
	$\Delta w(X - Y)$	1.011	0.390	

Table 3.6: Weight  $w(d_{xz})$  and  $w(d_{yz})$  of the determinants with single occupation in the respective orbitals, their difference  $\Delta w(X - Y)$  and their overall variation  $\Delta(\Delta w(X - Y))$  in all three case of calculation for  $\vec{F} \parallel Z$ .

First, we can observe the small variation in case (b) which matches well the

variation of  $E$  for this case in 3.6. The variation  $\Delta(\Delta w(X - Y))$  is very similar between case (a) and case (c), which confirms that the overall variation of the  $E$  term is dictated by the changes in the electronic structure induced by the application of the electric field.

### 3.2.3 Application of the electric field along the Y axis

Now, let us consider the applied field in the Y direction  $\vec{F} \parallel Y$ . The field is now perpendicular to the main component of the dipole moment ( $\mu_Z$ ). Note that the field is not applied directly along the Ni-N<sub>3</sub> bond, which is slightly out of the XY plane, but rather along the Y axis which is perpendicular to the Z axis. Figure 3.7 shows the evolution of the ground state energy when  $F \parallel Y$ . Case (b) follows the same parabolic trend as when  $F \parallel Z$ , the argument remains the same. The situation differs from that of  $\vec{F} \parallel Z$  in case (a), the evolution is now quadradic rather than linear. The applied field induces a change in the sign of the dipole moment component  $\mu_y$  which is very small, see Table 3.1. The Stark effect then acts to stabilise the ground state for both signs of the electric field  $F$ .

Figure 3.8 shows the evolution of the  $D$  term with respect to the applied field. It once again follows a linear behavior in all three cases. The sign of the slopes are now inverted, with  $|dD/dF|$  being positive for case (a) and negative for cases (b) and (c) as opposed to when the field was along the Z direction.

The slopes for each case are shown in Table 3.7, once again the variation of the  $D$  term is dictated by the geometrical changes under the applied field, case (b). Note that the slopes  $|dD/dF|$  remain additive and are now much higher in the  $\vec{F} \parallel Y$  case than in the  $\vec{F} \parallel Z$  case, almost seven times larger.

$Hz/(V.m^{-1})$	(a) Electronic structure	(b) Geometric structure	(c) Both	Sum of (a) and (b)
$dD/dF$	+25.32	-110.75	-85.45	-85.43
$dE/dF$	-2.39	+1.20	-1.19	-1.19

Table 3.7: Slopes of the straight lines in cases (a), (b) and (c) for the D and E parameter for  $\vec{F} \parallel Y$

The most significant contributions are reported in Table 3.8. Once again, the contribution that is the most affected by the electric field is that of the first excited state  $T^1$  with good agreement between the ORCA and the variational/perturbative estimations. In case (a), note the increase in the energy difference  $\Delta(\Delta E)$ . This can be attributed to the deformation of the electronic cloud around the Ni(II) ion

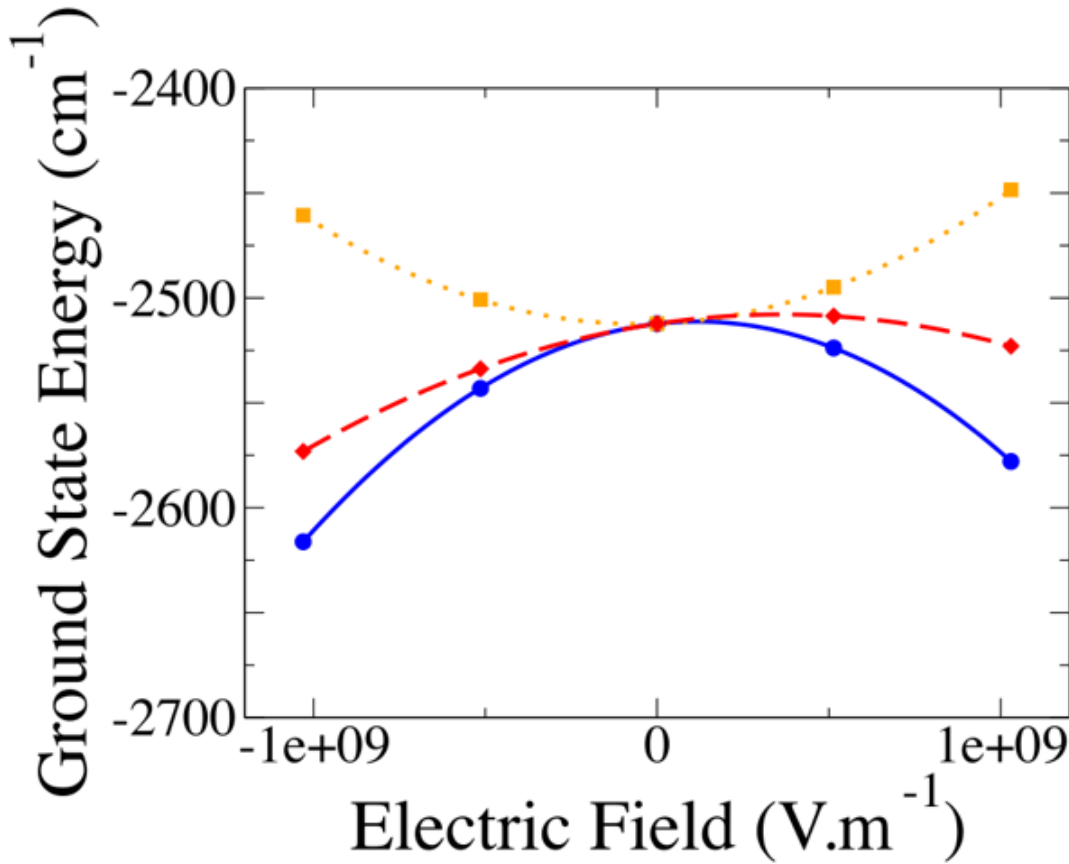


Figure 3.7: Energies in  $\text{cm}^{-1}$  (shifted by  $58.35795.107 \text{ cm}^{-1}$ ) of the ground state obtained for the cases (a) (in blue and plain line), (b) (in orange and dotted line) and (c) (in red and dashed line) as functions of the field applied in the Y direction.

in the direction of  $\text{N}_3$  for  $+F$ . This destabilises the  $d_{x^2-y^2}$  orbital, which points directly towards  $\text{N}_3$  and stabilizes the  $d_{xy}$  orbital, resulting in an increase in the energy difference between the two states. The rationalization of the variations for case (b) can be explained by the evolution of the ligand field shown in Table 3.9. The application of the electric field along the Y direction tends to elongate the  $\text{Ni-N}_3$  bond and concomitantly reduces the other  $\text{Ni-N}$  bond lengths in the XY plane. The ligand field along the Y axis is therefore reduced stabilising the  $d_{x^2-y^2}$  orbital while the  $d_{xy}$  orbital, which points directly towards  $\text{N}_2$  and  $\text{N}_4$ , is destabilised. This results in a decrease in the orbital energy difference  $\Delta(\Delta\epsilon(d_{x^2-y^2} - d_{xy}))$ , thus decreasing the energy difference between the ground state  $T^0$  and the excited state  $T^1$ . According to eq 3.2.1, this leads to an increase in the magnitude  $|D|$ , as can be seen in Figure 3.8 for case (b). Note that the

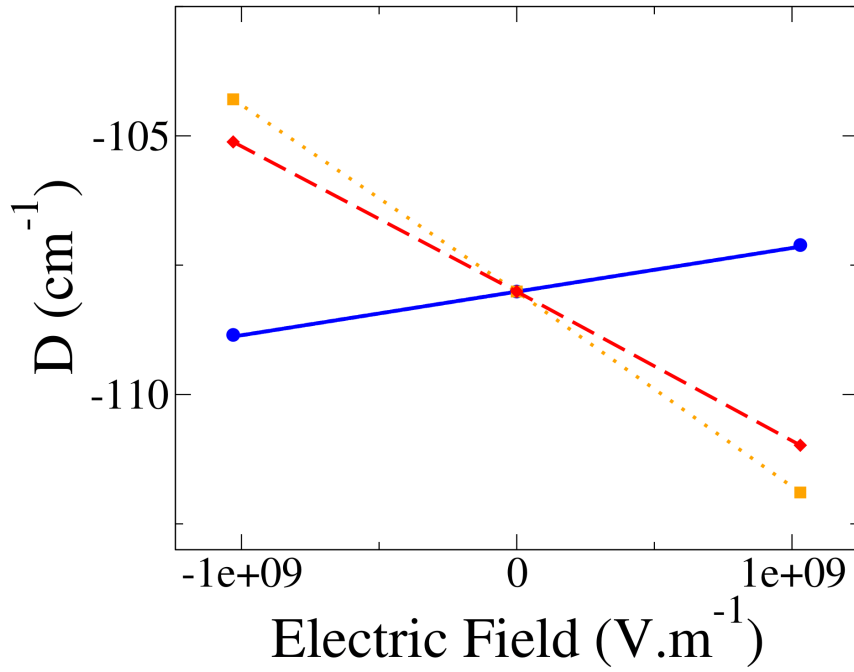


Figure 3.8: Evolution of the axial D parameter (in  $\text{cm}^{-1}$ ) as a function of the field  $\vec{\mathbf{F}} \parallel Y$  in cases (a) (in blue and plain line), (b) (in orange and dotted line) and (c) (in red and dashed line)

impact of the electric field on the geometric structure results in the greatest change of magnitude  $|D|$  with a slope as large as  $-110.75\text{Hz}/(\text{V}\cdot\text{m}^{-1})$ . This is due to the large variation in the energy difference  $\Delta(\Delta E)$  for case (b) which is one order of magnitude greater than when the field is along the Z axis. Similarly to the  $\vec{\mathbf{F}} \parallel Z$  case, the overall trend in the evolution of the axial anisotropy  $D$  is driven by the field's impact on the geometric structure.

As for the rhombicity, changes in the electronic structure caused by the application of an electric field are once again responsible for the overall variation as indicated by Table 3.7. These variations are linear with good additivity but are smaller than observed when  $\vec{\mathbf{F}} \parallel Z$ . Figure 3.9 shows that the rhombic  $E$  decreases as the field increases, indicating that the difference between the X and Y axes diminishes. This can be explained by the evolution of the weights  $w(d_{xz})$  and  $w(d_{yz})$  of determinants with a single occupation in the  $d_{xz}$  and  $d_{yz}$  orbitals, which are found in Table 3.10. In case (a) and (c), the diffence  $\Delta(X - Y)$  of the weights between X and Y decreases with the field, which reduces the rhombicity term  $E$ . Note that  $\Delta(X - Y)$  is positive in case (b) which is consistent with the

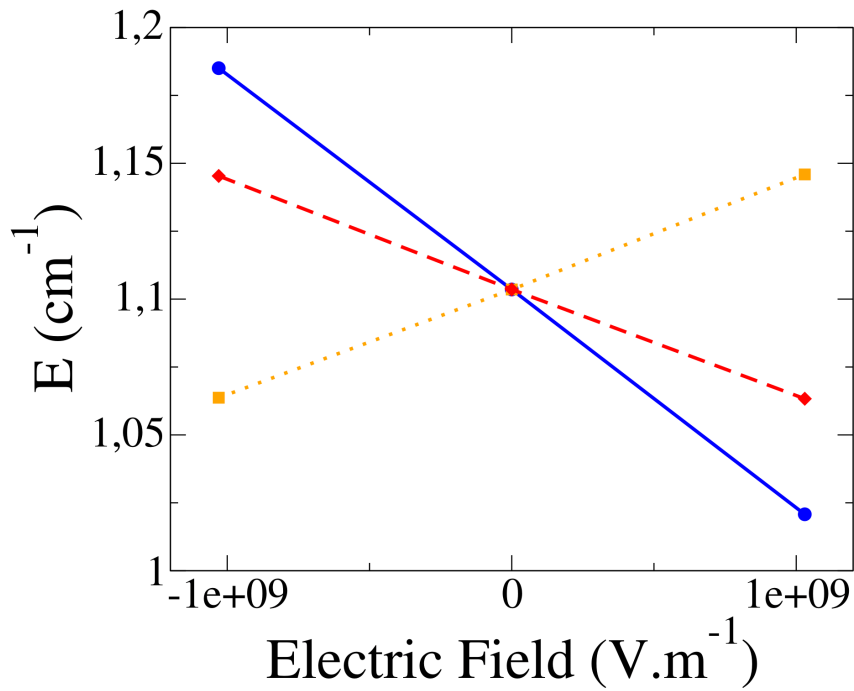


Figure 3.9: Evolution of the rhombic E parameter (in  $\text{cm}^{-1}$ ) as a function of the field  $\vec{\mathbf{F}} \parallel Y$  in cases (a) (in blue and plain line), (b) (in orange and dotted line) and (c) (in red and dashed line)

positive slope observed for geometric structure changes in Table 3.7 and Figure 3.9.

	Excited state	C(D) for -F	C(D) for +F	$\Delta C(D)$ ORCA	$\Delta C(D)$ VAR.	$\Delta C(D)$ PERT.	$\Delta SOC ^2$	$\Delta(\Delta E)$
(a)	T <sub>1</sub>	-179.99	-178.26	1.73	1.74	2.21	36.05	24.40
	T <sub>2</sub>	23.66	24.05	0.39				
	T <sub>3</sub>	19.60	19.61	0.01				
	S <sub>3</sub>	20.53	20.50	-0.03				
(b)	T <sub>1</sub>	-174.84	-183.67	-8.83	-8.76	-11.10	-162.22	-122.40
	T <sub>2</sub>	23.91	23.82	-0.09				
	T <sub>3</sub>	19.56	19.65	0.09				
	S <sub>3</sub>	20.44	20.60	0.16				
(c)	T <sub>1</sub>	-175.65	-182.86	-7.11	-7.02	-8.91	-124.89	-98.20
	T <sub>2</sub>	23.71	24.02	0.31				
	T <sub>3</sub>	19.56	19.65	0.09				
	S <sub>3</sub>	20.45	20.59	0.14				

Table 3.8: Contributions to the axial parameter D (in cm<sup>-1</sup>) of the most contributing excited states and their variations  $\Delta C(D)$  between the -F and +F in the Y direction either provided by ORCA, calculated variationally and perturbatively.  $\Delta|SOC|^2$  is the variation of the square of the module of the SOC between the ground and the first excited triplet states while  $\Delta(\Delta E)$  is the variation between the -F and +F of their energy difference (in cm<sup>-1</sup>) obtained at the NEVPT2 level.

Ligands	-F	+F	$\Delta(distance)$
Cl	2.32024	2.32043	$2.4.10^{-4}$
N <sub>1</sub> (apical)	2.14947	2.14727	$1.7.10^{-4}$
N <sub>2</sub>	2.22518	2.22245	$-27.3.10^{-4}$
N <sub>3</sub>	2.1482	2.14596	$11.4.10^{-4}$
N <sub>4</sub>	2.2270	2.22229	$-4.1.10^{-4}$

Table 3.9: Variation of the distances in Angstrom between the Ni(II) ion and the closest atoms of the ligand between -F and +F with  $\vec{F} \parallel Y$ .

### 3.2.4 Conclusion

The aim of this study was to determine the influence of an external electric field on the anisotropy parameter of the ZFS Hamiltonian in a Ni(II) complex close to first-order spin-orbit coupling regime. A combination of DFT and wave-function theory was employed to evaluate the geometric changes induced by the field and extract the parameter using wave-function based method and effective Hamiltonian theory. Treating the electronic and geometric changes separately allowed us to identify which mechanisms are responsible for the variation in the parameters. Two orientations for the field were explored. Depending on which parameter it affected the most, both orientations proved to be of interest. The

		$-F$	$-F$	$\Delta(\Delta w(X - Y))$
(a)	$w(d_{xz})$	96.603	96.738	
	$w(d_{yz})$	97.191	97.152	-0.174
	$\Delta w(X - Y)$	0.588	0.414	
(b)	$w(d_{xz})$	96.661	96.695	
	$w(d_{yz})$	97.159	97.195	+0.002
	$\Delta w(X - Y)$	0.498	0.500	
(c)	$w(d_{xz})$	96.597	96.762	
	$w(d_{yz})$	97.175	97.170	-0.170
	$\Delta w(X - Y)$	0.578	0.480	

Table 3.10: Weight  $w(d_{xz})$  and  $w(d_{yz})$  of the determinants with single occupation in the respective orbitals, their difference  $\Delta w(X - Y)$  and their overall variation  $\Delta(\Delta w(X - Y))$  in all three case of calculation for  $\vec{F} \parallel Y$ .

findings can be summarised in a few points:

- (i) The rhombicity of the system, described by the rhombic term  $E$ , can be modulated by the electric field. The variation  $dE/dF$  can be significant, especially for  $\vec{F} \parallel Z$  which was not expected at first. As rhombicity describes the anisotropy between the X and Y directions, it seems reasonable to assume that it would be more affected by the field oriented in the XY plane rather than in the Z direction. However, the most important contributions to the  $E$  term were found to come from excited states ( $T^2$  and  $T^3$ ) coupled to the ground state via excitations from the  $d_{xz}$  or the  $d_{yz}$  orbitals to the  $d_{z^2}$  or the  $d_{x^2-y^2}$  orbitals. As these orbitals are mainly oriented along the Z axis, it is therefore natural that these excitations would be more impacted by the field along the Z directions than in the XY plane.
- (ii) The electronic and geometric changes have an opposite effect on the variation  $dD/dF$  for both field orientation. In case (a) for  $\vec{F} \parallel Z$ , the large increase in magnitude  $|D|$  can be related to a large variation of the SOC while the energy difference  $\Delta E$  between  $T^0$  and  $T^1$  decreases. When  $\vec{F} \parallel Y$ , the variations are governed only the difference in energy  $\Delta E$  between the two lowest triplet. In case(a), the electronic cloud displacement induced by the electric field tend to stabilise the  $d_{xy}$  orbital and destabilise the  $d_{x^2-y^2}$  orbital leading to an increase of  $\Delta E$
- (iii) Similarly to rhombicity, it was expected that the greatest change to the axial parameter  $D$  would come from the application of the electric field in

the Z direction. However, as the changes in  $D$  are dictated by the behaviour of the two orbitals that belong to the XoY plane,  $d_{x^2-y^2}$  and  $d_{xy}$ , the most impressive impact comes from the field along the Z direction.

# Chapter 4

## Electric field on Exchange anisotropy

Numerous studies have been conducted to characterise the properties of magnetic anisotropies and many successful procedures have been developed with great success as discussed above. However, only a few studies have been applied to determine the properties of the exchange anisotropy using Quantum Chemistry theories. This study is part of a series of works that aims to rationalise the origin of exchange anisotropy in polynuclear molecules.

The spin Hamiltonian used to describe anisotropic behaviour in binuclear systems is as follows:

$$\hat{H}_{AB} = J_{AB} \hat{\mathbf{S}}_A \cdot \hat{\mathbf{S}}_B + \hat{\mathbf{S}}_A \cdot \overline{\overline{D}}_{AB} \cdot \hat{\mathbf{S}}_B + \mathbf{d}_{AB} \cdot (\hat{\mathbf{S}}_A \times \hat{\mathbf{S}}_B) \quad (4.0.1)$$

To achieve this, a procedure was developed for extracting values of the Dzyaloshinskii-Moriya pseudovector interaction  $d_{AB}$  and the symmetric exchange anisotropy  $D_{ij}$ -tensor. It relies on effective Hamiltonian theory in combination with wave-function based method. This procedure was tested on a simple model molecule, shown in Figure 4.1, consisting of two  $Cu^{2+}$  cations separated by  $Cl^-$  anions.

The reason for choosing this system is its simplicity, with only one magnetic electron per centre and a reasonable size, it allows for simple analytical derivation and high-level treatment of the correlation. Such a toy molecule can also be distorted to assess the impact of geometry, *i.e.* distances and angles, on these interactions. Initially, it was determined that the most favourable setting for obtaining large values of the anisotropic interactions is to approach first-order coupling regime without reaching it. It was discussed in the previous chapter that such regime occurs when degeneracy of some of the d-orbitals allows for very strong couplings between the ground and excited states. This situation arises

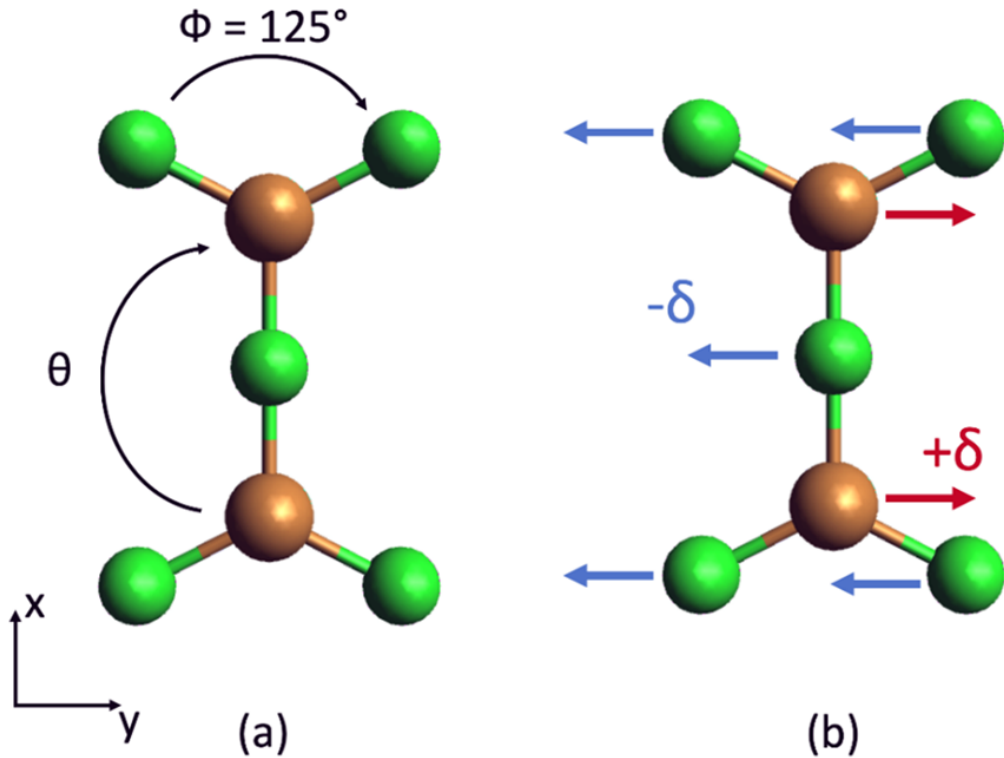


Figure 4.1: (a)  $Cu_2Cl_5$  model molecule of  $D_{2h}$  symmetry, (b) displacement  $\delta$  of the atoms generated by the application of an electric field along the  $y$  direction.

when the outside angle  $\phi$  reaches  $120^\circ$ , at which point the local environment of each  $Cu^{2+}$  is close to a  $C_3$ -axis symmetry. This allows the condition of quasi-degeneracy of the  $d_{x^2-y^2}$  and  $d_{xy}$  orbitals to be achieved. However, due to the  $D_{2h}$  symmetry of the system, it possesses an inversion centre, leading to a zero value of DMI. To induce a non-zero value of the DMI, the first two studies relied on the deformation of the molecule with a variation of the  $\theta$  angle, which resulted in the hybridization of the otherwise pure cartesian d-orbitals. This mixing of the d-orbitals is key to creating DMI, as increasing the mixing was shown to allow the obtention of very large values of DMI. It was then thought that applying of an external electric field could have a similar effect by acting on the electronic could itself rather than the nuclei's position. As mentionned in the previous chapter, an electric field is an interesting option as it can be focused accurately at the molecular level. Using an external stimulus is also much easier than relying on the "intrinsic" geometry of the molecule and allows a larger number of candidates to be studied. This study focused on the impact of the electric field on the isotropic and antisymmetric exchange parameter of the spin Hamiltonian, it establishes that the Dzyaloshinskii-Moriya pseudo-vector

is highly sensitive to the external field. Here we follow the already established procedure to focus our attention on the symmetric exchange anisotropy tensor. The work proceeds along two axes:

- (i) Derive an appropriate model to estimate the symmetric tensor under the condition of 1<sup>st</sup> order SOC in the absence of an electric field.
- (ii) Study how the symmetric tensor varies under the influence of an electric field, and its relation to the apparition of DMI.

## 4.1 Computational Informations

The electronic and relativistic state computation were performed using the MOLCAS code. Complete-Active-Space-Self-Consistent field calculations were carried out for various values of the angle  $\Phi$ , ranging from  $\Phi = 130^\circ$  (close to 1<sup>st</sup> order SOC) to  $170^\circ$  (far from it). The active space consists of six electrons occupying the  $d_{x^2-y^2}$  and  $d_{xy}$  orbitals of each copper centre, CAS(6,4), with two sets of orbitals optimised in an average way. One for the four lowest triplet states and the other for the four lowest singlet states. An enlarged active space containing all d-orbitals and their electrons, CAS(18,10) was also considered, but a previous study showed that it had little impact on the extracted parameters. The conclusion was that the reduced active space CAS(6,4) was sufficient to capture the effect of first-order SOC. Nevertheless, it used for the treatment of second-order spin orbit coupling. Dynamical correlation was introduced using the Difference-dedicated-configuration-interaction (DDCI3) method, performed using the CASDI code which is interfaced with the MOLCAS chain. Three types of SO-SI calculation were performed:

- (i) CAS(6,4)SCF : the energy and wave-function are obtained from CASSCF calculation.
- (ii) CAS(6,4)DDCI/SCF-SO : the DDCI energies are used while the wave-functions remain that of the CAS(6,4)SCF.
- (iii) CAS(6,4)DDCI/DDCI-SO : the energies and wave-functions are obtained from DDCI calculation.

This allows to study the impact of each component of dynamic correlation (energy or wave-function) on the exchange interactions. The TZVP basis set

were used throughout all calculations: 5s4p3d1p for Cu and 4s3p1d for Cl. The continuous electric field was added in the SEWARD stage of the calculation in MOLCAS, the X,Y and Z directions were treated but most of the results reported here relates to the Y direction. The field values range from 0  $kV.cm^{-1}$  to  $5.1724 \times 10^4 kV.cm^{-1}$  for the maximum value.

## 4.2 Theoretical model

In order to derive the parameters of the Multispin Hamiltonian, we must first define the model space. Let  $a(a')$  and  $b(b')$  represent the magnetic orbitals located on each copper ion. These orbitals are obtained from state-specific calculations and may differ between triplet and singlet states by the tails on the  $Cl^-$  ligands hence the difference of notation. Crystal field theory indicates that these orbitals should mainly be composed of the  $d_{x^2-y^2}$  or  $d_{xy}$  orbitals respectively. With the application of an electric field, one can predict that these orbitals will hybridise to form the orbitals  $a(a')$  and  $b(b')$ . We refer to the orthogonal cartesians orbitals as  $a_1(b_1)$  and  $a_2(b_2)$  respectively depending whether the site is A or B so that:

$$\begin{aligned} a &= \alpha a_1 + \beta a_2 & b &= -\alpha b_1 + \beta b_2 \\ a' &= \alpha' a_1 + \beta' a_2 & b' &= -\alpha' b_1 + \beta b_2 \end{aligned} \quad (4.2.1)$$

Where  $\alpha(\alpha')$  and  $\beta(\beta')$  are the mixing coefficients between the d-orbital in the triplet(singlet) state. The coupling of the lone electron of each copper ion gives rise to a triplet and singlet state that will form the basis of the model space:

$$\begin{aligned} T^+ &= |ab| \\ T^0 &= \frac{1}{\sqrt{2}}(|a\bar{b}| - |b\bar{a}|) \\ T^- &= |\bar{a}\bar{b}| \\ S &= \frac{1}{\sqrt{2}}(|a'\bar{b}'| + |b'\bar{a}'|) \end{aligned} \quad (4.2.2)$$

The matrix representation of the Multi-Spin Hamiltonian in this basis is:

$H_{MS}$	$T^+$	$T^0$	$T^-$	$S$
$T^+$	$\frac{J_{AB}}{4} + \frac{D_{zz}}{4}$	$\frac{D_{xz}-iD_{yz}}{2\sqrt{2}}$	$\frac{(D_{xx}-D_{zz}-2iD_{xy})}{4}$	$\frac{d_y+id_x}{2\sqrt{2}}$
$T^0$	$\frac{D_{xz}+iD_{yz}}{2\sqrt{2}}$	$\frac{J_{AB}}{4} - \frac{D_{zz}}{4} + \frac{(D_{xx}+D_{yy})}{4}$	$-\frac{D_{xz}-iD_{yz}}{2\sqrt{2}}$	$-\frac{id_z}{2}$
$T^-$	$\frac{(D_{xx}-D_{zz}+2iD_{xy})}{4}$	$-\frac{D_{xz}+iD_{yz}}{2\sqrt{2}}$	$\frac{J_{AB}}{4} + \frac{D_{zz}}{4}$	$\frac{d_y-id_x}{2\sqrt{2}}$
$S$	$\frac{d_y-id_x}{2\sqrt{2}}$	$\frac{id_z}{2}$	$\frac{d_y+id_x}{2\sqrt{2}}$	$-\frac{3J_{AB}}{4} - \frac{D_{zz}}{4} - \frac{(D_{xx}+D_{yy})}{4}$

The evolution of the  $J_{AB}$  and the components  $d_x$ ,  $d_y$  and  $d_z$  under the application of an external electric field has been studied previously. The components  $D_{xx}$ ,  $D_{xy}$ , etc. are the components of the symmetric exchange anisotropy  $\overline{\overline{D}}$ -tensor which is the focus of this study. Its evolution will be compared to previous results, especially those relating to the DMI.

When approaching the condition of quasi-degeneracy of the  $d_{x^2-y^2}$  and  $d_{xy}$  orbitals, *i.e.* first-order spin orbit coupling, second-order perturbation theory cannot be used to account for spin-orbit coupling due to the small differences in energy between the lowest states. Therefore, a variational treatment is mandatory. To this end, a model was derived to assess the contribution of 1<sup>st</sup> order SOC based on the spin-free states generated by the occupation of these two orbitals. The following states form the uncoupled basis:

$$\begin{aligned}
T_1^+ &= |a_1 b_1|; & T_1^0 &= \frac{|a_1 \bar{b}_1| - |b_1 \bar{a}_1|}{\sqrt{2}} \\
S_1 &= \frac{|a_1 \bar{b}_1| - |b_1 \bar{a}_1|}{\sqrt{2}} \\
T_2^+ &= \frac{|a_1 b_2| + |b_1 a_2|}{\sqrt{2}}; & T_2^0 &= \frac{|a_1 \bar{b}_2| + |b_1 \bar{a}_2| - |a_2 \bar{b}_1| - |b_2 \bar{a}_1|}{2} \\
S_2 &= \frac{|a_1 \bar{b}_2| + |b_1 \bar{a}_2| + |a_2 \bar{b}_1| + |b_2 \bar{a}_1|}{2} \\
T_3^+ &= \frac{-|a_1 b_2| + |b_1 a_2|}{\sqrt{2}}; & T_3^0 &= \frac{-|a_1 \bar{b}_2| + |b_1 \bar{a}_2| - |a_2 \bar{b}_1| + |b_2 \bar{a}_1|}{2} \\
S_3 &= \frac{-|a_1 \bar{b}_2| + |b_1 \bar{a}_2| + |a_2 \bar{b}_1| - |b_2 \bar{a}_1|}{2} \\
T_4^+ &= |a_2 b_2|; & T_4^0 &= \frac{|a_2 \bar{b}_2| - |b_2 \bar{a}_2|}{\sqrt{2}} \\
S_4 &= \frac{|a_2 \bar{b}_2| - |b_2 \bar{a}_2|}{\sqrt{2}}
\end{aligned} \tag{4.2.3}$$

For simplicity, the ionic part of these states was left out of the model, but will be taken into account in the *ab initio* calculations as they play an essential part in the antiferromagnetic coupling. Note that, in absence of electric field, crystal field theory indicates that the magnetic orbitals are the  $d_{x^2-y^2}$  on each copper center. Thus the energy ordering should follow the order in which they are expressed in 4.2.3. The spin-orbit matrix can be derived from the SO-Hamiltonian:

$$\hat{H}^{SO} = \zeta (\hat{l}_1 \hat{s}_1 + \hat{l}_2 \hat{s}_2) \tag{4.2.4}$$

With  $\hat{l}_i$  the angular momenta and  $\hat{s}_i$  the spin momenta operators working on electron  $i$  and  $\zeta$  the spin-orbit constant. The spin-orbit couplings between the states 4.2.3 originate from the  $\hat{l}_z \hat{s}_z$  part of the  $\hat{H}^{SO}$  that couples the determinants formed from orbitals of same spatial ( $m_l$ ) and spin ( $m_s$ ) component. The representation matrix of the SO Hamiltonian with the addition of electronic couplings is given in the basis developped in eq 4.2.3.

The electronic effects included are the isotropic couplings  $J_i$ , between triplet and singlet states of the same spatial nature. The  $h_i(h_i')$  couplings are induced

$\hat{H}^{SO}$	$ T_1^+\rangle$	$ T_2^+\rangle$	$ T_3^+\rangle$	$ T_4^+\rangle$	$ T_1^0\rangle$	$ T_2^0\rangle$	$ T_4^0\rangle$	$ S_1\rangle$	$ S_3\rangle$	$ S_4\rangle$
$\langle T_1^+  $	$E_1 + J_1$	$h_1$	$i\zeta\sqrt{2}$	$\delta_4$	0	0	0	0	0	0
$\langle T_2^+  $	$h_1$	$E_2 + J_2$	0	$h_2$	0	0	0	0	0	0
$\langle T_3^+  $	$-i\zeta\sqrt{2}$	0	$E_3 + J_3$	$i\zeta\sqrt{2}$	0	0	0	0	0	0
$\langle T_4^+  $	$\delta_4$	$h_2$	$-i\zeta\sqrt{2}$	$E_4 + J_4$	0	0	0	0	0	0
$\langle T_1^0  $	0	0	0	0	$E_1 + J_1$	$h_1$	$\delta_4$	0	$-i\zeta\sqrt{2}$	0
$\langle T_2^0  $	0	0	0	0	$h_1$	$E_2 + J_2$	$h_2$	$-i\zeta\sqrt{2}$	0	$-i\zeta\sqrt{2}$
$\langle T_4^0  $	0	0	0	0	$\delta_4$	$h_2$	$E_4 + J_4$	0	$-i\zeta\sqrt{2}$	0
$\langle S_1  $	0	0	0	0	0	$i\zeta\sqrt{2}$	0	$E_1$	$h'_1$	$\delta'_4$
$\langle S_3  $	0	0	0	0	$i\zeta\sqrt{2}$	0	$i\zeta\sqrt{2}$	$h'_1$	$E_3$	$h'_2$
$\langle S_4  $	0	0	0	0	0	$i\zeta\sqrt{2}$	0	$\delta'_4$	$h'_2$	$E_4$

Table 4.1: Representation matrix of  $\hat{H}^{SO}$  and electronic couplings in the uncoupled basis.  $T_3^0$  and  $S_2$  are not coupled to the others, as such they were left out for clarity.  $h_1(h'_1)$  and  $h_2(h'_2)$  are couplings induced by the electric field and differ between triplet and singlet states by their exchange integrals.  $\delta_1$  and  $\delta_2$  are small bielectronic integrals between  $T_1(S_1)$  and  $T_4(S_4)$ . The  $M_S=-1$  components of the triplets are left out but possess the same couplings as the  $M_S=1$  components.

by the mixing of the the  $d_{x^2-y^2}$  and  $d_{xy}$  orbitals when the electric field is applied along the Y direction. This coupling gives rise to the DMI in this system, as it opens coupling path between  $S_1$  and  $T_1^0$ . The couplings can be estimated perturbatively at second-order, but as the system enters 1<sup>st</sup> order SOC the best approach is to diagonalise the matrix following a variational treatment. Symmetric anisotropic exchange is described by a tensor of rank-two with six different components in a random set of axis. When expressed in its proper axis, it is reduced to simply two components, an axial parameter  $D_{AB}$  and rhombic term  $E_{AB}$ . In order to understand the origins of the anisotropic parameter,  $D_{AB}$  and the DMI, the couplings must be decomposed according to their contributions. Put simply, the axial anisotropy describes the difference in energy between the  $M_S=\pm 1$  and the  $M_S=0$  components. Within this model space, there is no difference in the couplings between the two  $M_S=\pm 1$  components of this matrix. As such there is no rhombicity, when considering only first-order SOC. Hence to estimate the  $D_{AB}$ , one has to look for states coupled to either  $T_1^0$  or  $T_1^+$ . The  $T_1^+$  component is coupled via SOC to  $T_3^+$  which stabilises it, bringing a negative contribution to the  $D_{AB}$  by reducing the energy of the  $M_S=\pm 1$  component. On the other hand, the  $S_3$  which is coupled to  $T_1^0$  will contribute positively to the  $D_{AB}$ . One way to assess these contributions is by diagonalising the matrix with only the relevant couplings,  $T_3^+$

or  $S_3$ , and see how the energies of  $T_1^+$  or  $T_1^0$  are affected. The small bielectronic integrals  $\delta_4$  and  $\delta'_4$  also allow the contribution of  $T_4^+$  and  $S_4$  but with a much smaller impact.

In the presence of an electric field applied in the Y direction, the situation of Table 4.1, the  $h_i$  and  $h'_i$  electronic coupling are no longer zero and new pathways open up for the DMI. As shown in matrix ??, the  $d_z$  component is created by the coupling between the  $T_1^0$  and the  $S_1$  states which can be expressed using second-order perturbation theory:

$$\frac{id_z}{2} = \langle S | H^{SO} | T^0 \rangle^{(0)} = \frac{\langle S_1 | H^{SO} | T_2^0 \rangle \langle T_2^0 | H^{el} | T_1^0 \rangle}{E_2 + J_2 - E_1} + \frac{\langle S_1 | H^{el} | S_3 \rangle \langle S_3 | H^{SO} | T_1^0 \rangle}{E_3 - E_1} \quad (4.2.5)$$

This equation is only valid far from first-order SOC regime but helps visualising how the DMI appears due to a combination of electronic and spin-orbit couplings.

For a full extraction, one must also consider the effect of higher lying states formed from determinants with the  $d_{xz}$  or  $d_{yz}$  orbitals, noted as  $a_3(b_3)$  and  $a_4(b_4)$ , singly occupied.

$$\begin{aligned} T_5^+ &= \frac{-|a_1b_3| + |b_1a_3|}{\sqrt{2}} & T_5^0 &= \frac{-|a_1\bar{b}_3| + |b_1\bar{a}_3| - |a_3\bar{b}_1| + |b_3\bar{a}_1|}{2} \\ S_5 &= \frac{-|a_1\bar{b}_4| + |b_1\bar{a}_3| + |a_3\bar{b}_1| - |b_3\bar{a}_1|}{2} \\ T_6^+ &= \frac{-|a_1b_4| + |b_1a_4|}{\sqrt{2}} & T_6^0 &= \frac{-|a_1\bar{b}_4| + |b_1\bar{a}_4| - |a_4\bar{b}_1| + |b_4\bar{a}_1|}{2} \\ S_6 &= \frac{-|a_1\bar{b}_4| + |b_1\bar{a}_4| + |a_4\bar{b}_1| - |b_4\bar{a}_1|}{2} \end{aligned} \quad (4.2.6)$$

These states are coupled with  $T_1$  and  $S_1$  through the  $\hat{l}_+ \hat{s}_- + \hat{l}_- \hat{s}_+$  operator in  $\hat{H}^{SO}$ . Note that the determinants formed from the  $d_{z^2}$  orbital can be omitted because it cannot interact with either  $T_1$  or  $S_1$  via  $\hat{H}^{SO}$ . Taking these states into account enable differentiation the two  $M_S = \pm 1$  of the triplet state and introduce rhombicity.

### 4.3 Impact of First-Order Spin-Orbit Coupling in the absence of electric field

Expressions for these terms have already been derived using second-order perturbation theory and involve the  $T_5(S_5)$  and  $T_6(S_6)$  states:

$$\begin{aligned} D_{AB} &= 4 \frac{\zeta^2 J_3}{\Delta E_3^2} - \frac{1}{2} \left( \frac{\zeta^2 J_5}{\Delta E_5^2} + \frac{\zeta^2 J_6}{\Delta E_6^2} \right) \\ E_{AB} &= \frac{1}{2} \left( \frac{\zeta^2 J_5}{\Delta E_5^2} - \frac{\zeta^2 J_6}{\Delta E_6^2} \right) \end{aligned} \quad (4.3.1)$$

where  $\Delta E_i^2 = \sqrt{\Delta T_i \Delta S_i}$  is the geometric mean of excitation energies between the states  $T_1$  and  $T_i$  or  $S_i$  and  $J_i = E_{T_i} - E_{S_i}$  is the isotropic coupling between excited states. As the first term of  $D_{AB}$  in eq 4.3.1 involves a state that contributes to 1<sup>st</sup> order SOC, its estimation may deteriorate as  $\phi$  decreases, *i.e.* entering first-order regime. This renders the equations valid only far from first-order regime and in the absence of external field. Note that the rhombic term requires the inclusion of the higher states for it to be different from zero.

Performing a rigorous extraction of the anisotropic parameter would require including all the excited states generated from single excitations within the d-orbital space, *i.e.* CAS(18,10). As this work focus solely on the contribution of 1<sup>st</sup> order SOC, a CAS(6,4) is sufficient. To assess the impact of dynamical correlation on the  $D_{AB}$  parameter, calculations were performed with gradual inclusion of the DDCI3 components (energy and wave-function). These results are reported on Figure 4.2 with the angle  $\phi$  variating from 130° to 170°.

This shows that the magnitude  $|D_{AB}|$  increases when entering 1<sup>st</sup> order SOC, *i.e.* a decrease of the angle  $\phi$ . A similar observation has been made for the DMI in previous study and in mononuclear complexes for local ZFS parameter  $D$ . It is important to note that far from first-order SOC, the impact of electron correlation is minimal, with only slight variations between the three curves. This difference increases as the angle  $\phi$  decreases. It should be noted that the curves (ii) and (iii), which differ in terms of the wave-function used (CASSCF-SO or DDCI-SO) are very similar and that the inclusion of the DDCI wave-function does not improve the results much unlike what was observed with the DMI. Therefore, the use of the correlated DDCI wave-functions in addition to the DDCI energies is not required and CASSCF wave-function should suffice for the SO-SI calculation in the absence of DMI.

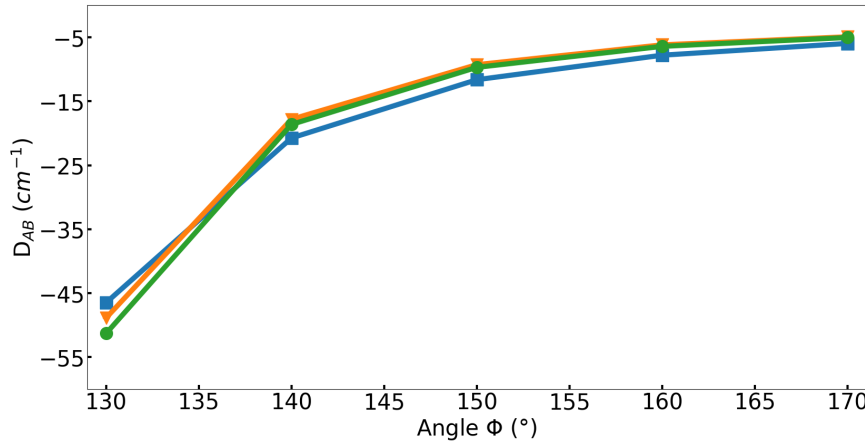


Figure 4.2:  $D_{AB}$  as a function of the outside angle  $\phi$  for (i) CAS(6,4)SCF/SCF-SO level (blue line with squares), (ii) CAS(6,4)DDCI/SCF-SO level (orange line with triangles), and (iii) CAS(6,4)DDCI/DDCI-SO level (green line with circles)

Far from first-order SOC limit, the equation 4.3.1 can be used with the large active space CAS(18,10) taking into account the states 4.2.6. At  $\phi = 170^\circ$ , the perturbative expressions give  $D_{AB}^{pert} = -4.86\text{cm}^{-1}$  and  $E_{AB}^{pert} = 0.18\text{cm}^{-1}$ , which is a good estimate when compared to the value extracted from the CAS(18,10)DDCI/DDCI-SO and effective Hamiltonian theory  $D_{AB} = -4.09\text{cm}^{-1}$  and  $E_{AB} = 0.10\text{cm}^{-1}$ . The slight overestimation may be due to the fact that a unique  $\zeta = 830\text{cm}^{-1}$  value of the free ion  $Cu^{2+}$  was used, in a complex this value is bound to decrease. As expected, these expressions lose their quality when entering first-order SOC,  $\phi = 130^\circ$ ,  $D_{AB}^{pert} = -83.31\text{cm}^{-1}$  and  $E_{AB}^{pert} = 0.21\text{cm}^{-1}$  compared with the values extracted from CAS(18,10)DDCI/DDCI-SO and effective Hamiltonian theory  $D_{AB} = -45.20\text{cm}^{-1}$  and  $E_{AB} = 0.02\text{cm}^{-1}$ . The rhombicity is negligible justifying the use of the smaller active space CAS(6,4) compared to the CAS(18,10).

The matrix 4.1 was extracted from *ab initio* CAS(6,4)DDCI/DCCI-SO calculation at  $\phi = 130^\circ$  and in the absence of an electrical field. Its numerical matrix is shown in Table 4.2, which shows a good correspondence. Note that the coupling terms  $h_i$  are equal to zero making it impossible for DMI to occur. Diagonalising this matrix with or without the inclusion of  $T_3^+$  and  $S_3$  allows to determine their individual contributions to the  $D_{AB}$ , which are reported in Table 4.3. The sum of these contributions matches perfectly with the value obtained via  $H^{eff}$ .

Note that from the final value of  $D_{AB}$  and the perturbative expression 4.3.1, it is clear that the main contribution to the  $D_{AB}$  comes from  $T_3$  and  $S_3$  even

$\hat{H}^{SO}$	$ T_1^+\rangle$	$ T_2^+\rangle$	$ T_3^+\rangle$	$ T_4^+\rangle$	$ T_1^0\rangle$	$ T_2^0\rangle$	$ T_4^0\rangle$	$ S_1\rangle$	$ S_3\rangle$	$ S_4\rangle$
$\langle T_1^+  $	1585	0	1079i	12	0	0	0	0	0	0
$\langle T_2^+  $	0	2362	0	0	0	0	0	0	0	0
$\langle T_3^+  $	-1079i	0	3275	1079i	0	0	0	0	0	0
$\langle T_4^+  $	12	0	-1079i	5036	0	0	0	0	0	0
$\langle T_1^0  $	0	0	0	0	1585	0	12	0	-1078i	0
$\langle T_2^0  $	0	0	0	0	0	2362	0	-1075i	0	-1076i
$\langle T_4^0  $	0	0	0	0	12	0	5036	0	-1078i	0
$\langle S_1  $	0	0	0	0	0	1075i	0	550	0	2
$\langle S_3  $	0	0	0	0	1078i	0	1078i	0	3369	0
$\langle S_4  $	0	0	0	0	0	1076i	0	2	0	4486

Table 4.2: Numerical matrix of  $\hat{H}^{SO}$  and electronic couplings in the uncoupled basis from a CAS(6,4)DDCI/DDCI-SO calculation with no electric field and  $\phi = 130^\circ$ .

	$D_{AB}$
Contribution of $T_3^+$ and $T_3^-$	-1176.74
Contribution of $S_3$	1124.28
Sum	-52.46
$D_{AB}$ from $H^{eff}$	-52.46

Table 4.3: Variational contribution in  $\text{cm}^{-1}$  of the excited states to  $D_{AB}$  and its value in  $\text{cm}^{-1}$  extracted from effective Hamiltonian at CAS(6,4)DDCI/DDCI-SO level

with the large active space CAS(18,10). This justify once more the use of the small CAS(6,4) calculations.

#### 4.4 Impact of the electric field on the symmetric anisotropic exchange parameter

This section focuses on the behaviour of the anisotropic parameter in first-order spin orbit coupling, at  $\phi = 130^\circ$ , with the application of an external electric field. Only changes in the electronic structure are studied, not the geometric ones. Indeed a previous study showed that the geometric changes only affect the values of the parameters and not their physical origin.

To obtain an initial estimate of the impact of the electric field on the  $D_{AB}$  parameter, CAS(6,4)SCF/SCF-SO calculations were performed with the electric field applied in the three cartesian directions (the axes are represented on Figure 4.1). The results are shown in Figure 4.3, a slight variation is observed when the electric field is applied along the X axis, but no change when it is applied

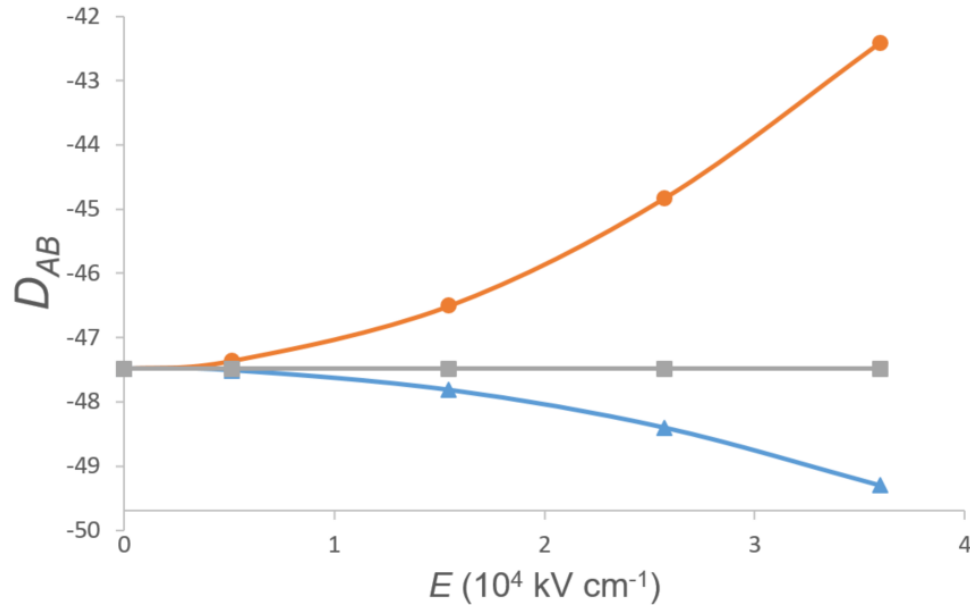


Figure 4.3:  $D_{AB}$  (in  $\text{cm}^{-1}$ ) as a function of the electric field applied in the X (blue line with triangles), Y (red line with circles) and Z (grey line with squares) directions, obtained at CAS(6,4)SCF/SCF-SO

along the Z direction. However, when the electric field is applied in the Y direction, a significant variation is observed. This behaviour was also observed in the study of the DMI where the largest value was obtained with the electric field along the Y direction. Therefore, this direction of application was chosen for further investigation as it showed the greater change in the two parameters. The impact of electron correlation is shown on Figure 4.4 with the evolution of the  $D_{AB}$  parameter under an electric field. It shows a large impact of both correlated energies and wave-functions as the field increases. The importance of dynamical correlation is expected, because as the field increases so does the DMI value making the use of DDCI energies and wave-function, *i.e.* CAS(6,4)DDCI-DDCI-SO, mandatory as shown in previous studies.

Applying the electric field in the Y direction results in a decrease of the axial parameter magnitude  $|D_{AB}|$ . To identify the cause of this decrease, the numerical matrix 4.4 was extracted.

Note that now, the  $h_i$  terms are no longer zero, allowing DMI via the coupling from eq 4.2.5. The same diagonalisation procedure as in section 4.3 is applied, selecting states that may contribute to either the  $D_{AB}$  or the DMI. This enables the impact of the electric field on the axial parameter and its behaviour in the presence of DMI to be determined. The decomposition of the different

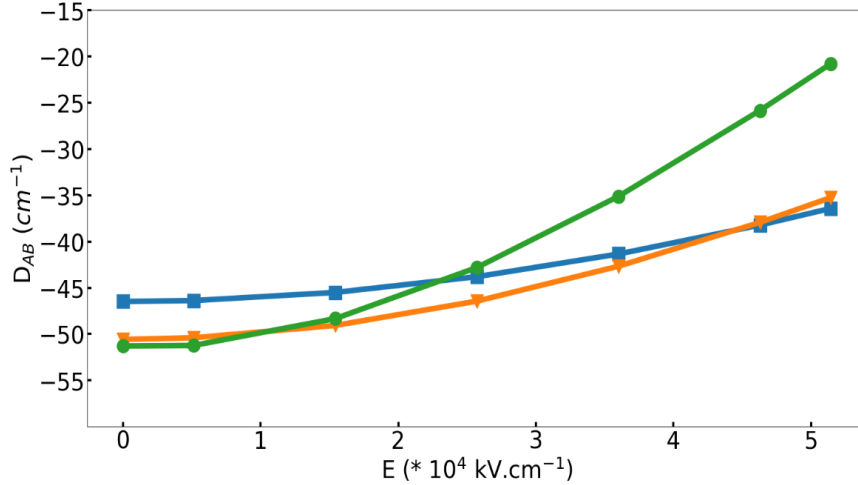


Figure 4.4:  $D_{AB}$  (in  $\text{cm}^{-1}$ ) as a function of the electric field applied in the Y direction, obtained at (i)CAS(6,4)SCF/SCF-SO (blue line with squares), (ii) CAS(6,4)DDCI/SCF-SO (orange line with triangles) and (iii) CAS(6,4)DDCI/DDCI-SO (green line with circles)

$\hat{H}^{SO}$	$ T_1^+\rangle$	$ T_2^+\rangle$	$ T_3^+\rangle$	$ T_4^+\rangle$	$ T_1^0\rangle$	$ T_2^0\rangle$	$ T_4^0\rangle$	$ S_1\rangle$	$ S_3\rangle$	$ S_4\rangle$
$\langle T_1^+  $	1580	-201	1078i	12	0	0	0	0	0	0
$\langle T_2^+  $	-201	2394	0	203	0	0	0	0	0	0
$\langle T_3^+  $	-1078i	0	3294	1077i	0	0	0	0	0	0
$\langle T_4^+  $	12	203	-1077i	5081	0	0	0	0	0	0
$\langle T_1^0  $	0	0	0	0	1580	-201	12	0	-1078i	0
$\langle T_2^0  $	0	0	0	0	-201	2394	203	-1075i	0	-1075i
$\langle T_4^0  $	0	0	0	0	12	203	5081	0	-1077i	0
$\langle S_1  $	0	0	0	0	0	1075i	0	556	202	1
$\langle S_3  $	0	0	0	0	1078i	0	1077i	202	3369	-207
$\langle S_4  $	0	0	0	0	0	1075i	0	1	-207	4541

Table 4.4: Numerical matrix of  $\hat{H}^{SO}$  and electronic couplings in the uncoupled basis from a CAS(6,4)DDCI/DDCI-SO calculation in the presence of an electric field of 0.01 a.u ( $5.1724 \times 10^4 \text{ kV.cm}^{-1}$ ) and  $\phi = 130^\circ$ .

contributions is reported in Table 4.5. The contributions from the  $T_3^{\pm 1}$  and  $S_3$  as well as the sum of the two, are comparable to the previous case in the absence of electric field. The effect of the electric field is mainly evident in the  $h_1$  and  $h'_1$  terms, which couple the components of the  $T_1$  and  $T_2$  states, thereby enabling DMI to emerge. These two couplings have large contributions to the  $|d_{AB}|$  term, accounting for 99% of the DMI parameter extracted from  $H^{eff}$ . On the other hand, these couplings have positive contributions to the  $D_{AB}$ , leading to a decrease in its magnitude  $|D_{AB}|$ . This demonstrates that there is

	$D_{AB}$	$ d_{AB} $
Contribution of $T_3^+$ and $T_3^-$	-1162.0	0
Contribution of $S_3$	1111.4	0
Sum	-50.6	0
Contribution of $h'_1$	-7	-86.6
Contribution of $h_1$	29.3	329.7
Contribution of $h'_2$	5.9	29.1
Contribution of $h_2$	-0.4	-24.0
Total sum	-22.8	248.2
Parameters from $H^{eff}$	-21.03	245.0

Table 4.5: Variational contribution in  $\text{cm}^{-1}$  of the excited states to  $D_{AB}$  and  $|d_{ab}|$  given in value in  $\text{cm}^{-1}$  extracted from effective Hamiltonian at CAS(6,4)DDCI/DDCI-SO level

an interferential behaviour between the two anisotropic parameters when the field is applied in the Y direction. This behaviour is not observed for other orientations. When the field is applied along the X direction, the  $D_{AB}$  term is affected (see Figure 4.3) while the  $d_{AB}$  remains zero as previously shown. Along the Z direction, it is the  $D_{AB}$  parameter that stays constant while a  $d_{AB}$  term can be observed, albeit much smaller.

## 4.5 Conclusion

This work studied the behaviour of the symmetric anisotropy parameters were studied in a binuclear Cu(II) complex, identifying different mechanisms as the source of their variations. The first part focused on the impact of first-order coupling on the axial  $D_{AB}$  and rhombic  $E_{AB}$  terms under certain geometry conditions. It showed that as the local environment of each metallic centre approaches a  $C_3$  symmetry, the condition for first-order coupling are met, allowing for large values of axial anisotropy. Initially, parameters were extracted perturbatively using previously derived expressions. However, this method of extraction proved to be no longer valid in first-order SOC regime and a variational approach was devised instead. This approach relies on the diagonalisation of the electronic and spin-orbit matrix in the basis of the three  $M_S$  components of the four triplet and four singlet states generated by a reduced active space consisting of the two highest d-orbitals. In this first part, the importance of the use of dynamically correlated wave-function during the extraction was determined. It showed that in the absence of DMI terms, reasonable values of the  $D_{AB}$  parameter can be obtained using the non-dynamically correlated CASSCF wave-function using corrected energies during the SO-SI step of the calculation. Once a DMI term appears, this is no longer true and the use of both the correlated energies and wave-function are necessary for a rigorous extraction. The second part introduces the application of an external electric field, focusing on its impact on the axial parameter. As with the DMI, it was demonstrated that the  $D_{AB}$  can also be influenced by an electric field and could contribute to the magneto-electric coupling. Three orientations of the electric field were explored and it was shown that, in one instance an interferential behaviour could be observed between the  $D_{AB}$  and  $d_{AB}$  terms. Analysis of the numerical matrices showed that the coupling at the DMI source for this field orientation also impacted the magnitude of the axial parameter: when the former increased, the latter decreased.

This work complements a series of studies attempting to define a recipe for obtaining large values for the parameters of both types of anisotropy (symmetric and antisymmetric). Two key elements have been identified as necessary in order to obtain such results:

- (i) geometries around the metal must allow the near-degeneracy of d-orbitals to approach first-order SOC. This can be achieved with geometries containing

symmetries such as a  $C_3$  axis.

- (ii) hybridisation of the degenerate orbitals must be possible via the application of an electric field. The choice of orientation of the field leads different type of hybridisation due to the deformation of the electronic cloud.

These considerations could pave the way for the design of compounds with strong magneto-electric coupling.

# Chapter 5

## Herbertsmithite

### Computational Informations

The structure studied was taken from a X-ray study, the Hydrogen position were optimised using periodic DFT with PBE functional implemented in the Quantum Espresso code.

Density functional theory calculations were performed using the ORCA package with def2-TZVP basis set on all atoms and the  $\omega$ B97X-D3 functional which has shown to provide very good value of magnetic couplings. Wave-function based method calculations were carried out with the MOLCAS and CASDI codes with the extended ANO-RCC basis set (6s5p3d2f for Cu and Zn, 4s3p2d for O, 4s3p1d for Cl and 2s1p for H)

The embedding's pseudopotential were set to the SDD Effective Core Potentiel (ECP) for ORCA calculations and *ab initio* model potentials (AIMP) for MOLCAS calculations. The quality of the embedding was checked by comparing the value of  $J_1$  using the B3LYP functional for embedded cluster and periodic calculations (using the Crystal code). The J1 values are in perfect agreement: 240K for periodic and 239K for embedded cluster. As we will see below, these B3LYP values slightly overestimate the coupling but demonstrate the adequacy of the embedding adopted in this study.

### 5.1 Density-Functional Theory study

In a first approximation, the isotropic behavior of Herbertsmithite is described by an unique first neighbor coupling. The highly-correlated nature of such system suggests the possibility of longer range interaction between copper ions separated by one or more neighbors. To explore this possibility, the need to

compute large fragments arises making the application of wave-function based method complicated. First the number of  $\text{Cu}^{2+}$  into the fragment has a direct impact on the size of the active space, even restricting to one orbital/one electron per copper centres leads to convergence troubles in the calculations. Also, the number of determinant and spin states generated prohibits the use of Post-CASSCF methods which are crucial for a good estimation of magnetic couplings. Finally, the number of spin states render an analytical derivation complicated with large matrices to diagonalize. As such, Density Functional Theory provides a good middle ground to compute large systems. It also presents some disadvantages, the DFT wave-function is monodeterminantal and usually not an eigenfunction of the  $\hat{S}^2$  operator which prevents the mapping on the HDvV Hamiltonian. Nevertheless, the combined use of Broken-Symmetry DFT (BS-DFT) and the Ising Hamiltonian provides a good way to obtain an estimation of the couplings in the system. The Broken-Symmetry approach relies on the computation of DFT solutions where the  $M_S$  value of spin moment of each copper ion of the fragment have been imposed beforehand to  $\pm\frac{1}{2}$ . It is then possible to obtain multiple solutions per fragments to make a connection between the energy differenceés of each solution and the Ising Hamiltonian energies. Additionaly, the time necessary for a DFT calculation and for the derivation of its analytical solution allows for the exploration of different properties of the embedding such as the size of the fragments and its overall quality.

### 5.1.1 In-plane couplings

In a first description, a fragment presenting only the first neighbor coupling was introduced with three copper ions as shown on Figure ??(a). Four solutions can be computed with  $M_S \geq 0$ , first a  $M_S = 3/2$  where all magnetic moment of the  $\text{Cu}^{2+}$  ions are aligned creating a fully ferromagnetic solution. Then, three other solutions are possible by switching the  $M_S$  value of one of the  $\text{Cu}^{2+}$  ion to  $-1/2$ . If the choice of fragment and construction of the embedding are done correctly, this should lead to three equal energy differences as these solutions are degenerate in the Ising Hamiltonian.

Let us call the highest occupied orbital of each copper ion a, b and c. The Slater determinant describing the high spin solution ( $M_S=+1/2$  on each  $\text{Cu}^{2+}$ ) can then be written  $|abc|$  while the low spin solutions (one of the  $M_S$  value is switched to  $-1/2$ ) are written  $|ab\bar{c}|, |\bar{a}bc|$  and  $|\bar{a}\bar{b}c|$ . Applying  $\hat{H}_{\text{Ising}} = \sum_{i,j} J_1 \hat{S}_{i,z} \hat{S}_{j,z}$  to the high spin (HS) solution  $|abc|$  gives the eigenvalue  $\frac{3}{2}J_1$

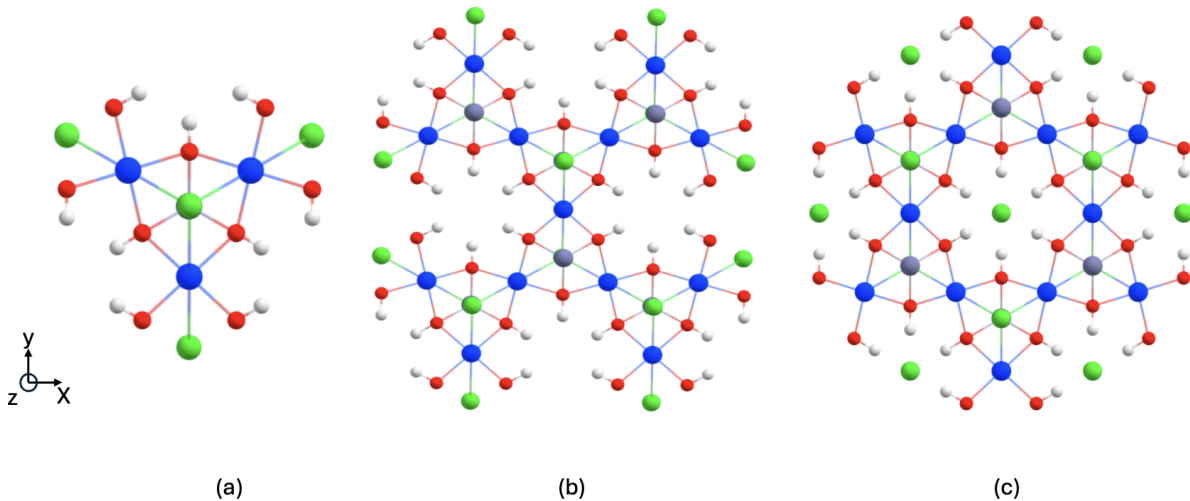


Figure 5.1: The three computed fragments using DFT calculations for in-plane couplings. Cu are represented in blue, Zn in grey, Cl in green, O in red and H in white.

while the application on the low spin (LS) solutions gives the eigenvalue  $\frac{1}{2}J_1$ . The Ising Hamiltonian's matrix representation is diagonal:

$H_{Ising}$	$ abc $	$ ab\bar{c} $	$ a\bar{b}\bar{c} $	$ \bar{a}\bar{b}\bar{c} $
$ abc $	$\frac{3}{2}J_1$	0	0	0
$ ab\bar{c} $	0	$\frac{1}{2}J_1$	0	0
$ a\bar{b}\bar{c} $	0	0	$\frac{1}{2}J_1$	0
$ \bar{a}\bar{b}\bar{c} $	0	0	0	$\frac{1}{2}J_1$

Table 5.1: Matrix representation of the Ising Hamiltonian in the basis of determinants  $M_S=1/2$  and  $M_S=3/2$

The value of  $J_1$  can then be extracted from the difference in energy between the high spin solution and low-spin ones:

$$J_1 = E_{HS} - E_{LS} \quad (5.1.1)$$

The same procedure of extraction can now be applied to larger fragments allowing the introduction of longer range couplings. The second fragment created included nine copper ions which allows for the consideration of two new couplings,  $J_2$  and  $J_3$  represented on Figure 5.2. It indicated that these couplings were small ( $|J_2| \approx |J_3| \approx 1\text{cm}^{-1}$  each) with a large standard deviation. While these results provided good insight on the nature of these two couplings, the extraction was unsatisfactory. The source of this deviation is believed to be

$J_i(K)$	(a)	(b)	(c)	$d_{Cu-Cu}$ (Å)
$J_1$	178.0	191.2	181.0	3.42
$J_2$	-	0.5	0.4	5.91
$J_3$	-	-1.1	-1.0	6.83
$J_4$	-	-0.1	-0.2	6.83

Table 5.2: Values of the  $J_i$  couplings in Kelvin in the three fragments and the distance associated to each couplings.

the environment of ions taking part in the interaction. The extraction of these couplings requires to flip the spin of at least one of the ion at the edge of the fragment whose neighboring atoms are not always explicitly computed (treated with ECP's). It was decided to increase the size of the fragment to twelve and thirteen copper ions (fragment (c) and (b) from Figure 5.1) so that there would be ways account for these interaction within the centre of the fragments.

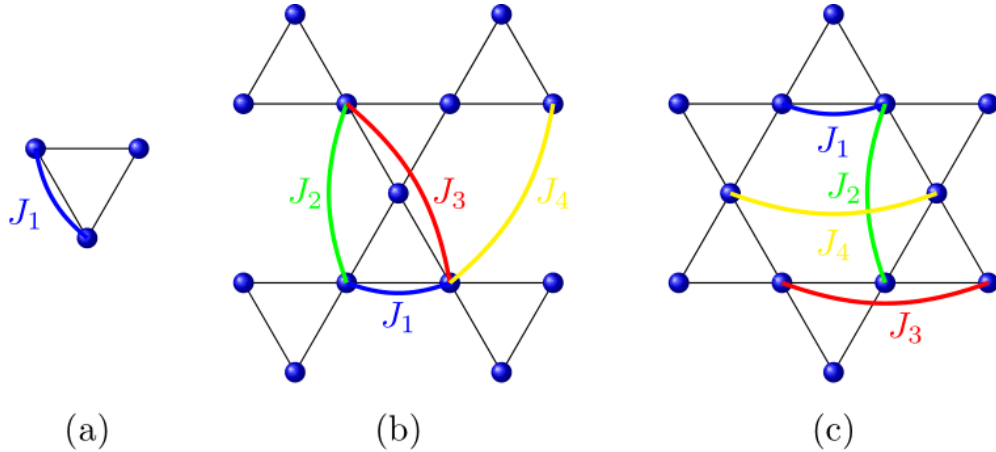


Figure 5.2: Schematic representation of the fragments and the couplings introduced

The results obtained for each couplings in the three fragments are presented in Table 5.2. The first thing to comment is the good transferability with a small relative deviation from one cluster to the other. Note that with this convention of the Ising Hamiltonian (a plus sign in front of the  $J$  term), a positive value indicates antiferromagnetism while negative indicates ferromagnetism. The closest neighbor interaction  $J_1$  is in good agreement with values published in the litterature while  $J_2, J_3$  and  $J_4$  are very weak.

These results highlight the mainly antiferromagnetic nature of these interactions with a leading interaction  $J_1$ , at least two order of magnitude higher than the other. This confirm the the use of models composed of only one  $J$  interaction, the negligenge of other couplings should cause no more than a small deviation.

### 5.1.2 Out-of-plane coupling

Another preoccupation of the model is the occupation disorder. Cristallographic studies have identified two types of defect present at low temperatures. The first is the substitution of the  $Zn^{2+}$  inter-plane site with a  $Cu^{2+}$  ion, estimated to occur at a rate of 0.15, and the second is a  $Zn^{2+}$  ion entering the Kagome plane with a much smaller occurrence rate ( $<0.05$ ). The latter is suspected to appear even less ( $<0.01$ ) because of the difficulty of the  $Zn^{2+}$  ion to enter the  $Cu^{2+}$  site in the kahome plane. As such, our study focus on the first type. Following the same approach, an embedding with the defect at its centre was constructed to include the inter-ion, the fragment is shown in Figure 5.3. This cluster contains two layers of Kagome planes, each with three  $Cu^{2+}$  ions and their neighbouring ions while the interstitial  $Zn^{2+}$  ion is replaced by a copper ion. In a structuraly perfect Kagome lattice, the inter\*-site is occupied by a  $Zn^{2+}$  ion which is not susceptible to the Jahn-Teller effect because of its doubly occupied d-orbitals, allowing for a  $C_3$  symmetry axis. However, replacing this ion with a  $Cu^{2+}$ , which is susceptible to the Jahn-Teller effect with a singly occupied d-orbital, induces structural deformation in the vicinity of the defect.

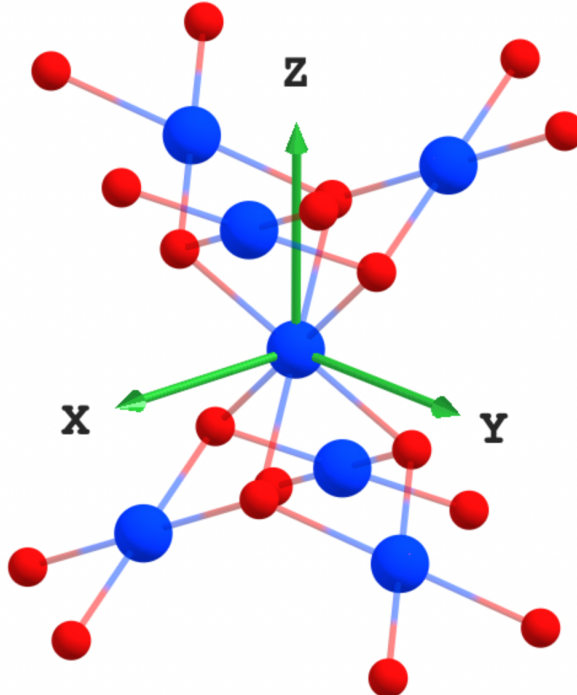


Figure 5.3: Embedded cluster used to compute the out of plane coupling before geometry optimisation. The three copper ions (blue) at the top and bottom of the fragment each belong to their own kagome plane. Hydrogens atoms are hidden.

To account for the deformations, the structure of the fragment was optimised using the ORCA package via DFT calculations with the PBE or B3LYP functionals. It is expected that local impurities act only locally and should not have any long range effect, thus no changes were made to the embedding. To order to maintain the rigidity of the crystal structure only the coordination sphere of the defect, *i.e.* the hydroxide groups close, was left free during optimisation, while the positions of the remaining ions were constrained. Depending on the functional used, two different types of structure were obtained. The PBE functional calculation converges towards a structure with four short Cu-O bonds and two long ones, this structure is referred to as the “4+2” structure. While the B3LYP functional calculation converges towards the opposite, with two short Cu-O bonds and four long ones. This structure is labelled “2+4”. In order to determine the most stable structure, one would compare the final single-point energy provided by the program at the end of the *SCF* cycle. However, comparing energies obtained using different functionals is not appropriate. Therefore, a second set of optimisations was performed starting from the previously obtained PBE (B3LYP) structure but now using the B3LYP (PBE) functional. Both calculations converged towards the “4+2” structure which was found to be slightly lower in energy than the “2+4” structure with a difference of  $\Delta E = 100K$  using the B3LYP functional. As the two structures are quite close in energy, a difference lower than the estimated first neighbour coupling, both structures were explored for the extraction of  $J$  couplings.

These distortions, together with the presence of a copper ion at the intersite, require the definition of new  $J_i$  couplings. Table 5.3 shows the distances between the oxygens atoms and the different  $Cu^{2+}$  ions in the unoptimised structure and the relative displacements induced by the defect. In both the optimised structures, one type of oxygens moves away from the in-plane copper while the other moves closer.

	$C_3$	“4+2”	“2+4”
$Cu_{defect} - O(1)$	2.11887	$-7.50.10^{-2}$	$4.24.10^{-2}$
$Cu_{defect} - O(2)$	”	$11.55.10^{-2}$	$-11.72.10^{-2}$
$Cu_{plane} - O(1)$	1.98423	$2.86.10^{-2}$	$0.40.10^{-2}$
$Cu_{plane} - O(2)$	”	$-1.17.10^{-2}$	$4.65.10^{-2}$

Table 5.3: Distance between the oxygens and the copper ions, defect or in plane, in the  $C_3$  structure and the relative displacement in both optimisation scheme given in Å.

This displacement results to a second in-plane coupling  $J'_1$ , which differs

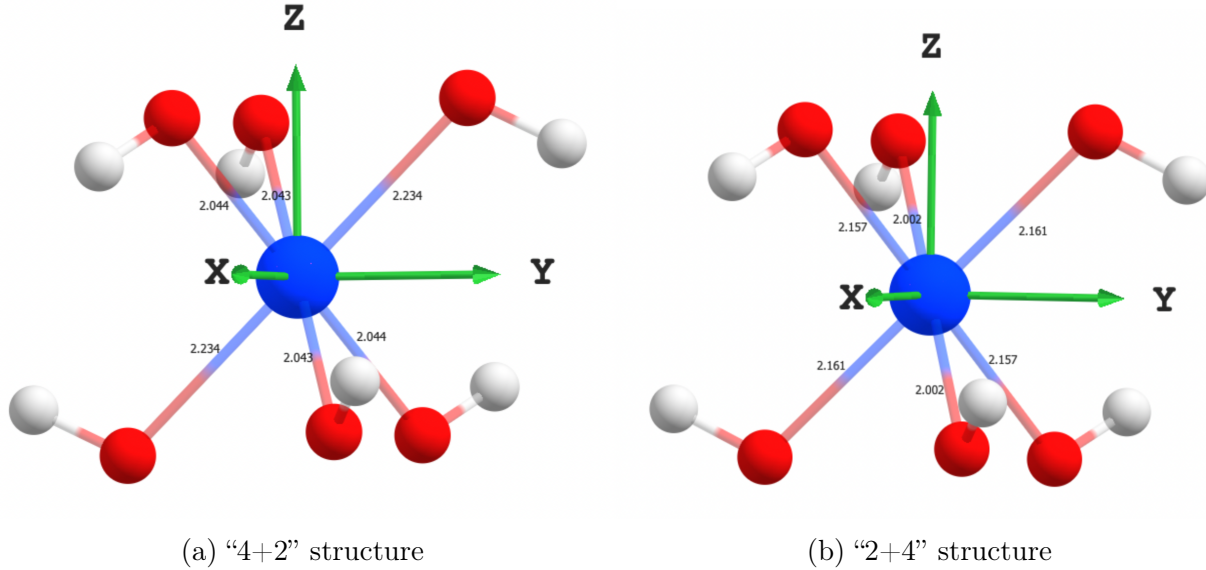


Figure 5.4: Close environment of intersite  $Cu^{2+}$  in both structure obtained via DFT with the B3LYP functional. The bond lengths are shown in Angstrom

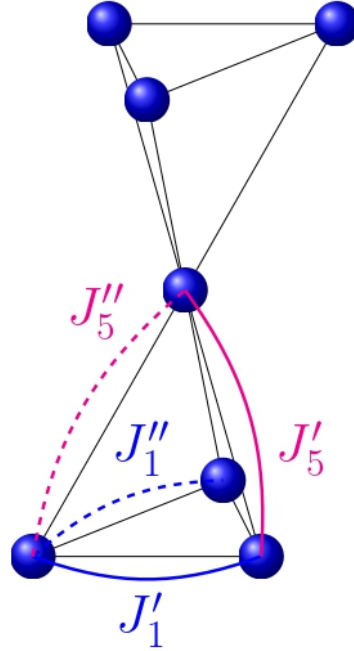


Figure 5.5: Schematic representation of the  $J_i$  couplings in the cluster with defect.

from the  $J_1$  by the distance between the copper ions and the bridging oxygen. Focusing on a triad of  $Cu^{2+}$  ions of the same plane, two bridging oxygens

occupy equivalent positions while the third one occupies a different one. The  $J'_1$  coupling is defined between two  $Cu^{2+}$  ions bridged by one of the two equivalent oxygens for a total of two  $J'_1$  couplings in the triad while  $J''_1$  denotes the final possible coupling. The out-of-plane coupling is a bit more complicated as the two copper ions involved are bridged by two oxygens. The coupling between two  $Cu^{2+}$  bridged by two equivalent oxygens is called  $J'_5$  and appears once in the triad involving the defect. The coupling going through two non-equivalent bridges, in turn, is referred to as  $J''_5$ , this coupling appears twice in the triad. These couplings are represented in Figure 5.5, the dashed-line indicates couplings that involves the non-equivalent oxygen position.

$J_i$ (K)	$J'_1$	$J''_1$	$J'_5$	$J''_5$
“4+2”	92.9	262.9	-47.5	-73.0
“2+4”	185.3	66.14	-81.61	-63.4

Table 5.4: Values of the  $J_i$  interactions given in Kelvin in presence of a  $Cu^{2+}$  defect in the intersite for the  $C_3$  and both optimised structure.

Table 5.4 shows the values extracted using BS-DFT for both the optimised. Calculations were also performed on the  $C_3$  structure in order to provide comparisons. The  $C_3$  structure indicates a strong  $J_1 = 184.22K$  antiferromagnetic coupling which is consistent with previously extracted values, as well as a non negligible out-of-plane ferromagnetic coupling  $J_5 = -80.64K$ . Extractions from the optimised structure show a significant impact of the deformations on the first neighbor coupling. Firstly, coupling within the plane decreases as oxygen atoms move away from it, whereas it increases as they move closer. This can be rationalised by the variation of the hopping term between ligand and metal, involved in the superexchange contribution to the  $J$  coupling, which decreases with distance. Note that these displacements lead to significant differences in the values of couplings of the same nature, *i.e.*  $J''_1$  and  $J''_5$  or  $J'_1$  and  $J'_5$ . The most important result of this study is the identification of ferromagnetic couplings between the in-plane copper ion and the defects. These couplings are no negligible and can go up to  $0.4|J_1|$  which should have an impact on the physics of the system.

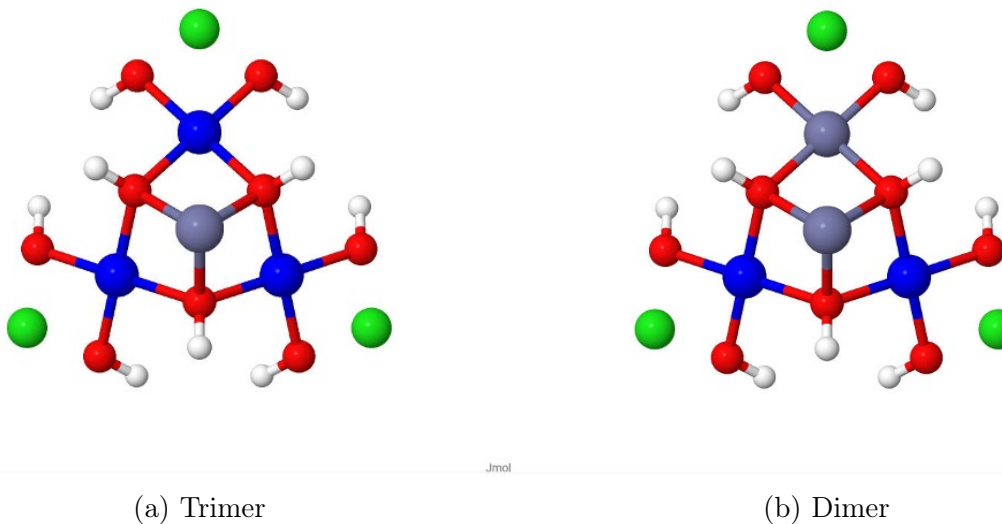


Figure 5.6: Trinuclear and dinuclear embedded clusters used for Wave-funciton computation

## 5.2 Wave-Function Theory study

The second purpose of this study was the determination of anisotropic interaction in the crystal. The extraction of such interactions follows the same procedure as described in Chap. 4. The computation of SO-states being very computationally demanding, this extraction will be resticted to two fragments of small size.

The first fragment, Figure 5.6 (left), is similar to the one used for DFT calculation, with three copper ions arranged in an equilateral triangle. A second fragment 5.6 (right) was designed by substituting one of the  $Cu^{2+}$  with a diamagnetic  $Zn^{2+}$ , both share rather close structural properties (charge, mass, ionic radius). As the d shell of the zinc ion is completely filled it will not take part in the magnetic interactions, leaving us with essentially a dimer to capture the interaction of only two  $Cu^{2+}$  ions. This approach has been studied in serveral other materials and we will see from the results that this substitution has little impact on the extracted values but can significantly reduce ther overall study time.

### 5.2.1 Isotropic Coupling

To check the applicability of WFT calculation to this system, the first step was to try and reproduce the  $J_1$  value. In both cluster, two type of active space were considered:

- one electron and orbital per magnetic center.
- all electrons occupying the d shell of each magnetic center.

The first type of active space results in a CAS(2,2) for the dimer calculation which generates one triplet ( $S=1$ ) and one singlet ( $S=0$ ) state.

$$|1, 1\rangle = |ab| \quad (5.2.1)$$

$$|1, 0\rangle = \frac{1}{\sqrt{2}}(|a\bar{b}| - |b\bar{a}|) \quad (5.2.2)$$

$$|1, -1\rangle = |\bar{a}\bar{b}| \quad (5.2.3)$$

$$|0, 0\rangle = \frac{1}{\sqrt{2}}(|a\bar{b}| + |b\bar{a}|) \quad (5.2.4)$$

These functions are eigenfunctions of the  $\hat{\mathbf{S}}^2$  operator, as such their energies can be mapped on the HDvV Hamiltonian's eigenvalues. The value of  $J_1$  is then given by the difference in energy between the triplet and singlet state  $J_1 = E(S = 1) - E(S = 0)$ . The enlarged active space CAS(18,10) generates 25 Triplet and 25 Singlet states.

In the case of the trimer cluster, CAS(3,3) represents the minimum active space which generates one quartet ( $S=3/2$ ) state and two doublet ( $S=1/2$ ) states. The two doublets are degenerate if only one value of  $J$  is taken into account as is our case with an equilateral repartition of the copper ions.

$$|3/2, 3/2\rangle = |abc| \quad (5.2.5)$$

$$|3/2, 1/2\rangle = \frac{1}{\sqrt{3}}(|a\bar{b}\bar{c}| + |a\bar{b}c| + |\bar{a}bc|) \quad (5.2.6)$$

$$|1/2, 1/2\rangle_1 = \frac{1}{\sqrt{6}}(|a\bar{b}\bar{c}| + |a\bar{b}c| - 2|\bar{a}bc|) \quad (5.2.7)$$

$$|1/2, 1/2\rangle_2 = \frac{1}{\sqrt{2}}(|a\bar{b}\bar{c}| - |a\bar{b}c|) \quad (5.2.8)$$

The expressions of the negative  $m_s$  value components were left out as they only differ by the number of up and down spins. The value of  $J_1$  is then given by  $J_1 = \frac{2}{3}(E(S = 3/2) - E(S = 1/2))$ . The enlarged active space CAS(27,15) generates 125 quartet and 250 doublets states.

CASSCF calculation tends to "over"-localise the wave-function on the metallic center, thus underestimating mechanism at the origin of the antiferromagnetic contribution to the  $J$  integral. As such it does not provide a good estimate but

Fragment	CAS(2,2) CAS(3,3)	CAS(18,10) CAS(27,15)	CASPT2	DDCI1	DDCI3
Dinuclear	10.7	8.3	69.8	50.0	80.1
Trinuclear	8.2	7.7	56.0	50.7	60

Table 5.5: Values of  $J_1$  in  $\text{cm}^{-1}$  extracted on both fragment. Dynamical correlation calculation are performed on the miniaml active space.

can nonetheless give informations about the nature of the coupling. Table 5.5 shows the results obtained at different levels of calculation for different active spaces.

These results indicate an antiferromagnetic  $J$  coupling with a large impact of dynamical correlation, yet these values do not match with the DFT calculations and the litterature. An active space only composed of d-orbitals is not enough to achieve a correct estimation of the isotropic coupling in this system, to improve the description of the antiferromagnetic mechanisms it was then thought to include the bridging ligand orbitals into the active space. The inclusion of the p-orbitals of the bridging oxygen presents a challenge, as they stay doubly occupied and do not contribute to the wave-function at CAS level, reaching a stable active space becomes challenging because of convergence issue. To avoid these troubles, a methodology based on the projection of the oxygen's p-orbitals onto the ligand's tail of the active orbitals was applied. This allows to obtain a reproducible active space with well defined orbitals represented on Figure 5.7 in the dinuclear calculation and Figure 5.8 in the trinuclear.

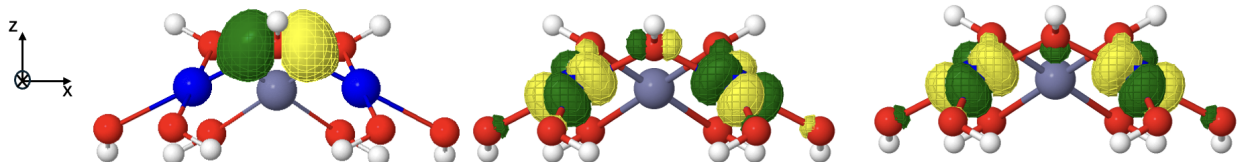
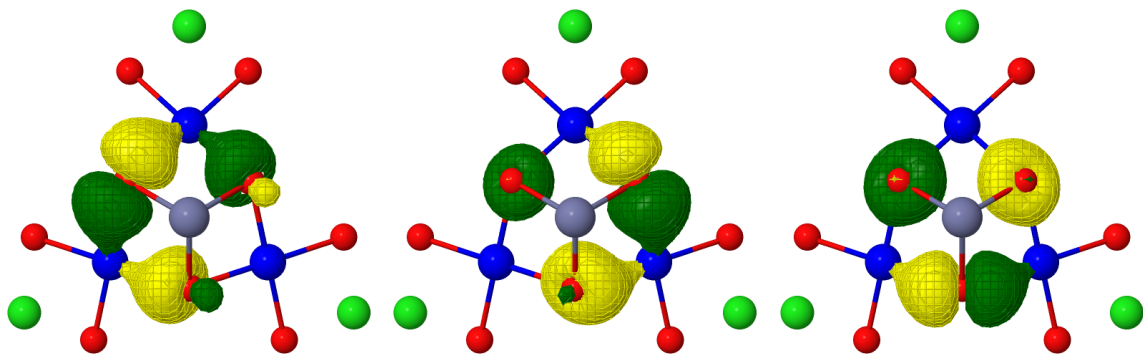
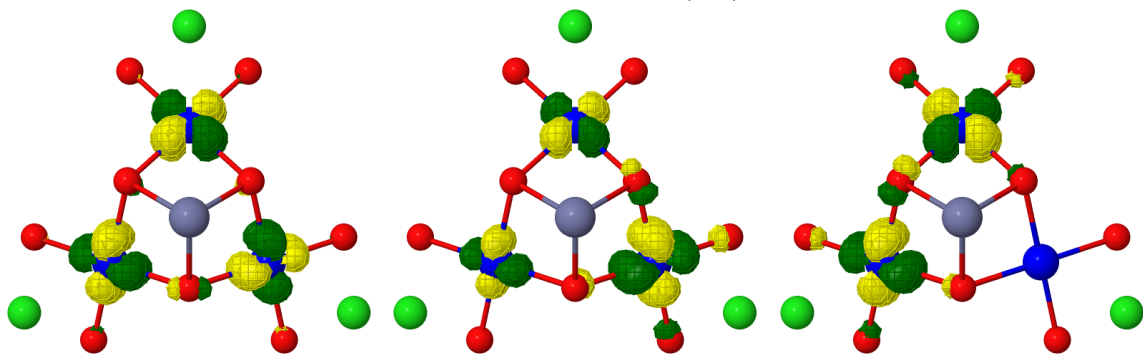


Figure 5.7: CAS(4,3)SCF, bridging orbital and magnetic orbitals calculated on the dinuclear fragment

It has been previously established that performing a DDCI1 calculation on a active space composed of the ligands orbitals in addition to the magnetic orbitals allows to obtain value of  $J$  coupling on par to a DDCI3 calculation. This allows to greatly reduce computational time, the active space is now composed of one electron/orbital per metallic centre and two electrons in one orbital per oxygen (CAS(4,3) in the dinuclear and CAS(9,6) in the trinuclear fragment). This

Bridging orbitals from the  $\text{CAS}(9,6)$  calculation.Magnetic orbitals from the  $\text{CAS}(9,6)$  calculation.Figure 5.8: Active space orbitals from  $\text{CAS}(9,6)$  calculation.

procedure has allowed the extraction of new values for  $J_1$  in both fragment,  $J_1 = 105.3\text{cm}^{-1}$  in the dinuclear cluster and  $J_1 = 126.3\text{cm}^{-1}$  in the trinuclear cluster. Even if the dinuclear value of  $J_1$  is lower, the coupling extracted from the trinuclear fragment is well within range of the expected value by both DFT and experiment as such the extraction is considered satisfactory.

### 5.2.2 Anisotropic interactions

The computation of the isotropic couplings was a way to ascertain the validity of our methods and calibration of the embedded cluster method. The electronic structure of the compound seems to be well replicated with a satisfactory value of the  $J_1$  coupling. We can now address the main purpose of this study, which is to extract anisotropic interactions. Theoretical model propose the inclusion of a weak Dzyaloshinskii-Moriya pseudo-vector along the out of plane direction to account for the behavior at low temperature but the symmetric tensor of anisotropy  $\overline{\overline{D}}_{ij}$  is usually left out. Following the procedure explained in Chap.4, all three components of the DMI were extracted as well as the  $D_{ij}$ -tensor.

#### Bi-nuclear calculation

Starting from the CASSCF wave-function obtained with the enlarged active space of all 18 copper d-shell electrons and the 10 d-orbitals, computation of the SO-states was performed using the SO-RASSI method implemented in MOLCAS. The lowest part of the energy spectrum was corrected using the isotropic coupling value previously obtained. No assumption on the magnetic axes was made and so the extraction of all anisotropic parameters (9 in total) was performed using effective hamiltonian theory with a model space composed of the three  $M_S$  component of the triplet state and the singlet state. The matrix representation of the model Hamiltonian in the model space basis is:

$H_{MS}$	$ 1, -1\rangle$	$ 1, 0\rangle$	$ 1, 1\rangle$	$ 0, 0\rangle$
$\langle 1, -1  $	$\frac{J}{4} + \frac{D_{zz}}{4}$	$\frac{D_{xz}-iD_{yz}}{2\sqrt{2}}$	$\frac{(D_{xx}-D_{zz}-2iD_{xy})}{4}$	$\frac{d_y+id_x}{2\sqrt{2}}$
$\langle 1, 0  $	$\frac{D_{xz}+iD_{yz}}{2\sqrt{2}}$	$\frac{J}{4} - \frac{D_{zz}}{4} + \frac{(D_{xx}+D_{yy})}{4}$	$-\frac{D_{xz}-iD_{yz}}{2\sqrt{2}}$	$-\frac{id_z}{2}$
$\langle 1, 1  $	$\frac{(D_{xx}-D_{zz}+2iD_{xy})}{4}$	$-\frac{D_{xz}+iD_{yz}}{2\sqrt{2}}$	$\frac{J}{4} + \frac{D_{zz}}{4}$	$\frac{d_y-id_x}{2\sqrt{2}}$
$\langle 0, 0  $	$\frac{d_y-id_x}{2\sqrt{2}}$	$\frac{id_z}{2}$	$\frac{d_y+id_x}{2\sqrt{2}}$	$-\frac{3J}{4} - \frac{D_{zz}}{4} - \frac{(D_{xx}+D_{yy})}{4}$

Note that the  $\mathbf{d}_{ij} \cdot \hat{\mathbf{S}}_i \times \hat{\mathbf{S}}_j$  operator is equivalent to the antisymmetric tensor

$\overline{\overline{T}}_{ij}$  of the operator  $\hat{\mathbf{S}}_i \overline{\overline{T}}_{ij} \hat{\mathbf{S}}_j$ . There is a one to one correspondence between its components, with  $d_x = T_{yz}$ ,  $d_y = -T_{xz}$  and  $d_z = T_{xy}$ . This remark will be useful for identifying the non-zero components of the vector via a symmetry analysis. The values obtained for both interaction expressed in Kelvin in the axis system of the cluster are:

$$\overline{\overline{D}}_{12} = \begin{pmatrix} 1 & 0 & 0 \\ 0 & 1 & 0 \\ 0 & 0 & 1 \end{pmatrix} \quad \mathbf{d}_{12} = \begin{pmatrix} 0 \\ 4.73 \\ 1.70 \end{pmatrix}$$

The symmetric tensor can be diagonalized to extract the  $D = -0.46K$  axial parameter and a small  $E = 0.13K$  rhombic term following the usual definition of these terms. These values are small and should have only little impact on the magnetic properties of this system. However, the DMI components are non-negligible. The di-nuclear fragment studied presents a  $C_S$  symmetry point group, with (YZ) being the symmetry plane. The symmetry rules for this point group have been derived to identify the non-zero components of the antisymmetric tensor  $\overline{\overline{T}}_{ij}$ . When the symmetry plane is (XY), these components are  $T_{xz}$  and  $T_{yz}$ . Replacing the X and Z axes to match our axes frame, *i.e.* X becomes Y, Y becomes Z and Z becomes X, one gets that the non-zero components are  $T_{xz} = d_y$  and  $T_{xy} = d_z$ . This rationalise the value obtained for the component along the X-axis, *i.e.*  $d_x$ , which is equal to zero. Note that the in-plane component (along the  $y$ -axis) is larger than the out of plane component (along the  $z$ -axis). This result can be surprising but can be rationalised by looking at the physical origins of the DMI component. It was demonstrated analytically that the DM-interaction comes from the hybridization of the metal's d-orbitals. It was shown that:

- a mixing between  $d_{x^2-y^2}$  and  $d_{yz}$  or  $d_{xy}$  and  $d_{xz}$  generates a  $d_x$  component.
- a mixing between  $d_{x^2-y^2}$  and  $d_{xz}$  or  $d_{xy}$  and  $d_{yz}$  generates a  $d_y$  component.
- a mixing between  $d_{x^2-y^2}$  and  $d_{xy}$  or  $d_{xz}$  and  $d_{yz}$  generates a  $d_z$  component.

This mixing can be clearly observed on Figure 5.7, and from the expression of one of these magnetic orbitals on the Cartesian d-orbitals of one copper ion :  $0.4889d_{x^2-y^2} + 0.2120d_{xz} - 0.2841d_{xy} - 0.3666d_{yz}$ .

Different configurations for the dinuclear cluster were explored to make sure that the values extracted were not affected by the choice of "couple" of  $Cu^{2+}$

ions. The extra zinc ion was swapped around all three in-plane sites. Note that the symmetry rules are only apply if the symmetry plane coincides with the axis frame of the dinuclear fragment under consideration. This is not the case for the other two dimer clusters, therefore, it is expected that all three components of the DMI will be non-zero. Therefore, it will be more adequate to refer to the in-plane projection as  $d_{\parallel}$  and the out of plane component as  $d_{\perp}$ . In all three calculations, the respective value of  $|d_{\perp}|$  and  $|d_{\parallel}|$  were found to be the same.

### Trinuclear calculations

The extraction was then performed on the tri-nuclear fragment with an active space of 27 electrons in 15 orbitals. In the case of three magnetic center, the model Hamiltonian is now written:

$$\begin{aligned}\hat{H}_{MS} = & J_{12} \hat{\mathbf{S}}_1 \cdot \hat{\mathbf{S}}_2 + \hat{\mathbf{S}}_1 \cdot \overline{\overline{D}}_{12} \cdot \hat{\mathbf{S}}_2 + \mathbf{d}_{12} \cdot (\hat{\mathbf{S}}_1 \times \hat{\mathbf{S}}_2) \\ & J_{12} \hat{\mathbf{S}}_2 \cdot \hat{\mathbf{S}}_3 + \hat{\mathbf{S}}_2 \cdot \overline{\overline{D}}_{23} \cdot \hat{\mathbf{S}}_3 + \mathbf{d}_{23} \cdot (\hat{\mathbf{S}}_2 \times \hat{\mathbf{S}}_3) \\ & J_{13} \hat{\mathbf{S}}_1 \cdot \hat{\mathbf{S}}_3 + \hat{\mathbf{S}}_1 \cdot \overline{\overline{D}}_{13} \cdot \hat{\mathbf{S}}_3 - \mathbf{d}_{13} \cdot (\hat{\mathbf{S}}_1 \times \hat{\mathbf{S}}_3)\end{aligned}\quad (5.2.9)$$

Note the negative sign in front of the last term  $d_{13}$  which originates from the permutation realtionship specific to the DMI ( $d_{13}=-d_{31}$ ). On the other hand, we set  $J_{12} = J_{23} = J_{13}$  and let the  $D_{ij}$ -tensor be expressed in the axis system of the cluster with 6 parameters each. First, we can obtain the matrix representation of this Hamiltonian in the basis of the determinants formed from the three magnetic orbitals on each site (a, b and c) located on each copper center:

To express this matrix in the coupled basis, *i.e.* in the basis formed from the  $m_s$  components of the quartet and two doublet states, one has to build the transformation matrix. This matrix can be obtained using the Clebsch-Gordan coefficients or by diagonalizing the HDvV Hamiltonian representation matrix and using the eigenvectors as the transition matrix.

$U$	$ \frac{3}{2}, \frac{3}{2}\rangle$	$ \frac{3}{2}, \frac{1}{2}\rangle$	$ \frac{3}{2}, -\frac{1}{2}\rangle$	$ \frac{3}{2}, \frac{-3}{2}\rangle$	$ \frac{1}{2}, \frac{1}{2}\rangle_1$	$ \frac{1}{2}, -\frac{1}{2}\rangle_1$	$ \frac{1}{2}, \frac{1}{2}\rangle_2$	$ \frac{1}{2}, -\frac{1}{2}\rangle_2$
$\langle abc $	1	0	0	0	0	0	0	0
$\langle ab\bar{c} $	0	$\frac{1}{\sqrt{3}}$	0	0	0	0	$-\frac{2}{\sqrt{6}}$	0
$\langle a\bar{b}c $	0	$\frac{1}{\sqrt{3}}$	0	0	$-\frac{1}{\sqrt{2}}$	0	$\frac{1}{\sqrt{6}}$	0
$\langle \bar{a}bc $	0	$\frac{1}{\sqrt{3}}$	0	0	$\frac{1}{\sqrt{2}}$	0	$\frac{1}{\sqrt{6}}$	0
$\langle a\bar{b}\bar{c} $	0	0	$\frac{1}{\sqrt{3}}$	0	0	0	0	$-\frac{2}{\sqrt{6}}$
$\langle \bar{a}b\bar{c} $	0	0	$\frac{1}{\sqrt{3}}$	0	0	$-\frac{1}{\sqrt{2}}$	0	$\frac{1}{\sqrt{6}}$
$\langle \bar{a}\bar{b}c $	0	0	$\frac{1}{\sqrt{3}}$	0	0	$\frac{1}{\sqrt{2}}$	0	$\frac{1}{\sqrt{6}}$
$\langle \bar{a}\bar{b}\bar{c} $	0	0	0	1	0	0	0	0

	$ Q^{3/2}\rangle$	$ Q^{1/2}\rangle$	$ Q^{-1/2}\rangle$	$ Q^{-3/2}\rangle$	$ D_1^{1/2}\rangle$	$ D_1^{-1/2}\rangle$	$ D_2^{1/2}\rangle$	$ D_2^{-1/2}\rangle$
$ Q^{3/2}\rangle$	$\frac{3j}{4}$	0	0	$-\frac{\sqrt{2}}{8}i(2d^{13}-d^{13}-d^{23})(e_x+ie_y)$	0	$\frac{\sqrt{6}}{8}(d^{13}-d^{23})(e_x+ie_y)$	0	0
$ Q^{1/2}\rangle$	0	$\frac{3j}{4}$	0	$-\frac{i\sqrt{6}}{12}e_x(2d^{12}-d^{13}-d^{23})$	$-\frac{i\sqrt{6}}{24}i(2d^{12}-d^{13}-d^{23})(e_x-ie_y)$	$\frac{\sqrt{2}}{4}(i(d^{13}-d^{23})$	$\frac{\sqrt{2}}{8}(d^{13}-d^{23})(e_x+ie_y)$	$\frac{\sqrt{2}}{8}(d^{13}-d^{23})$
$ Q^{-1/2}\rangle$	0	0	$\frac{3j}{4}$	$\frac{\sqrt{6}}{24}i(2d^{12}-d^{13}-d^{23})(e_x-ie_y)$	$-\frac{i\sqrt{6}}{12}e_x(2d^{12}-d^{13}-d^{23})$	$-\frac{\sqrt{2}}{8}i(d^{13}-d^{23})(e_x-ie_y)$	$-\frac{\sqrt{2}}{8}i(d^{13}-d^{23})$	$-\frac{\sqrt{2}}{8}i(d^{13}-d^{23})$
$ Q^{-3/2}\rangle$	0	0	0	$\frac{3j}{4}$	$0$	$0$	$0$	$0$
$ D_1^{1/2}\rangle$	0	0	0	$\frac{3j}{4}$	$0$	$\frac{\sqrt{3}}{6}i(d^{12}+d^{13}+d^{23})e_z$	$-\frac{1}{2\sqrt{3}}i(d^{12}+d^{13}+d^{23})(e_x+ie_y)$	$-\frac{1}{2\sqrt{3}}i(d^{12}+d^{13}+d^{23})$
$ D_1^{-1/2}\rangle$	0	0	0	0	$0$	$0$	$0$	$0$
$ D_2^{1/2}\rangle$	0	0	0	0	$-\frac{3j}{4}$	$-\frac{1}{4}$	$-\frac{3j}{4}$	$-\frac{3j}{4}$
$ D_2^{-1/2}\rangle$	0	0	0	0	$0$	$0$	$0$	$0$

Figure 5.9: Representation matrix of the Multi-Spin Hamiltonian in the basis of the four components of the quartet and the doubly-degenerate doublet states

The symmetric tensor terms (6 each, 18 total) are left out of the matrix for clarity but are taken into account during the extraction. The extracted Dzyaloshinskii-Moriya pseudo vectors are:

$$\mathbf{d}_{12} = \begin{pmatrix} -4.1 \\ 2.36 \\ 1.70 \end{pmatrix} \quad \mathbf{d}_{13} = \begin{pmatrix} 0 \\ 4.73 \\ 1.70 \end{pmatrix} \quad \mathbf{d}_{23} = \begin{pmatrix} 4.1 \\ 2.36 \\ 1.70 \end{pmatrix}$$

The axis system was not changed between the dinuclear and trinuclear fragment. Hence, the two  $Cu^{2+}$  ions numbered 1 and 2 in the trinuclear fragment are the one that are included in the dinuclear calculation. Note that the extracted DMI-vector is strictly the same  $\mathbf{d}_{12}^{dinuclear} = \mathbf{d}_{13}^{trinuclear}$  which validate the expansion to a trinuclear fragment. The three DMI vectors share the same out of plane  $d_z^{ij} = 1.70K$  and in plane component  $|d_{xy}^{ij}| = 4.73K$ . Their orientations is depicted in Figure 5.10. It is important to mention that the out-of-plane component  $d_\perp$  oscillates between below and above the (XY) plane of copper ions from one triangle to the next, following the alternating positions above and below of the oxygens

Fragment	$ d_{ij}^{\parallel} $	$ d_{ij}^{\parallel} $	$ d $	D	E
Bi-nuclear	4.73	1.70	5.03	-0.46	0.13
Tri-nuclear	4.73	1.78	5.05	-0.51	0.16

Table 5.6: Values in Kelvin of the  $|d|$  DM magnitude and its components, axial (D) and rhomic (E) anisotropic exchange parameters, obtained for both fragments.

Table 5.6 provides the results obtained from the extractions performed on the bi-nuclear and tri-nuclear fragments. It shows good agreement between the two fragments for all of the parameters considered in the model.

### 5.3 Conclusion

The purpose of this work was the application of *ab initio* calculation to extraction magnetic interactions in Herbertsmithite which has not been done before. The first part of the study focused on the isotropic couplings using embedded cluster method, the exploration of fragments with different sizes has been done using DFT calculations, it allowed the determination of the possible isotropic couplings. Extractions performed on the multiple fragment showed good transferability of the couplings from one cluster to the other. This justify the validity of the

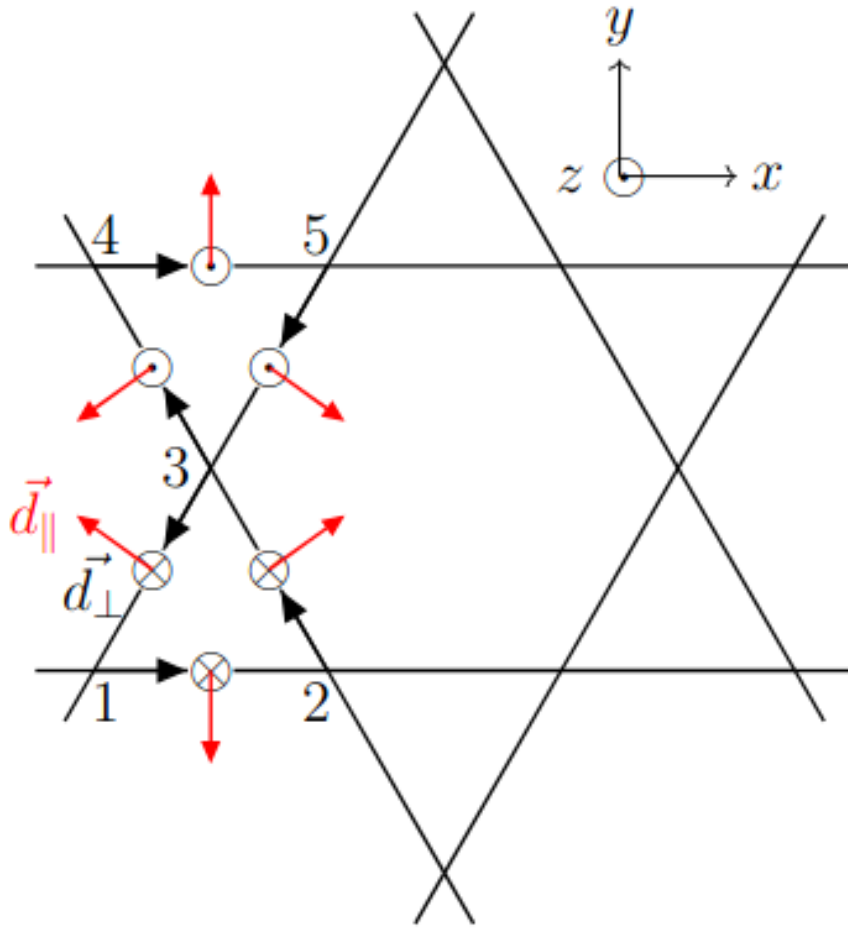


Figure 5.10: Schematic representation of the DMI vector components in two adjacent  $Cu^{2+}$  triangles of the lattice. The black arrows between the magnetic centers indicates the order of the first and second spins in the vector products of the DM interactions. The out-of-plane components alternate from one triangle to its neighbors and point in the opposite direction to the position of the oxygens. The angle between the in-plane components of the vectors within the triangle is  $120^\circ$ .

application of the embedded cluster method for this material. The study of the structure without defects indicates that the only relevant in-plane coupling is between first neighbour. A reported value of  $J_1 \approx 180K$  matches very well with experimental data, other couplings were found to be two order of magnitude smaller. The subject of defects was addressed as well with the study of structural deformation around the most recurring defect. The substitution of the intersite  $Zn^{2+}$  ion by a additional  $Cu^{2+}$  ion tends to modify the environment near this site due a strong Jahn-Teller effect. Two types of structure were identified, which differ by the displacement of the hidroxide groups around the

intersite. As the two structure are close in energy,  $\approx 100K$ , the extraction of isotropic couplings was performed for both geometries. It was found that the deformations have a significant impact on the in-plane coupling, replacing the unique  $J_1$  by two different  $J$  values. The most remarkable result of this study is the introduction of new ferromagnetic couplings between in-plane copper ions and the intersite defect. These coupling are non negligible,  $\approx 0.4|J_1|$ , which could have a strong impact on the measurement at low temperature. The second part of this study focused on the extraction of anisotropic interactions on a dinuclear and trinuclear fragment. First, the extraction of the first neighbour coupling using wave-function based method was performed. It was found that an active space composed only of the d-orbitals does not allow a good estimation of  $J_1$ . To solve this problem, some orbitals of the bridging ligand were included in the active space enable following a projection procedure. This allowed the extraction of a  $J_1$  value that compares well with DFT calculations. Then, the Dzyaloshinskii-Moriya pseudovector and the symmetric tensor of anisotropic exchange were extracted on both fragments. A significant value of DMI was obtained with both an out-of plane and in-plane components, the latter usually overlooked in theoretical models. Results between fragment compares perfectly which validate the use of the Multi-Spin Hamiltonian to describe the anisotropy of this system.